Supplementary Information

Bottlebrush Polymers with Discrete Sidechains Display Stereochemistry- and Conformation-Dependent Biological Properties

Hung V.-T. Nguyen,[†,φ] Yivan Jiang,[†,φ] Somesh Mohapatra,[§] Wencong Wang,[†] Jonathan C. Barnes,[†] Nathan J. Oldenhuis,[†] Kathleen K. Chen,[†] Simon Axelrod,[§,‡] Zhihao Huang,[†] Qixian Chen,[†] Matthew R. Golder,[†] Katherine Young,[†] Dylan Suvlu,[†] Yizhi Shen,[†] Adam P. Willard,[†] Michael J. A. Hore,[⊥] Rafael Gómez-Bombarelli,[§,*] Jeremiah A. Johnson[†,*]

[†]Department of Chemistry, and [§]Department of Materials Science and Engineering, Massachusetts Institute of Technology, 77 Massachusetts Avenue, Cambridge, Massachusetts 02139, United States
[‡]Department of Chemistry and Chemical Biology, Harvard University, 12 Oxford Street, Cambridge, Massachusetts 02138, United States
[⊥]Department of Macromolecular Science and Engineering, Case Western Reserve University, 10900 Euclid Avenue, Cleveland, Ohio 44106, United States

[φ]These authors contributed equally to this work.

*Email: jaj2109@mit.edu; rafagb@mit.edu

Table of Contents

Section A. Supplementary Figures

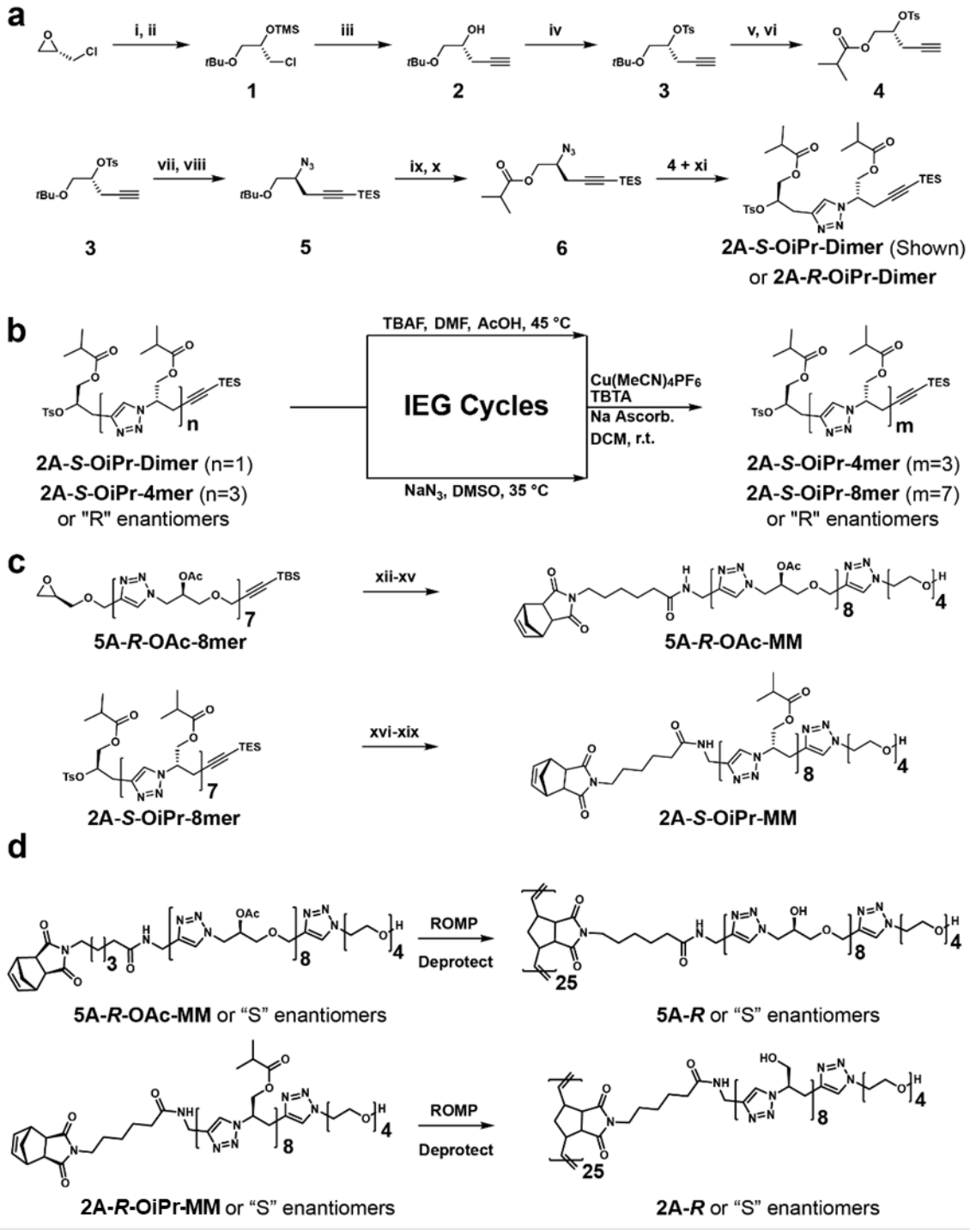

Figure 1. (a) Synthesis of "2 atom" dimer. (i) *t*-BuOH, BF_3OEt_2; (ii) TMSCl, imidazole, DMF; (iii) lithium TMS acetylide, DMSO, THF, hexanes, r.t.; (iv) TsCl, 4-DMAP, TEA, DCM; (v) TFA, DCM; (vi) isobutyric anhydride, 4-DMAP, TEA, DCM; (vii) NaN_3, DMSO, 35 °C; (viii)

NaHMDS, TESCl, THF; (ix) TFA, DCM; (x) isobutyric anhydride, 4-DMAP, TEA, DCM; (xi) $Cu(MeCN)_4PF_6$, TBTA, Na ascorbate, DCM. **(b)** IEG synthesis of 2-atom octamer from dimer. **(c)** Chain end modification scheme for the synthesis of MMs **5A-*R*-OAc-MM** and **2A-*S*-OiPr-MM**. (xii) NaN_3, AcOH, DMF, 60 °C then Ac_2O, 4-DMAP; (xiii) **Nb-yne**, CuBr, PMDTA, Na ascorbate, DMF; (xiv) TBAF, THF; (xv) azido-tetraethyleneglycol, CuBr, PMDTA, Na ascorbate, DMF; (xvi) TBAF, AcOH, DMF; (xvii) azido-tetraethyleneglycol, $Cu(MeCN)_4PF_6$, TBTA, Na ascorbate, DCM; (xviii) NaN_3, DMSO; (xix) **Nb-yne**, CuBr, PMDTA, Na ascorbate, DMF. **(d)** chiral bottlebrush polymer (CBP) synthesis. (ROMP): Grubbs 3rd generation catalyst, DCM; (Deprotect): K_2CO_3 in MeOH/DCM and K_2CO_3 in water/acetone subsequently.

Norbornene-based end group

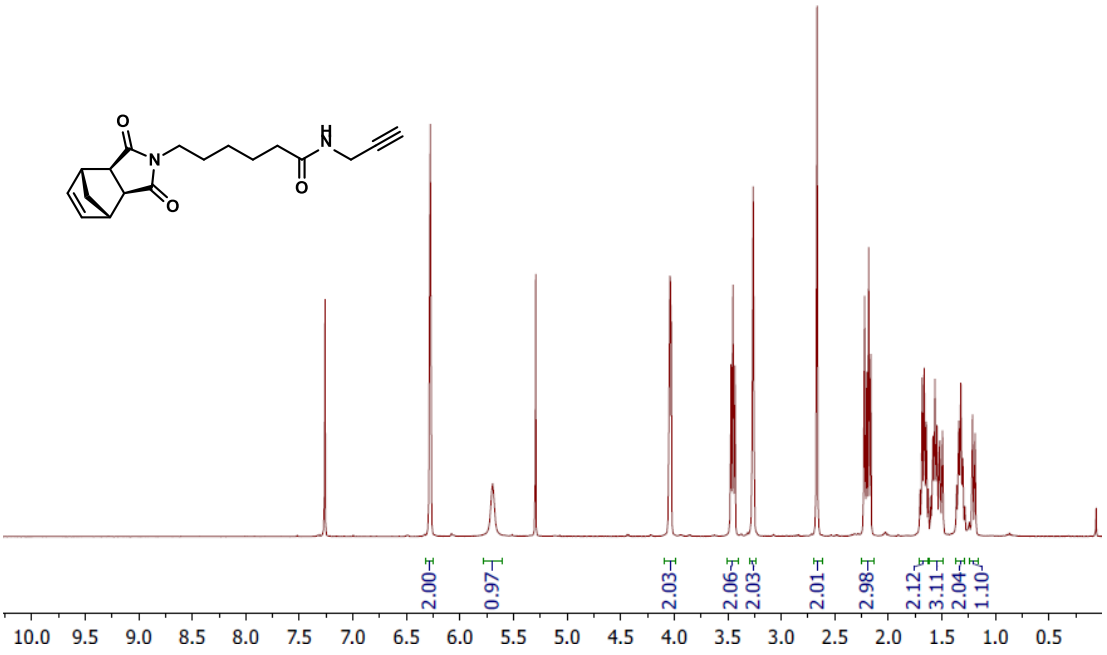

Figure 2. ^{1}H NMR spectrum for **Nb-yne** in $CDCl_3$.

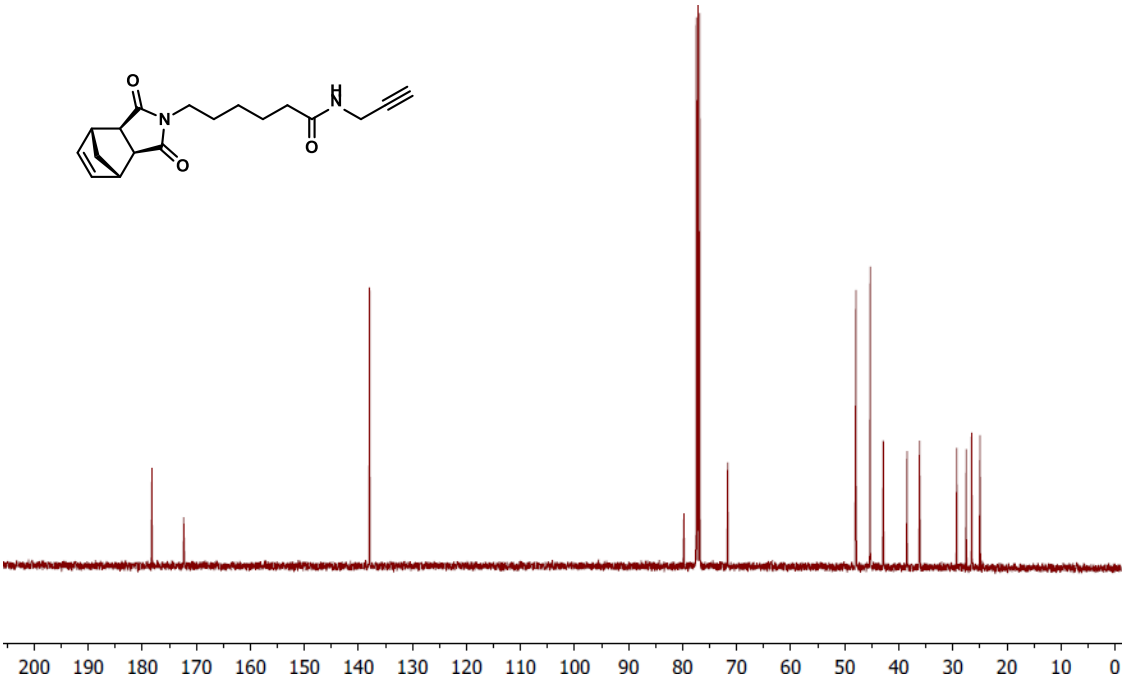

Figure 3. ^{13}C NMR spectrum for **Nb-yne** in $CDCl_3$.

"5-Atom" Iterative Exponential Growth (5AIEG) Macromonomers (MMs)

5A-R-OAc-MM

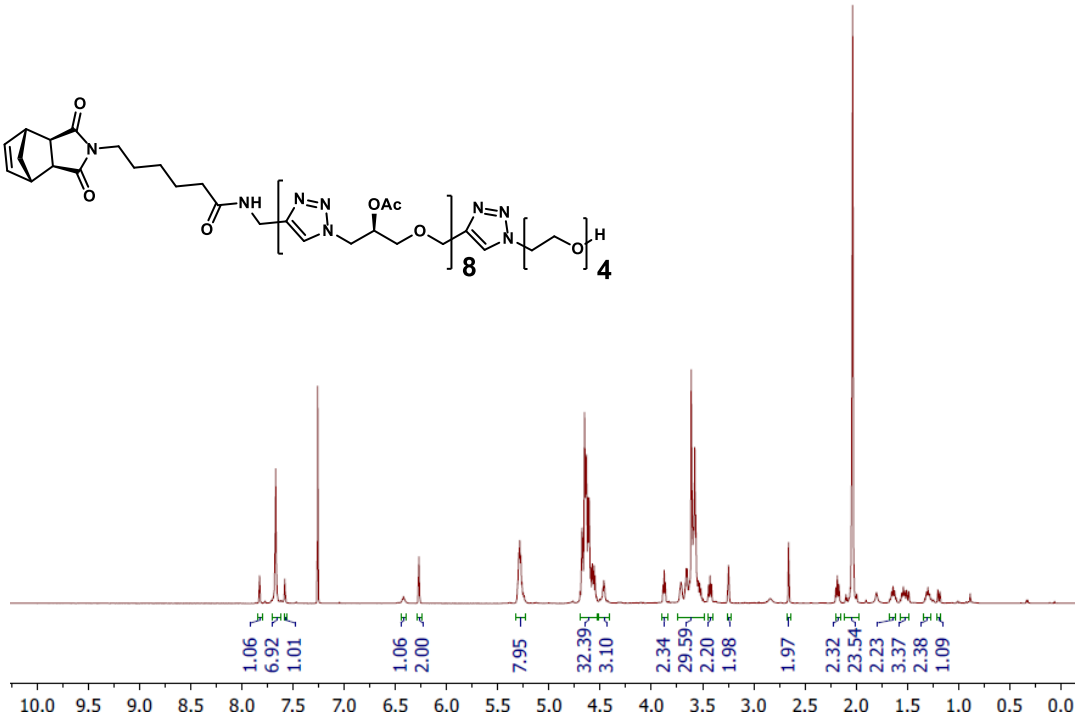

Figure 4. ^{1}H NMR spectrum for **5A-*R*-OAc-MM** in $CDCl_3$.

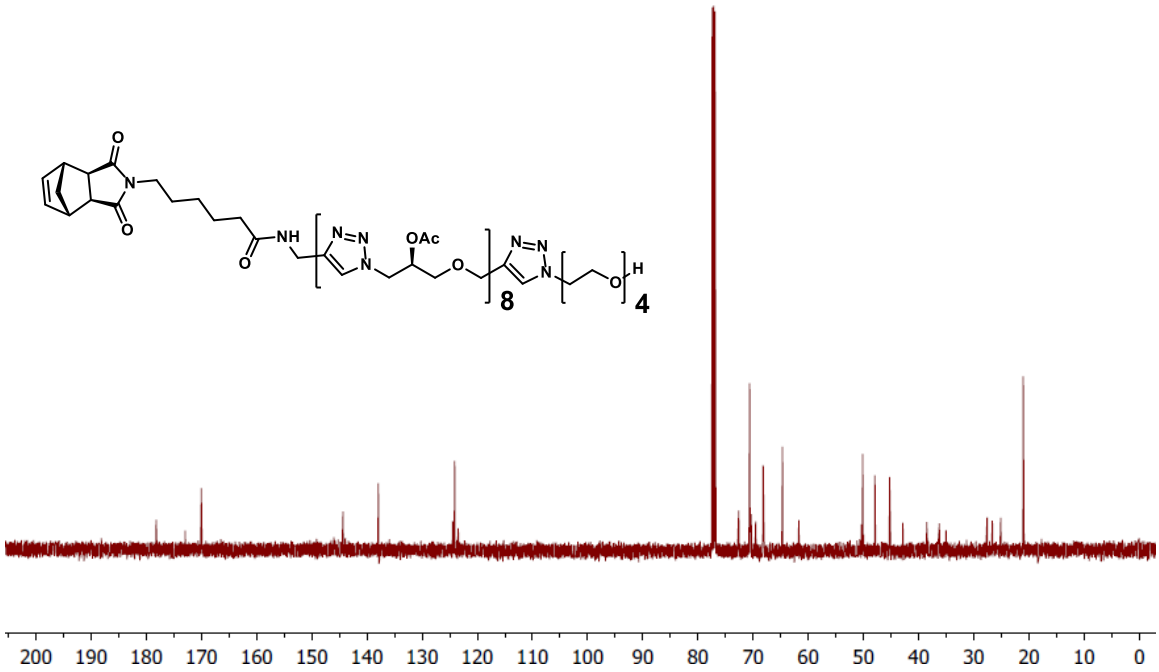

Figure 5. ^{13}C NMR spectrum for **5A-*R*-OAc-MM** in $CDCl_3$.

5A-S-OAc-MM

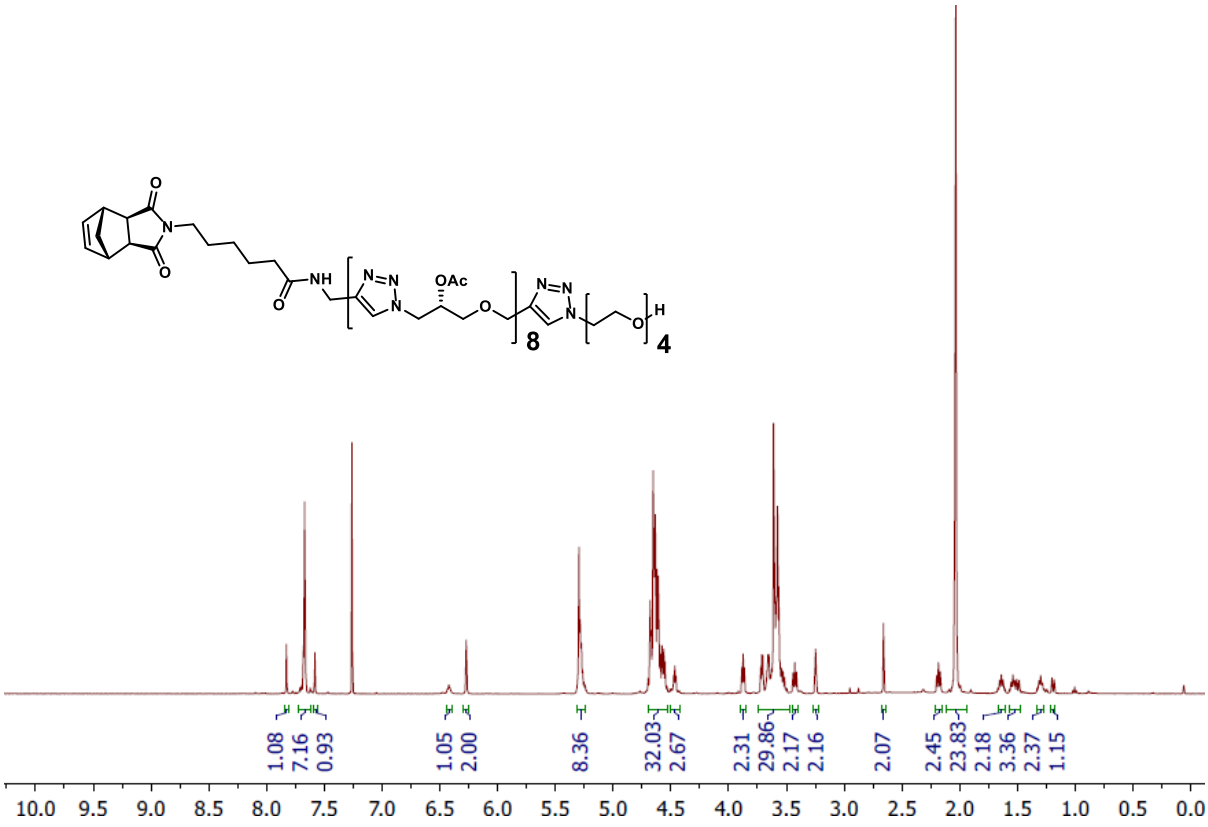

Figure 6. ^{1}H NMR spectrum for **5A-*S*-OAc-MM** in $CDCl_3$.

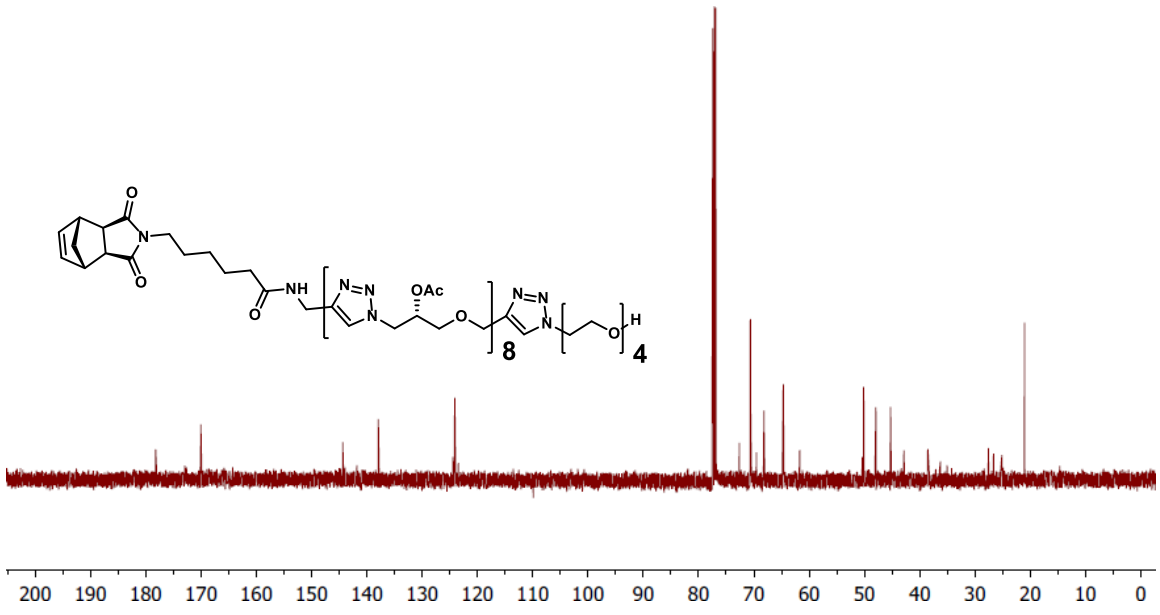

Figure 7. ^{13}C NMR spectrum for **5A-*S*-OAc-MM** in $CDCl_3$.

Matrix-Assisted Laser Desorption/Ionization Time-of-Flight Mass Spectrometry (MALDI-TOF-MS)

5AIEG MMs

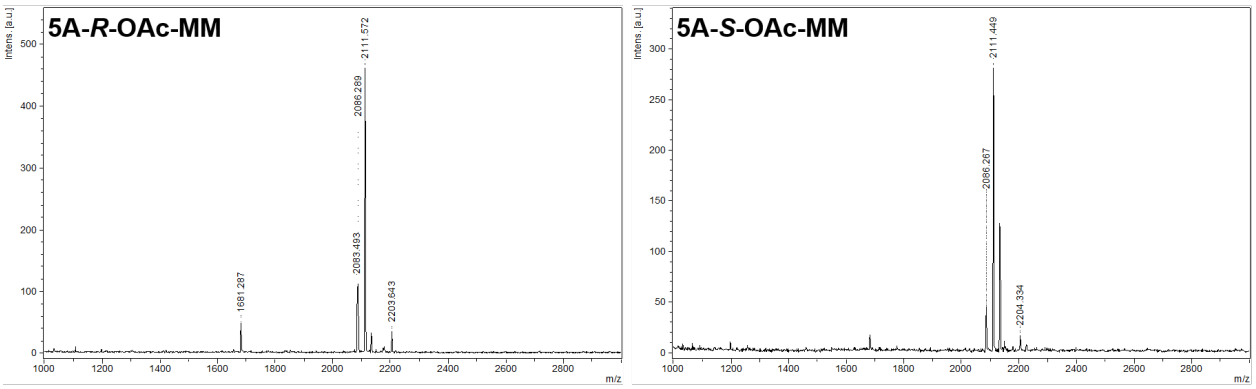

Figure 8. MALDI-TOF-MS of **5A-*R*-OAc-MM** and **5A-*S*-OAc-MM**. (Cald. 2110.93 $[M+H]^+$)

"2-Atom" Iterative Exponential Growth (2AIEG) MMs

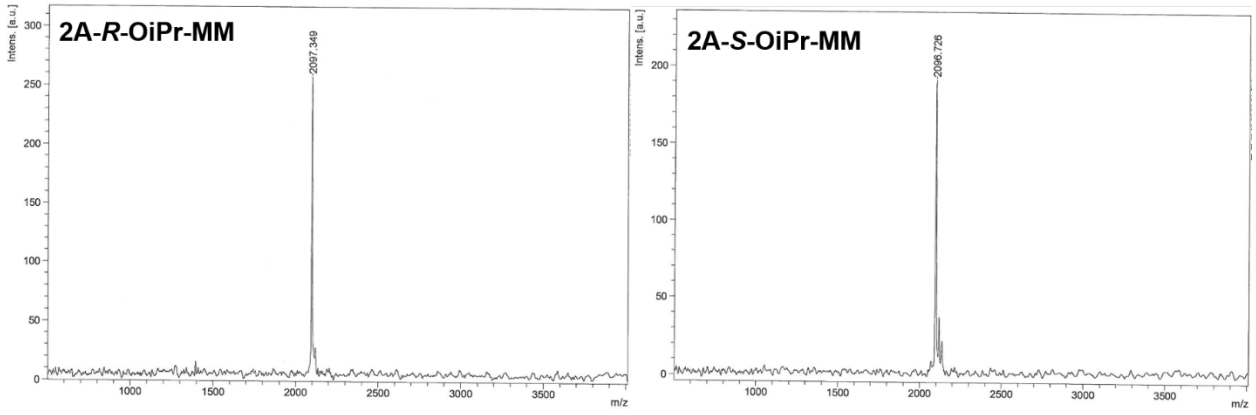

Figure 9. MALDI-TOF-MS of **2A-*R*-OiPr-MM** and **2A-*S*-OiPr-MM**. (Cald 2096.86 $[M+H]^+$)

2AIEG Small Molecule Precursors and MMs

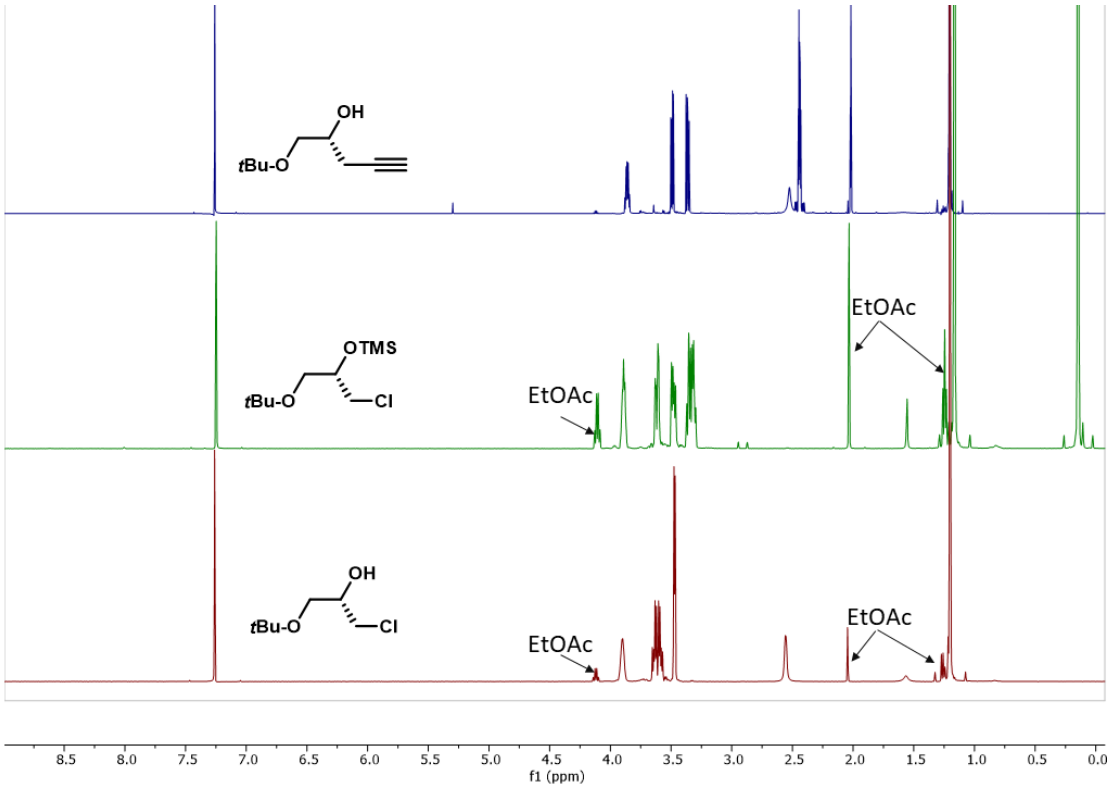

Figure 10. ^{1}H NMR spectra for **d1**, **1**, and **2** in $CDCl_3$.

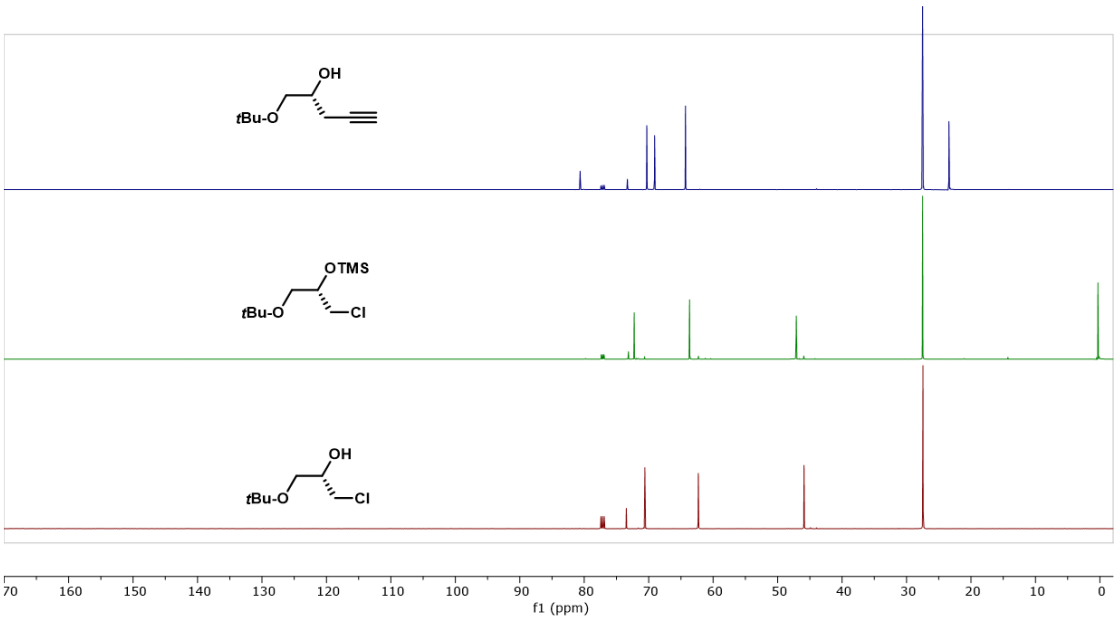

Figure 11. ^{13}C NMR spectra for **d1**, **1**, and **2** in $CDCl_3$.

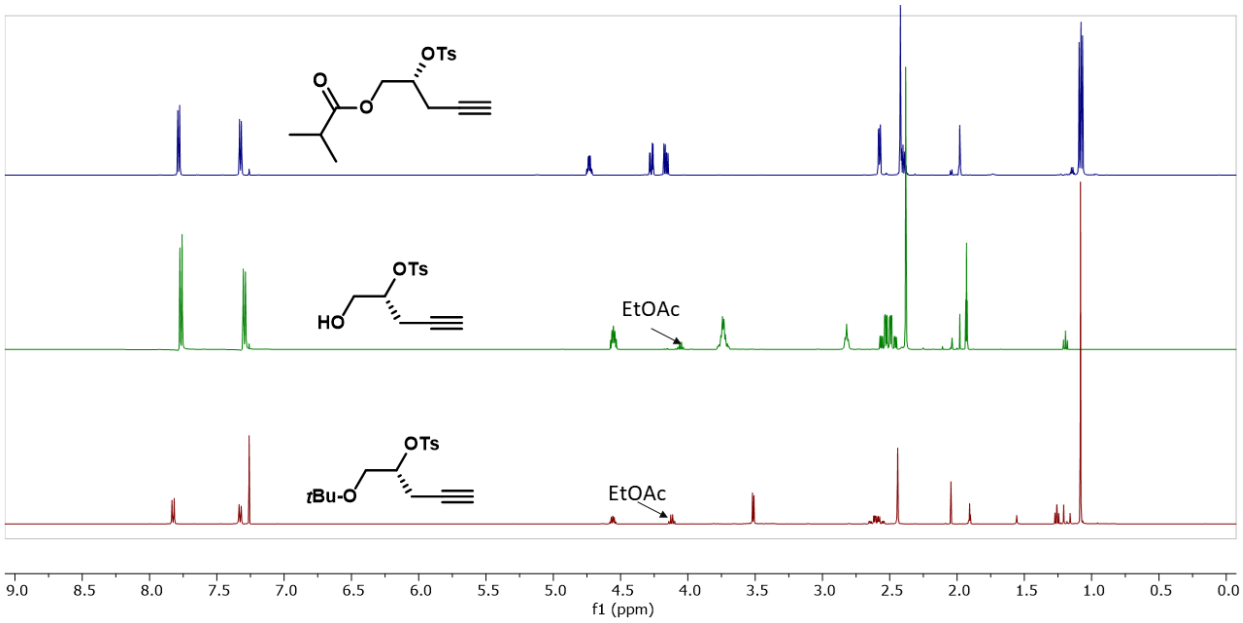

Figure 12. ^{1}H NMR spectra for **3**, **d4**, and **4** in $CDCl_3$.

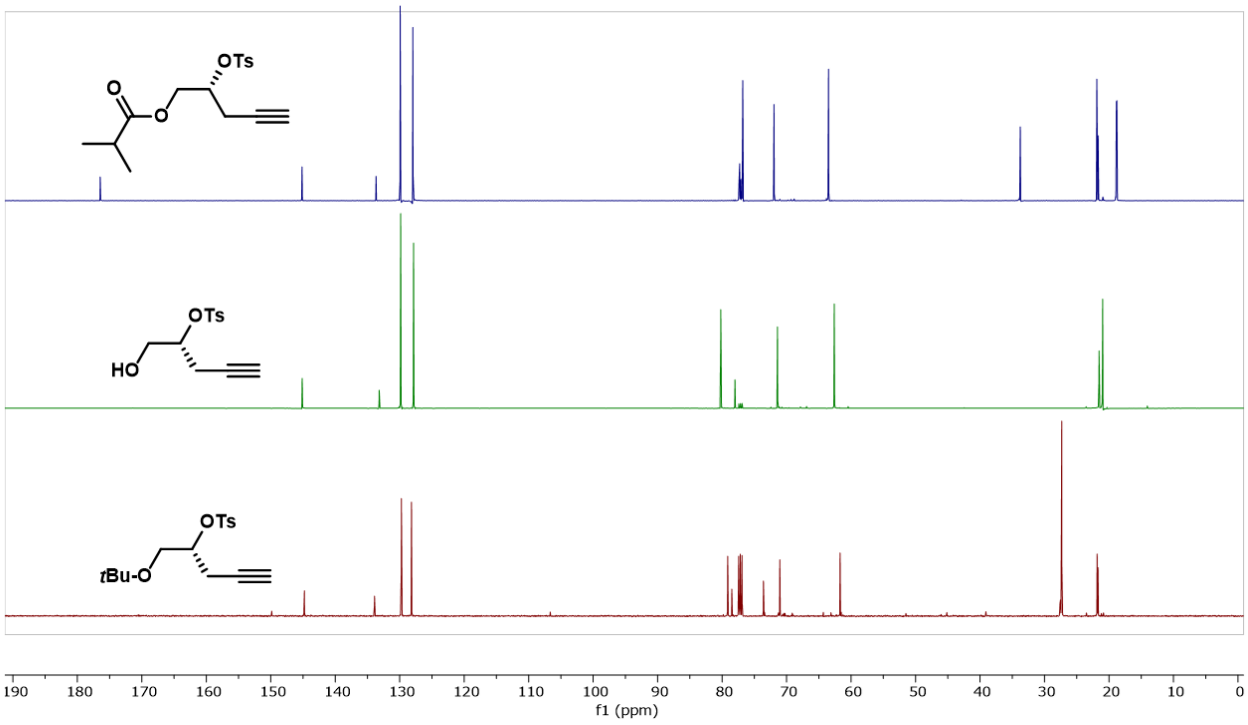

Figure 13. ^{13}C NMR spectra for **3**, **d4**, and **4** in $CDCl_3$.

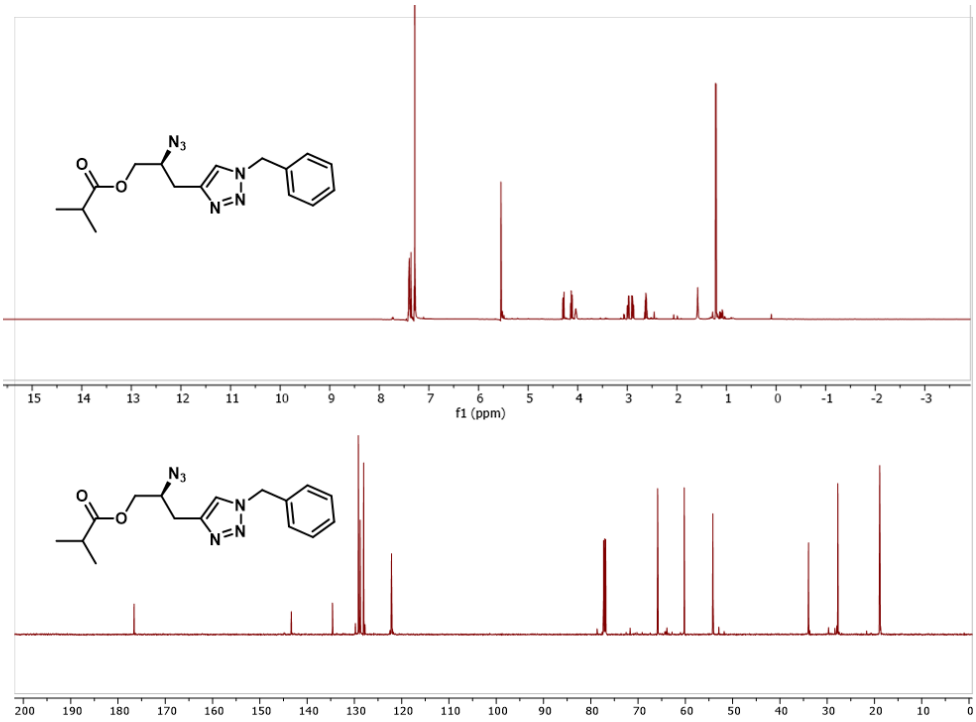

Figure 14. ^{1}H and ^{13}C NMR spectra for **7** in $CDCl_3$.

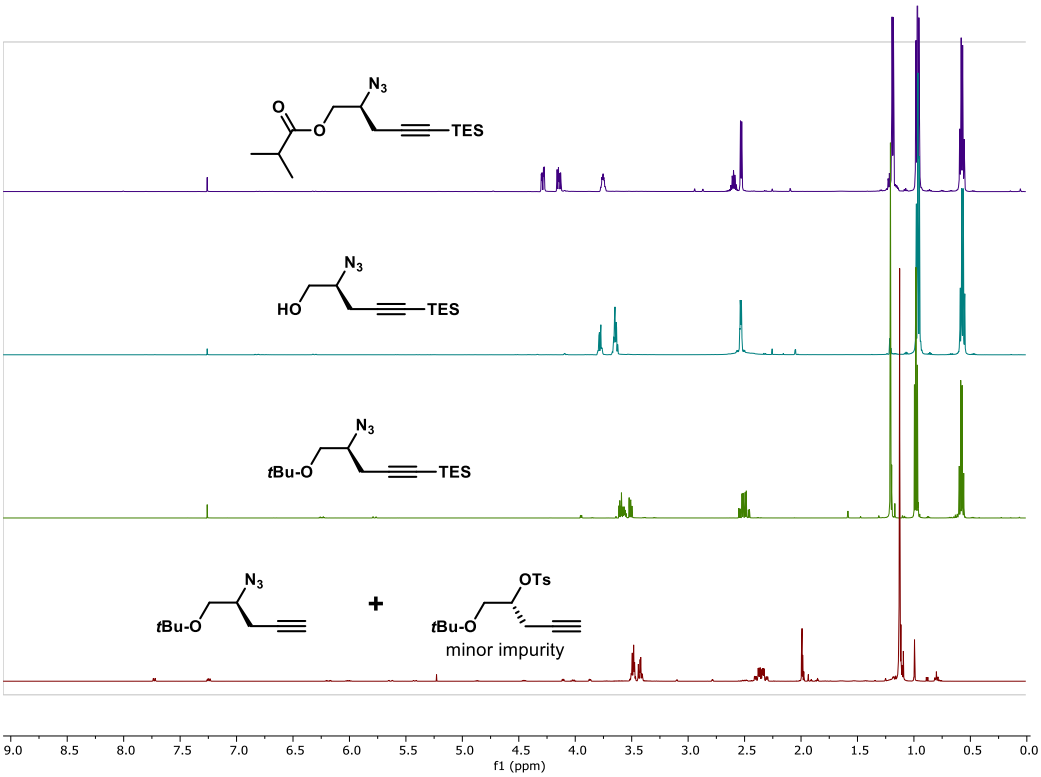

Figure 15. ^{1}H NMR spectra of **d2**, **5**, **d4**, and **6** in $CDCl_3$.

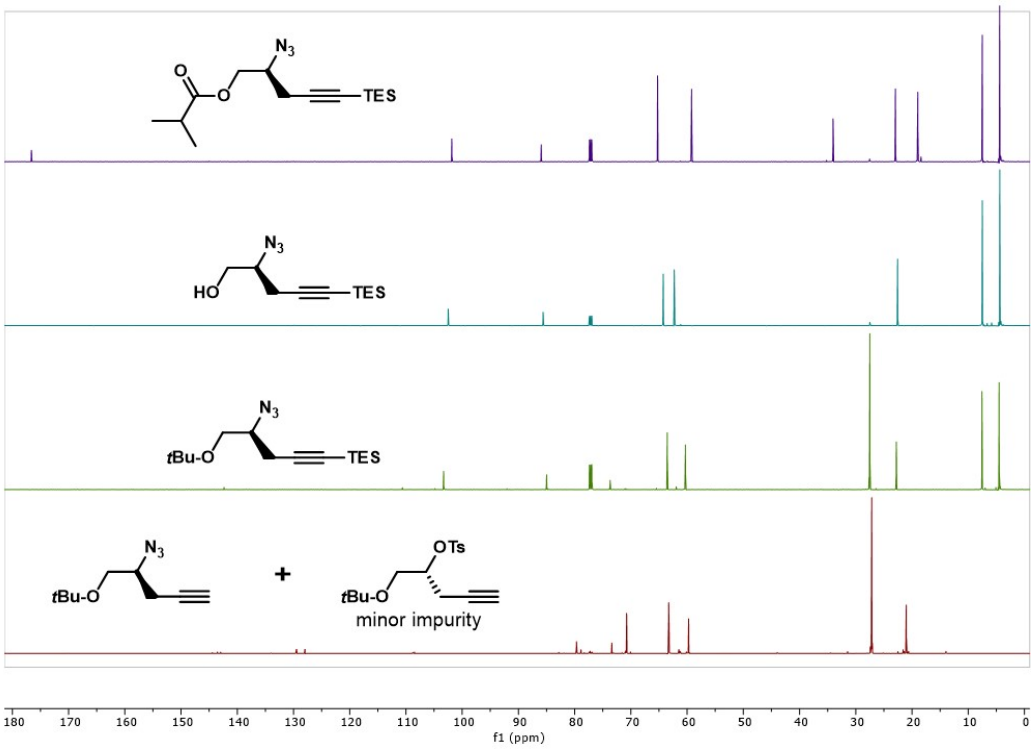

Figure 16. ^{13}C NMR spectra for **d2**, **5**, **d4**, and **6** in $CDCl_3$.

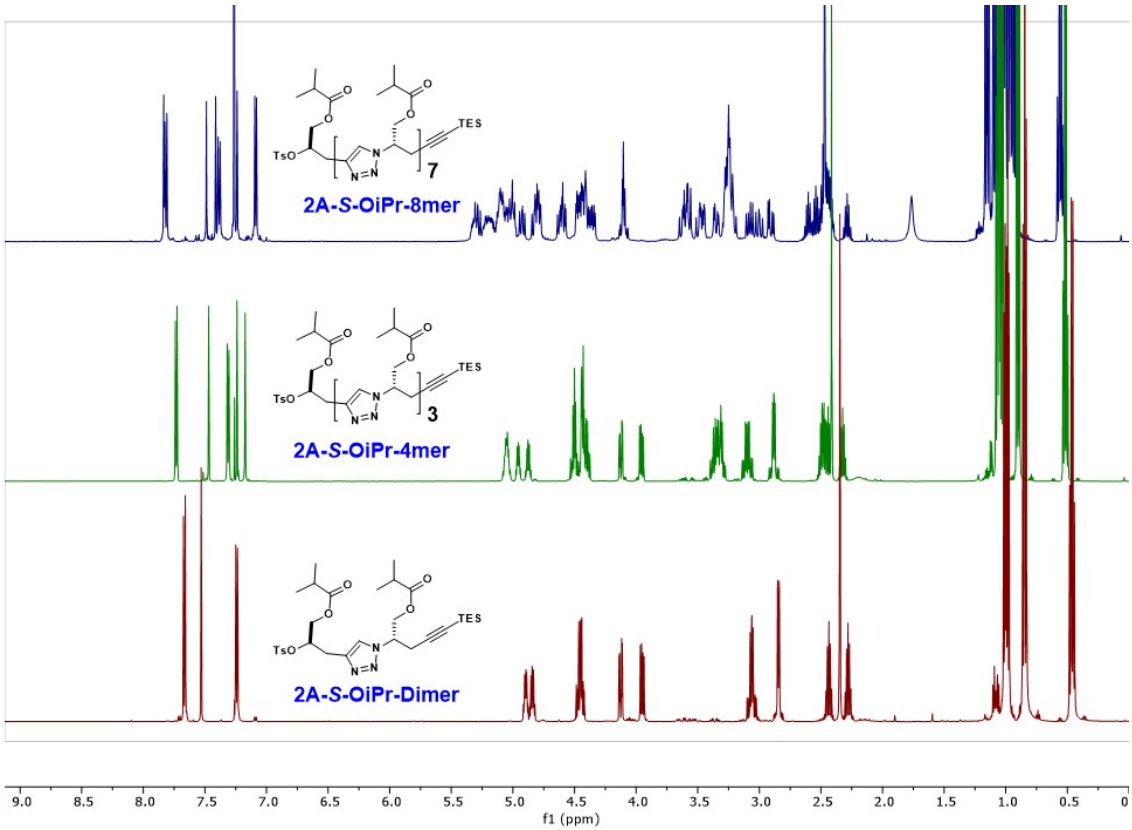

Figure 17. ^{1}H NMR spectra of **2AIEG** oligomers in $CDCl_3$.

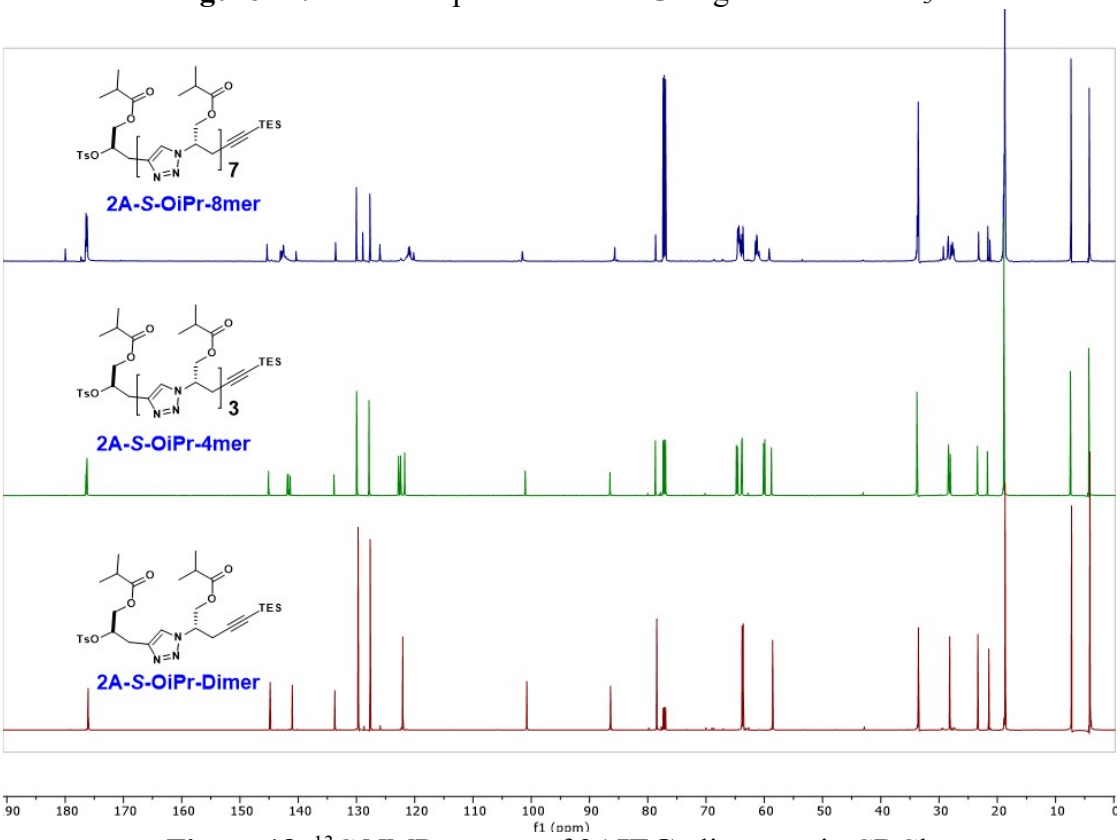

Figure 18. ^{13}C NMR spectra of **2AIEG** oligomers in $CDCl_3$.

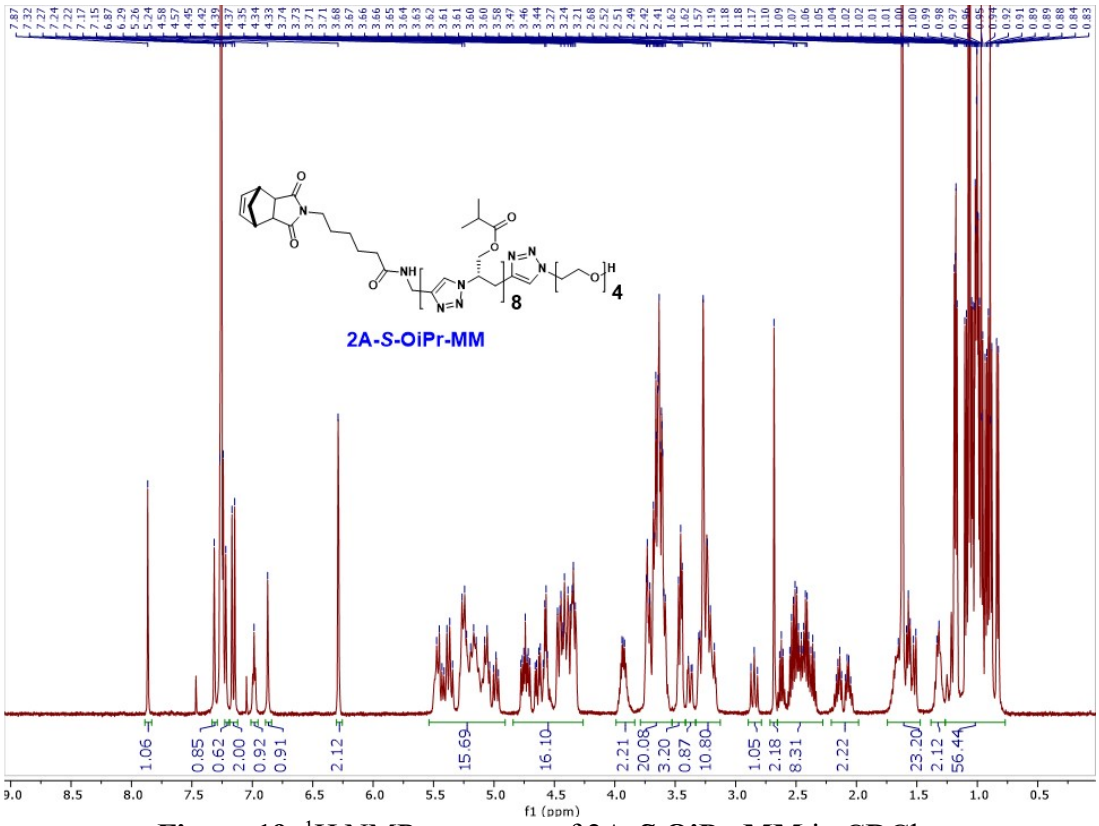

Figure 19. ^{1}H NMR spectrum of **2A-*S*-OiPr-MM** in $CDCl_3$.

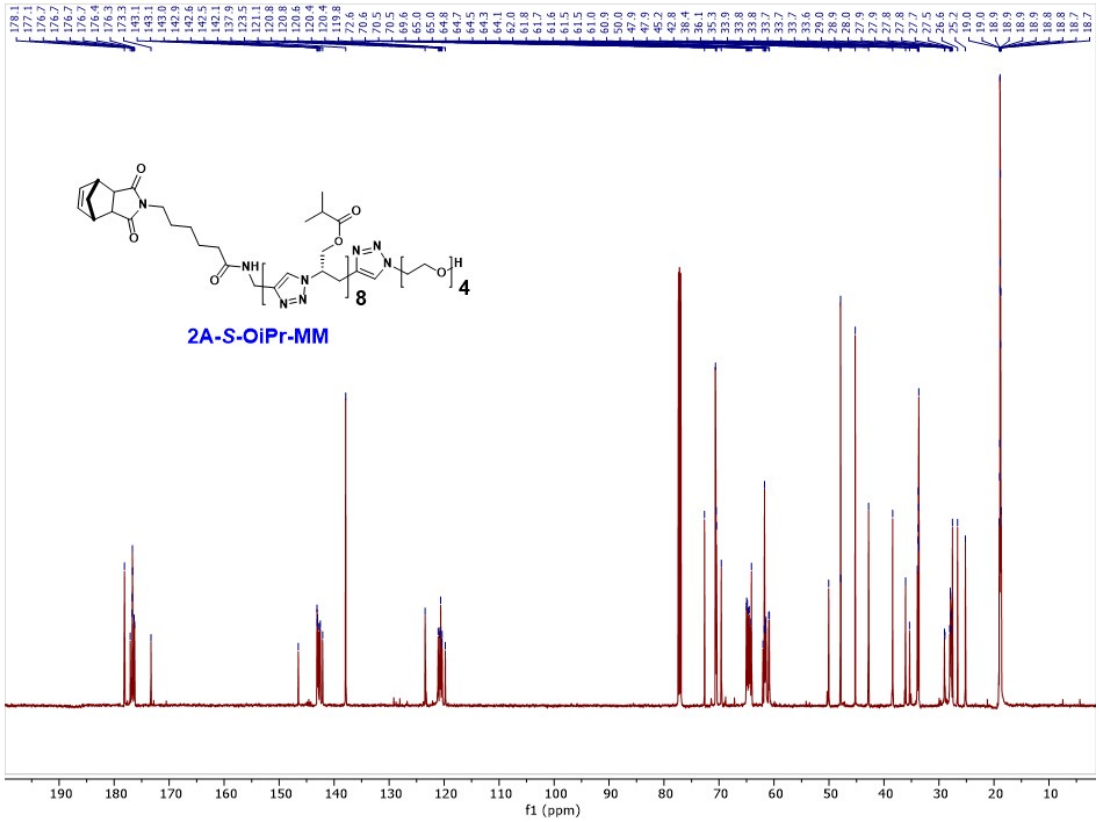

Figure 20. ^{13}C NMR spectrum of **2A-*S*-OiPr-MM** in $CDCl_3$.

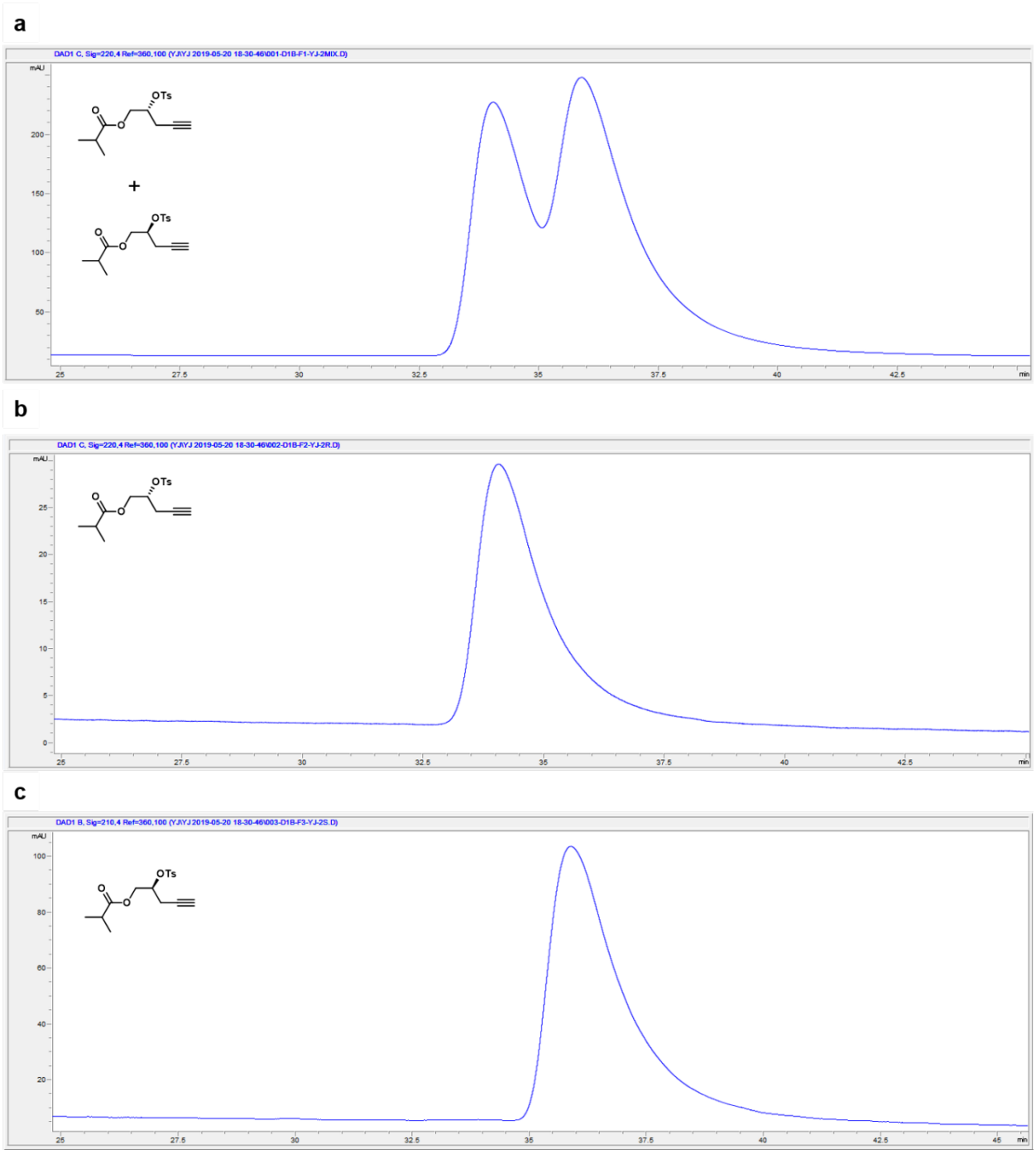

Figure 21. Chiral HPLC traces for **a.** racemic mixture of **4**, **b.** (*R*)-**4**, and **c.** (*S*)-**4**.

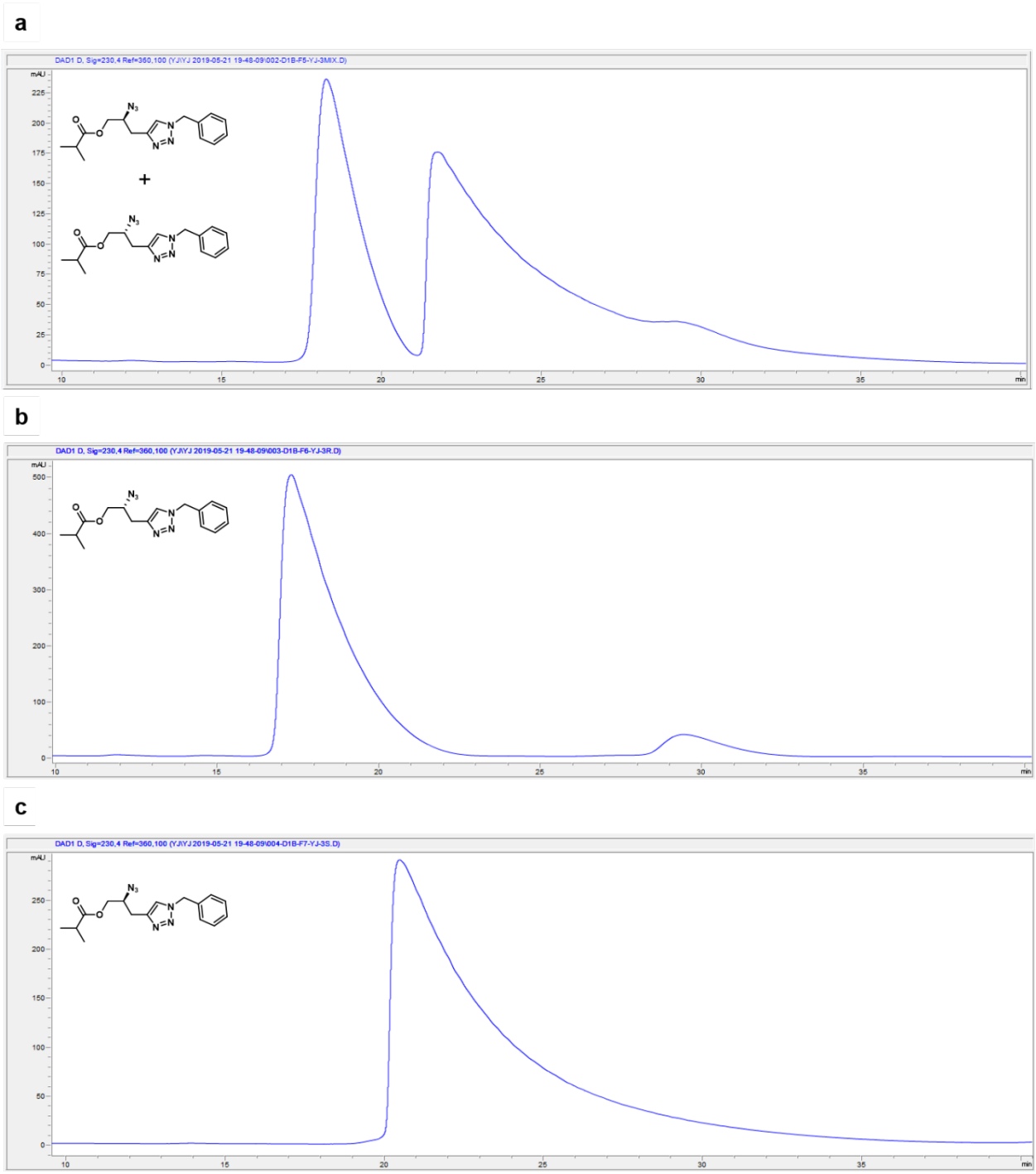

Figure 22. Chiral HPLC traces for **a.** racemic mixture of **7**, **b.** (*R*)-**7**, and **c.** (*S*)-**7**.

Gel Permeation Chromatography (GPC) of Bottlebrush Polymers

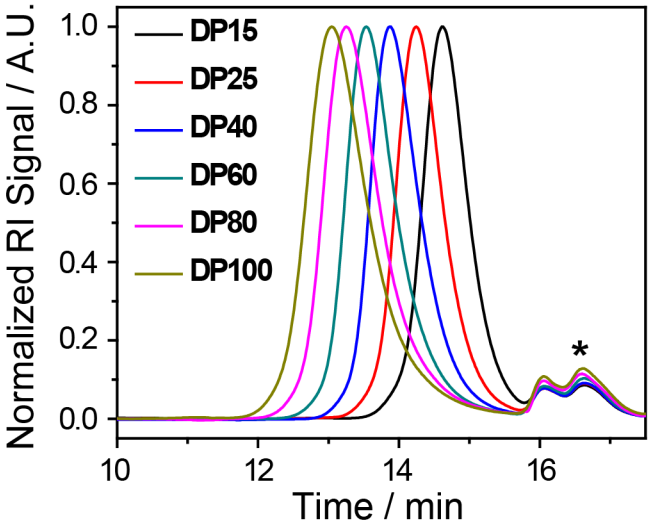

Figure 23. GPC traces of chiral bottlebrush polymers with varying degrees of polymerizations (DPs) for the 2 atom IEG MM **2A-*S*-OiPr-MM**. * denotes residual MM in the crude reaction mixture prior to deprotection and dialysis. In all cases, conversions of >90% was observed.

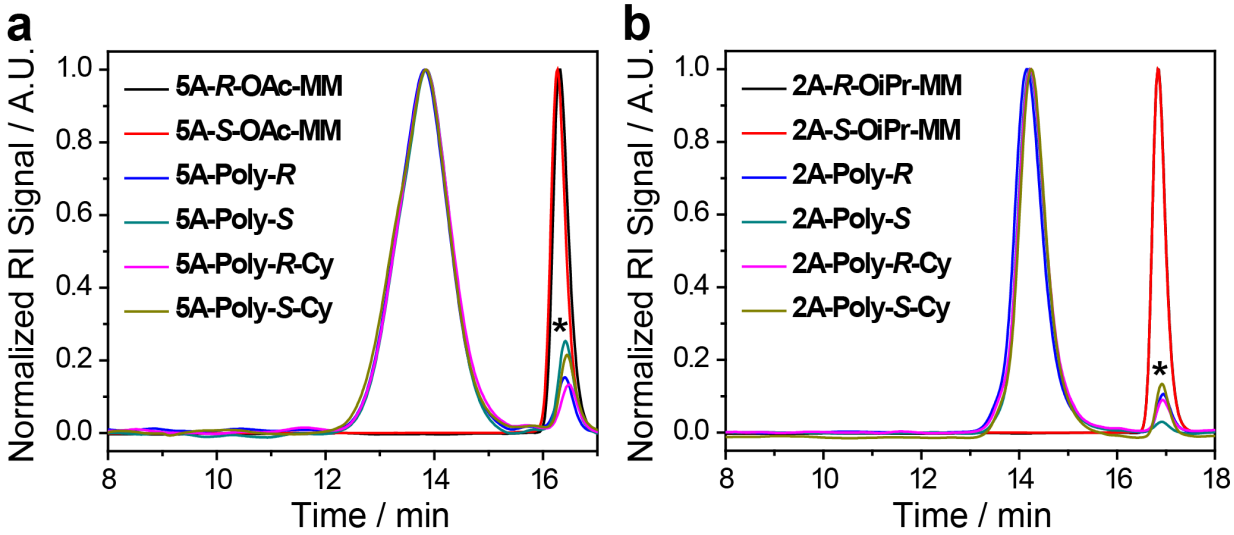

Figure 24. GPC traces for IEG MMs and the corresponding bottlebrush polymers for the **a.** 5AIEG and **b.** 2AIEG systems. * denotes residual MM in the crude reaction mixture prior to deprotection and dialysis. In all cases, conversions of >90% was observed.

Table 1. Characterization Data for MMs and Chiral Bottlebrush Polymers (CBPs)

Polymer	***M_w* (kDa)***	***Đ***	***CBP***	***D_h***
5A-*R*-OAc-MM	2.111	1.201		
5A-*S*-OAc-MM	1.925	1.187		
5A-Poly-*R*	56.19	1.255	**5A-*R***	3.2 ± 0.6
5A-Poly-*S*	60.66	1.268	**5A-*S***	3.3 ± 0.7
2A-*R*-OiPr-MM	2.089	1.216		
2A-*S*-OiPr-MM	2.162	1.146		
2A-Poly-*R*	67.07	1.271	**2A-*R***	2.8 ± 0.4
2A-Poly-*S*	59.78	1.212	**2A-*S***	2.5 ± 0.3

*Absolute weight-average molar masses (M_w) were acquired using static light scattering with d*n*/d*c* values of 0.1210 for 5AIEG and 0.0775 for 2AIEG species.

5A-Poly-R

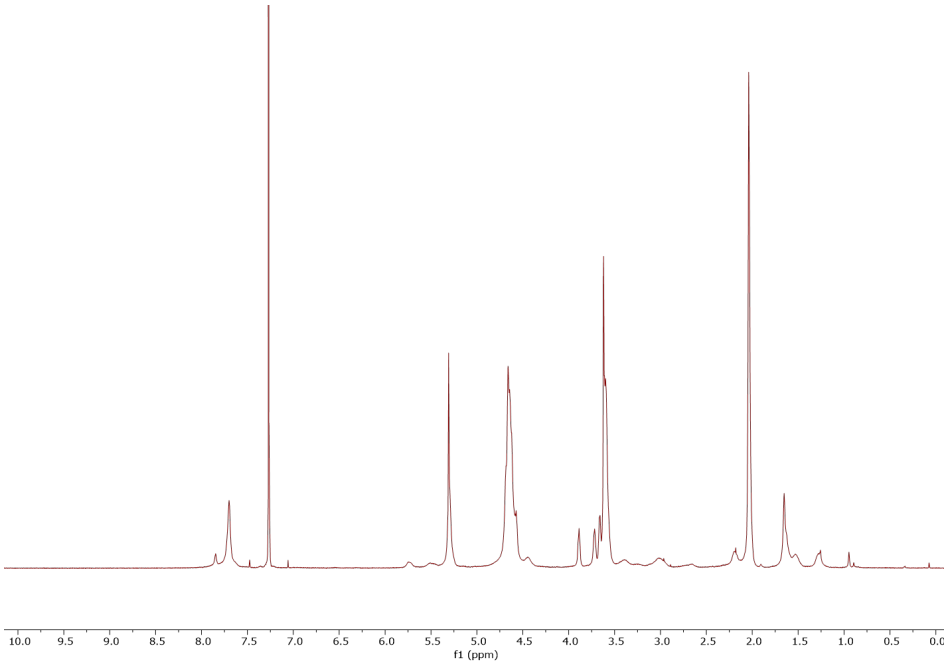

Figure 25. ^{1}H NMR spectrum for **5A-Poly-*R*** in $CDCl_3$.

5A-Poly-S

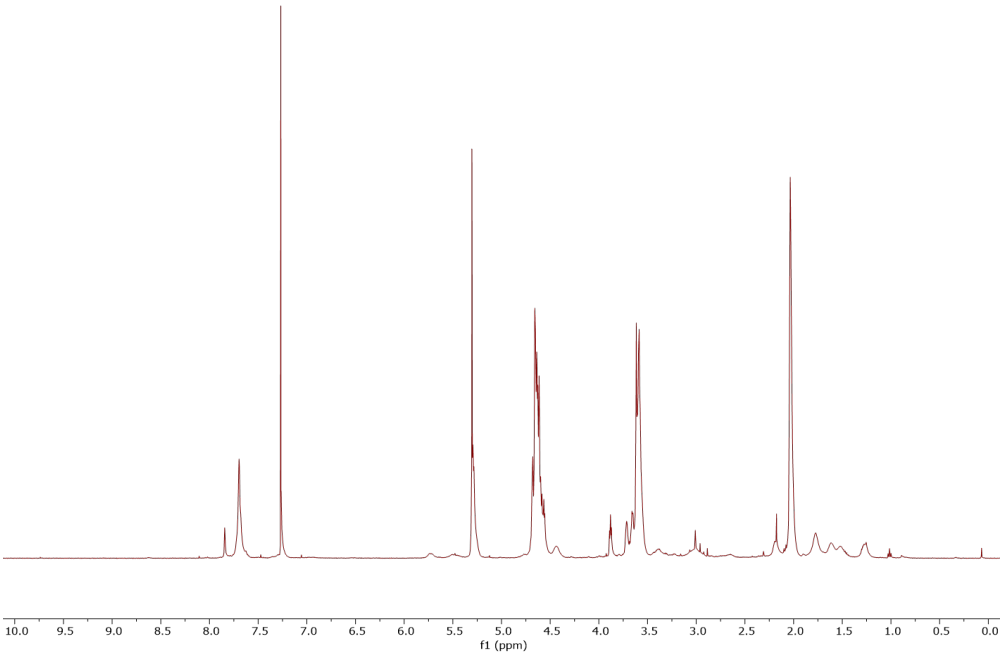

Figure 26. ^{1}H NMR spectrum for **5A-Poly-*S*** in $CDCl_3$.

5A-Poly-R-Cy

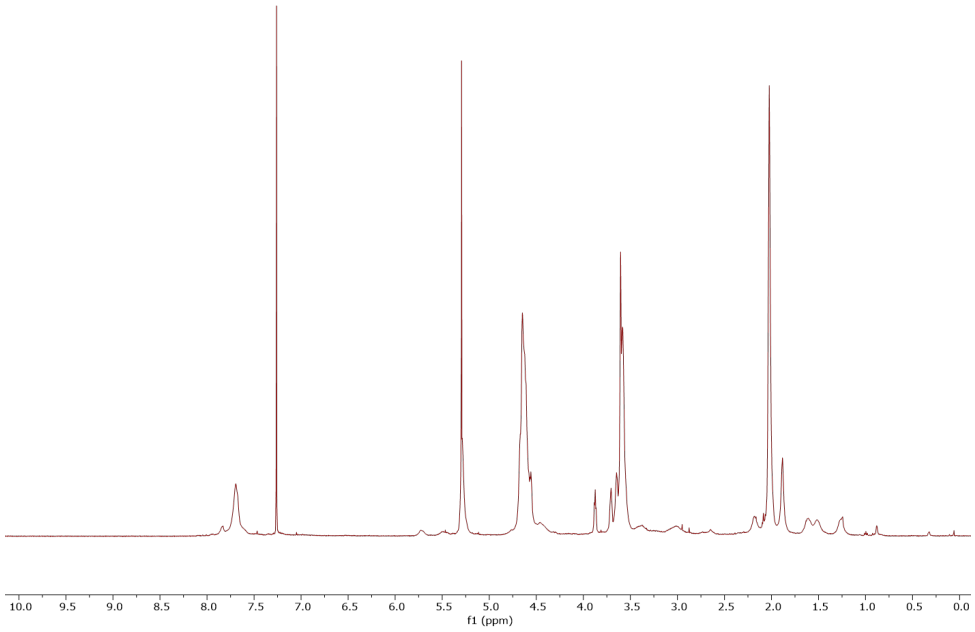

Figure 27. ^{1}H NMR spectrum for **5A-Poly-*R*-Cy** in $CDCl_3$.

5A-Poly-S-Cy

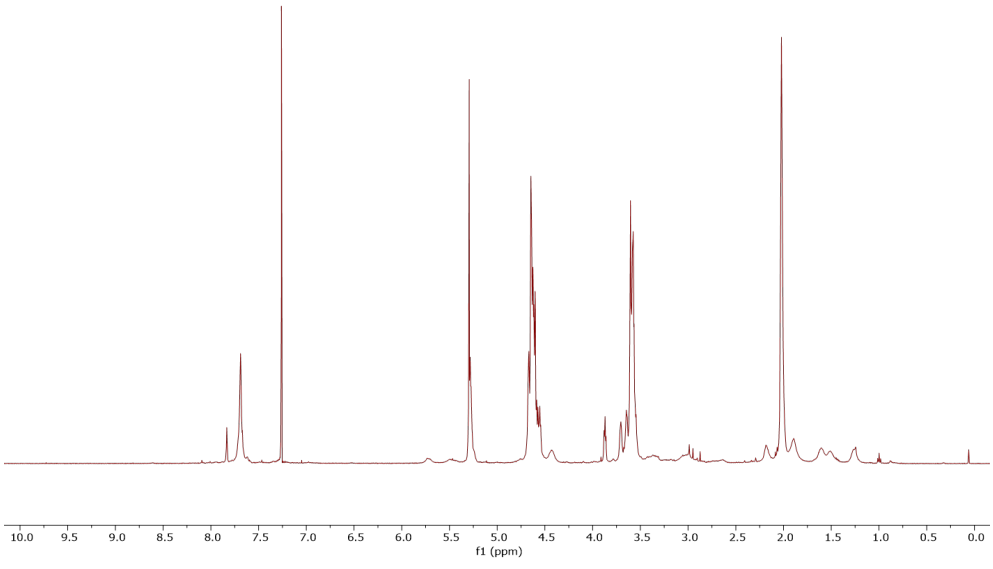

Figure 28. ^{1}H NMR spectrum for **5A-Poly-*S*-Cy** in $CDCl_3$.

2A-Poly-R

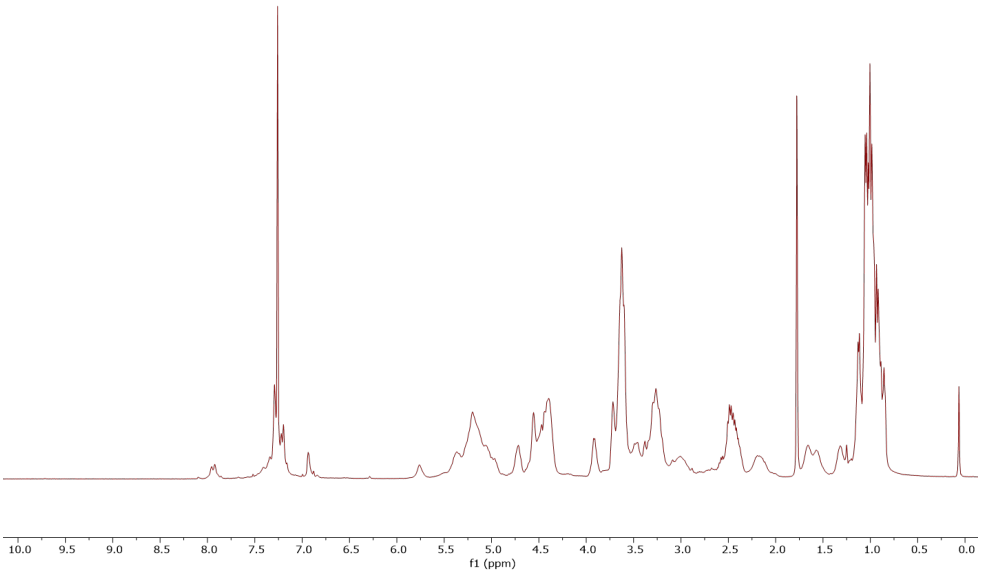

Figure 29. ^{1}H NMR spectrum for **2A-Poly-*R*** in $CDCl_3$.

2A-Poly-S

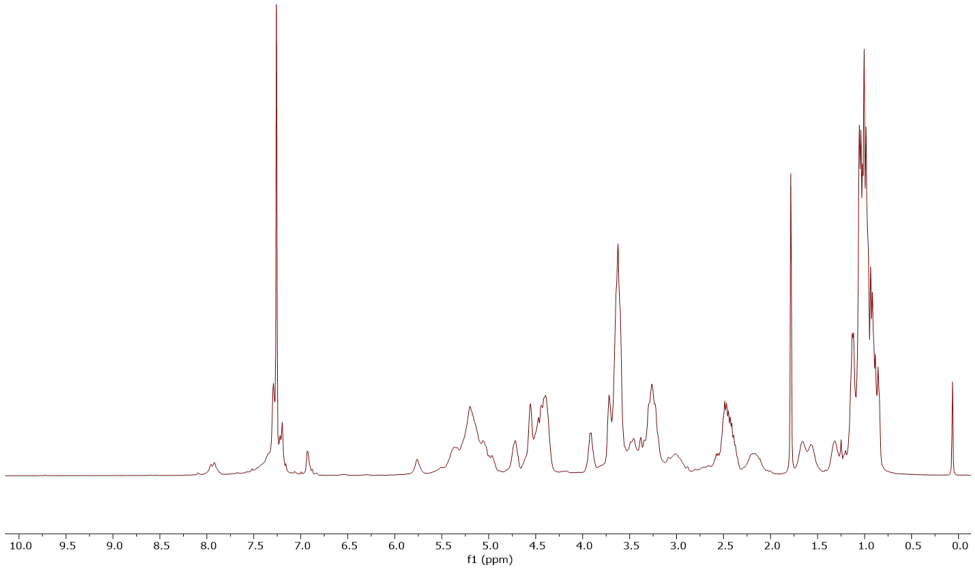

Figure 30. ^{1}H NMR spectrum for **2A-Poly-*S*** in $CDCl_3$.

2A-Poly-R-Cy

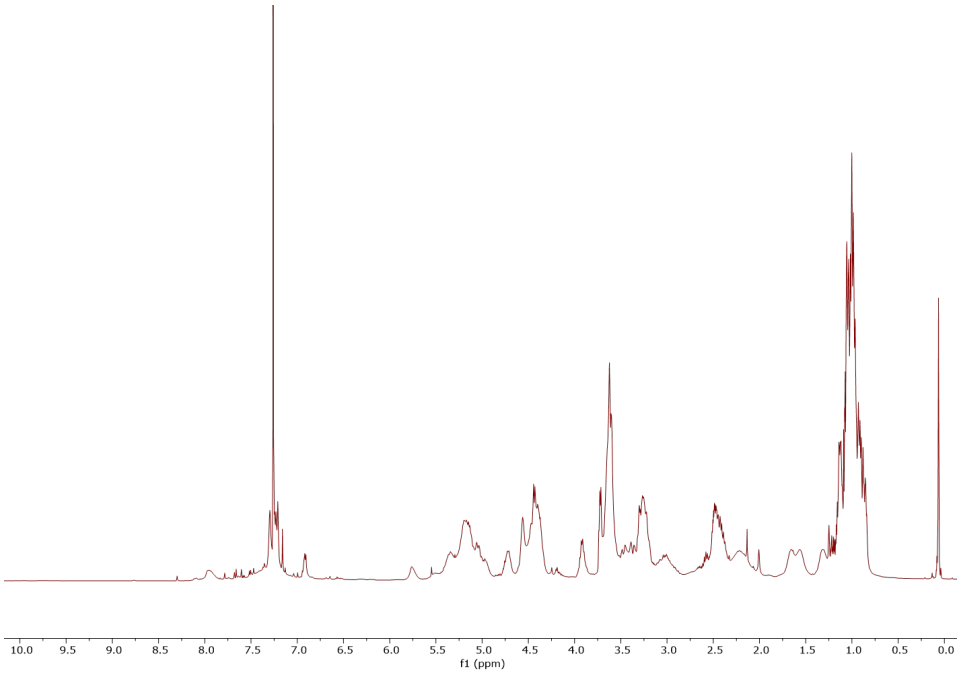

Figure 31. ^{1}H NMR spectrum for **2A-Poly-*R*-Cy** in $CDCl_3$.

2A-Poly-S-Cy

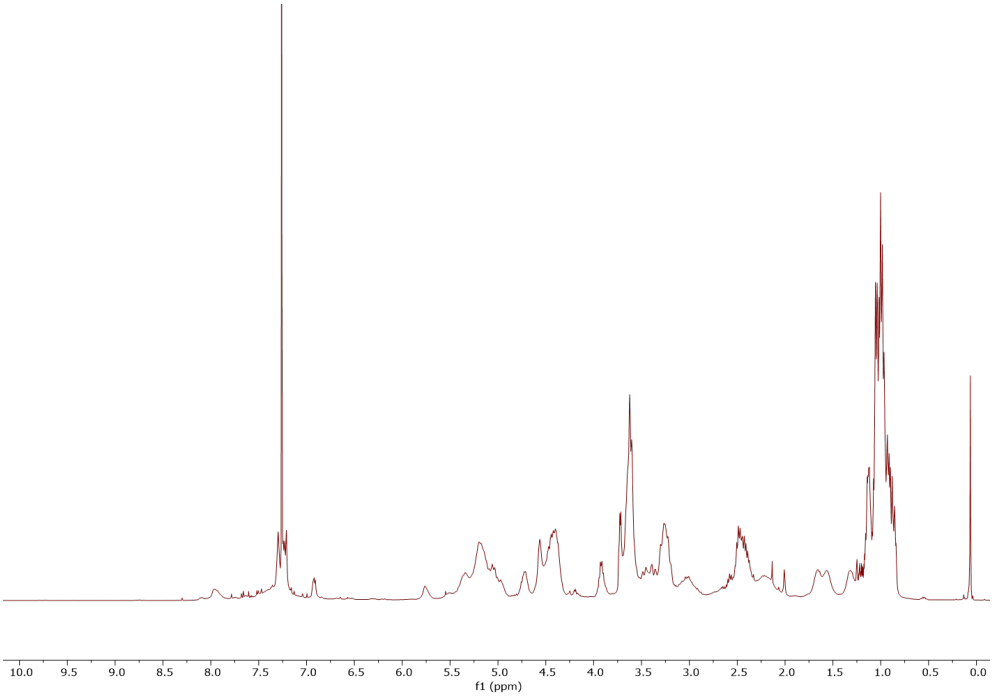

Figure 32. ^{1}H NMR spectrum for **2A-Poly-*S*-Cy** in $CDCl_3$.

Deprotection of MMs and CBPs

NMR

5A-R-OAc-MM

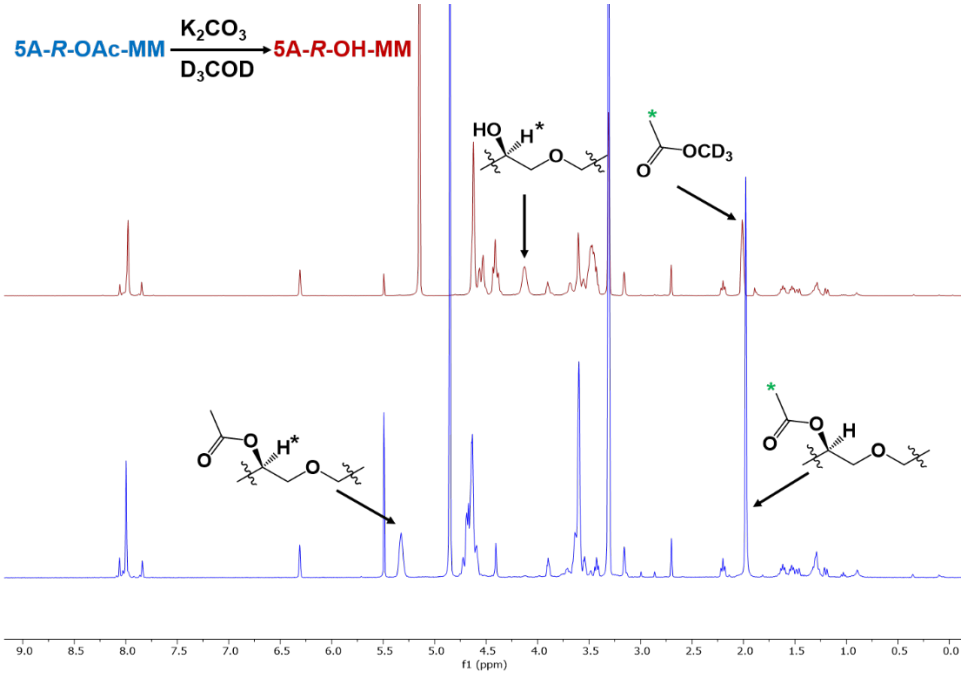

Figure 33. Stacked ^{1}H NMR spectra for the deprotection of **5A-*R*-OAc-MM** in $CDCl_3$.

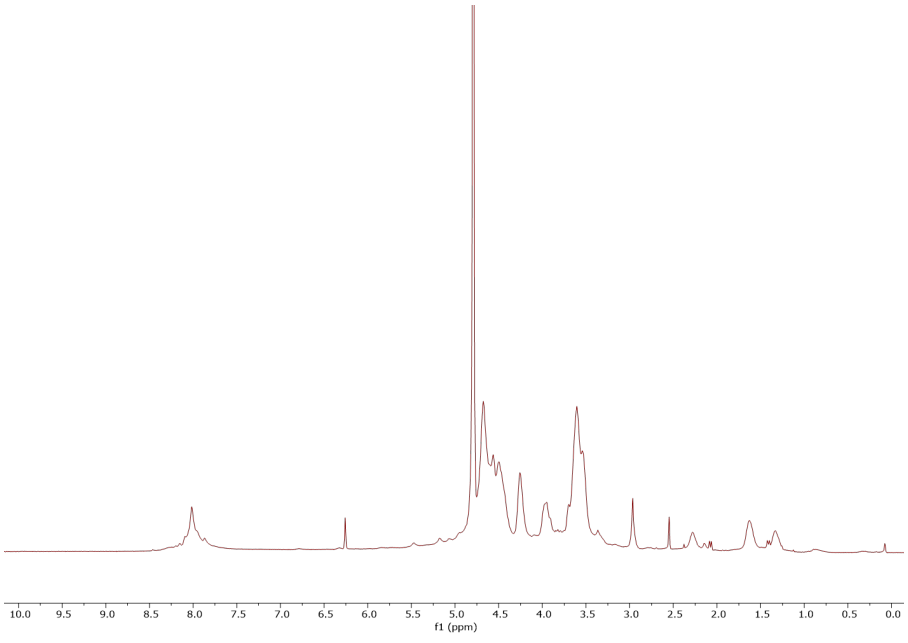

Figure 34. ^{1}H NMR spectrum for **5A-*R*-OH-MM** (deprotected) in D_2O.

5A-S-OAc-MM

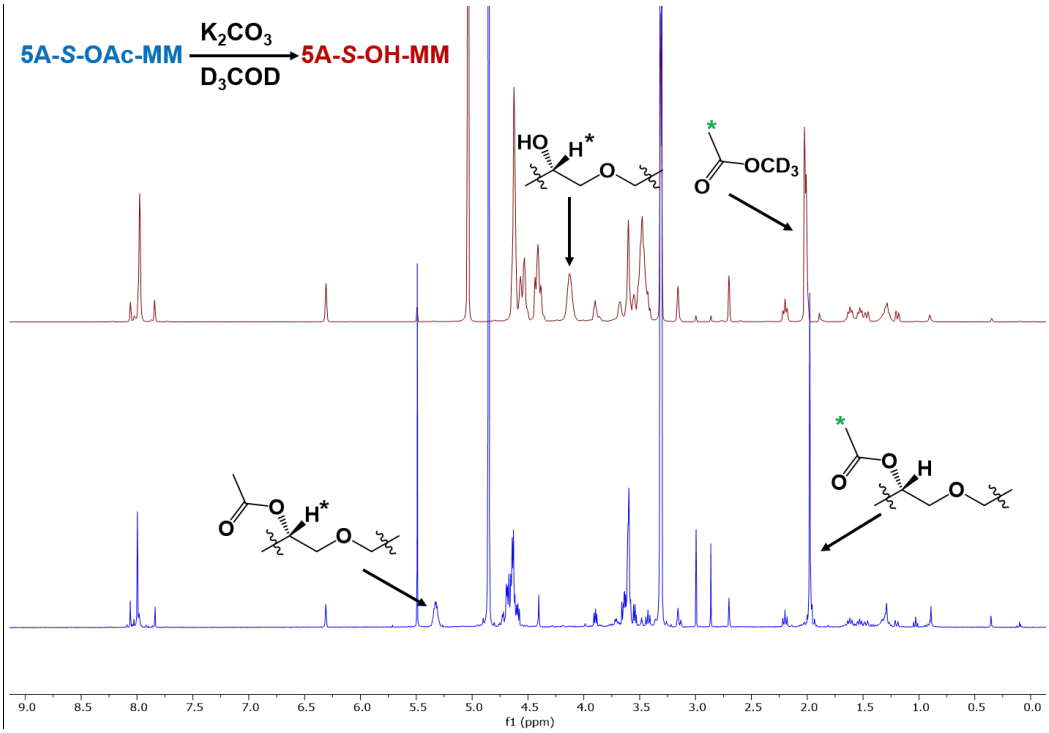

Figure 35. Stacked ^{1}H NMR spectra for the deprotection of **5A-*S*-OAc-MM** in $CDCl_3$.

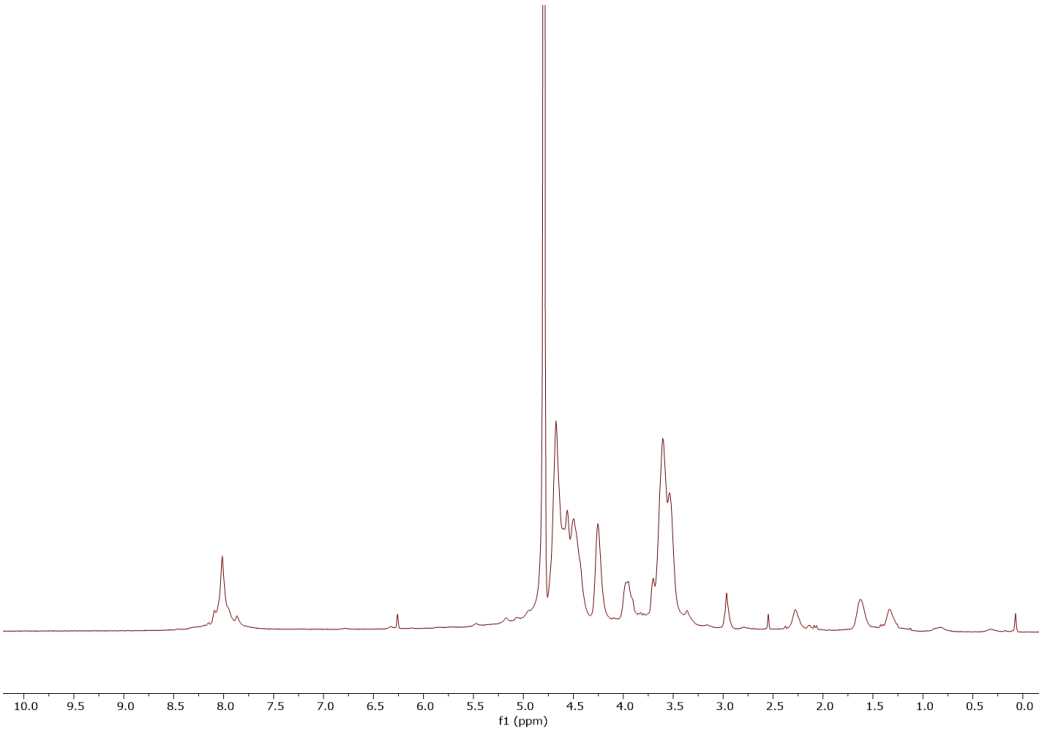

Figure 36. ^{1}H NMR spectrum for **5A-*S*-OH-MM** (deprotected) in D_2O.

2A-R-OAc-MM

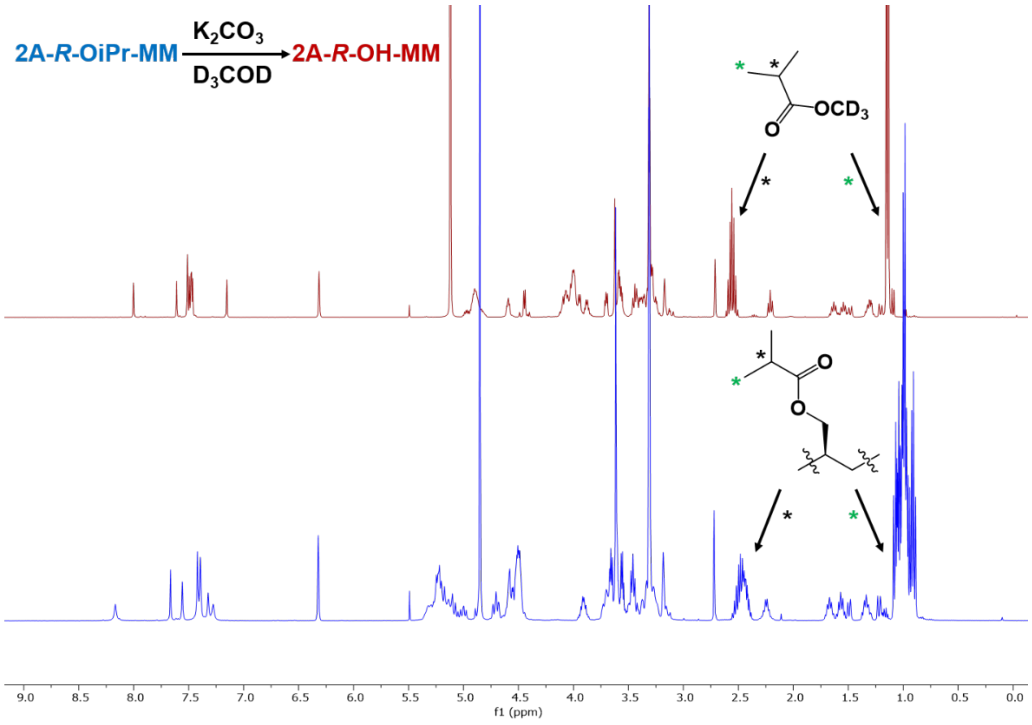

Figure 37. Stacked ^{1}H NMR spectra for the deprotection of **2A-*R*-OiPr-MM** in $CDCl_3$.

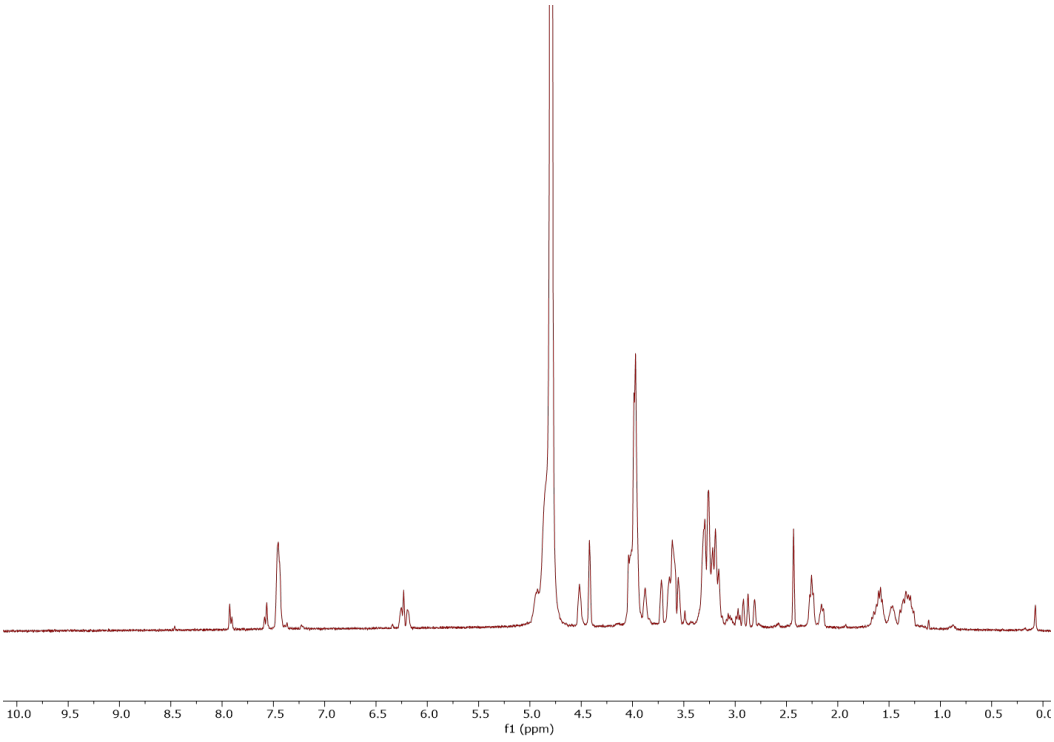

Figure 38. ^{1}H NMR spectrum for **2A-*R*-OH-MM** (deprotected) in D_2O.

2A-S-OAc-MM

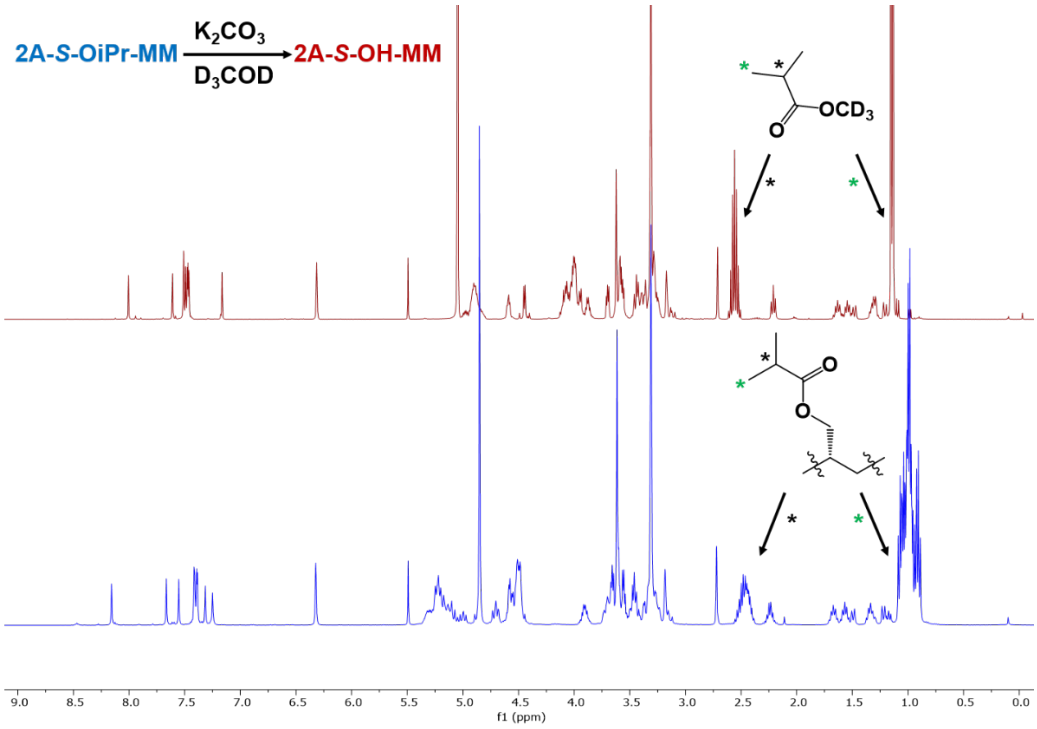

Figure 39. Stacked ^{1}H NMR spectra for the deprotection of **2A-*S*-OiPr-MM** in $CDCl_3$.

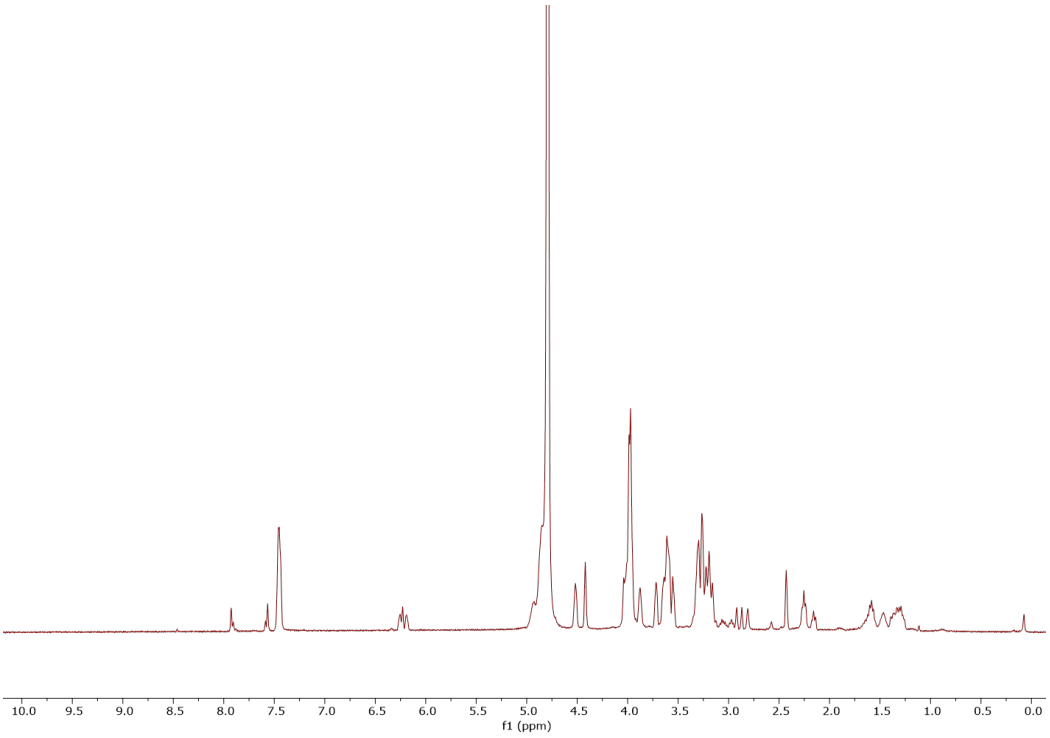

Figure 40. ^{1}H NMR spectrum for **2A-*S*-OH-MM** (deprotected) in D_2O.

5A-R

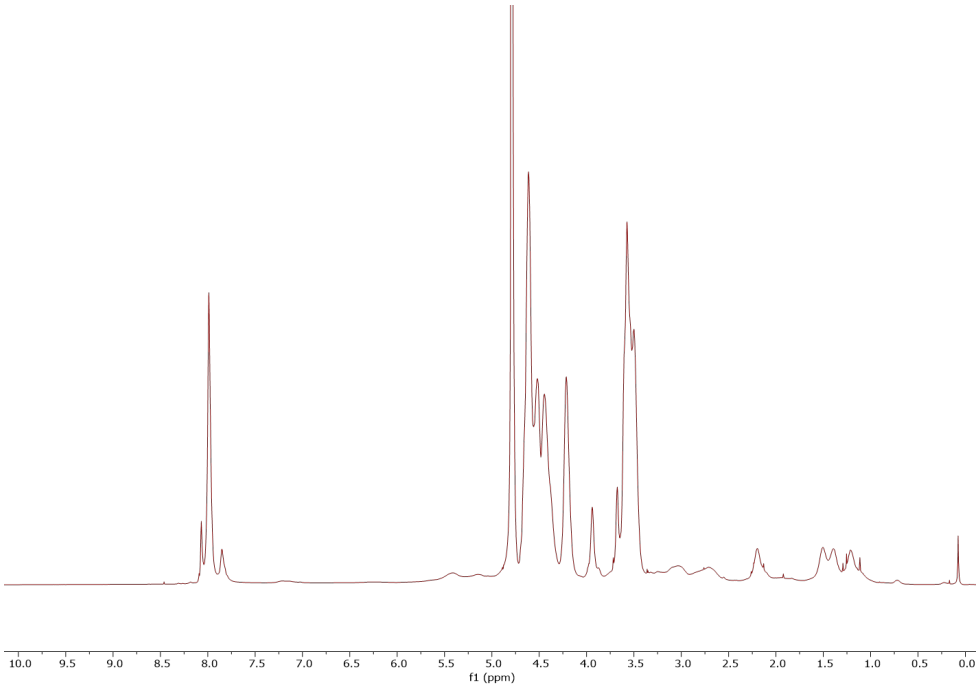

Figure 41. ^{1}H NMR spectrum for **5A-*R*** in D_2O.

5A-S

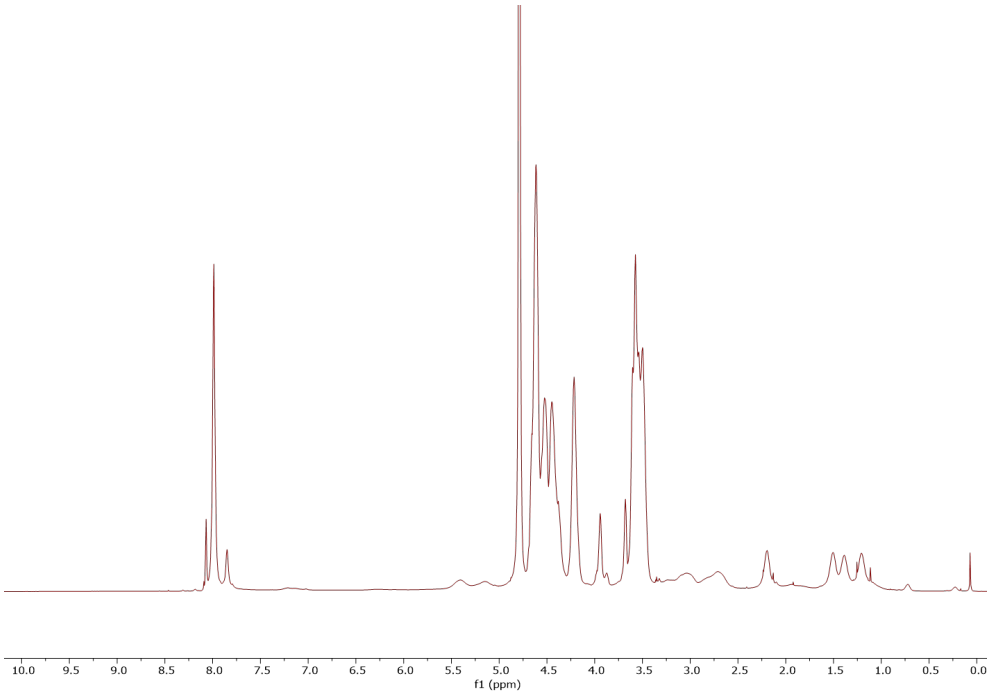

Figure 42. ^{1}H NMR spectrum for **5A-*S*** in D_2O.

5A-R-Cy

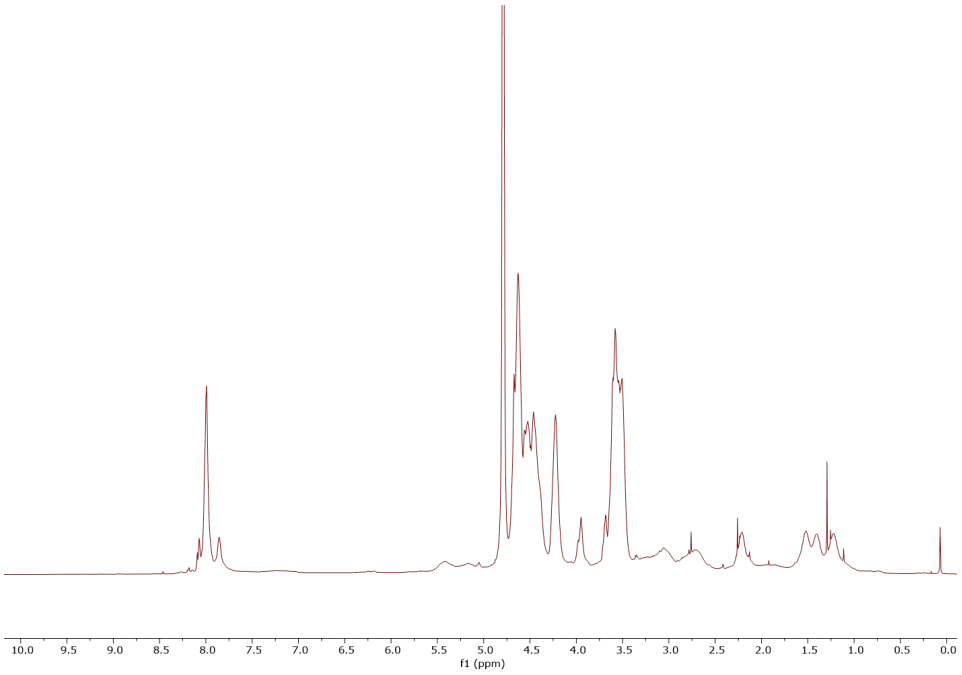

Figure 43. ^{1}H NMR spectrum for **5A-*R*-Cy** in D_2O.

5A-S-Cy

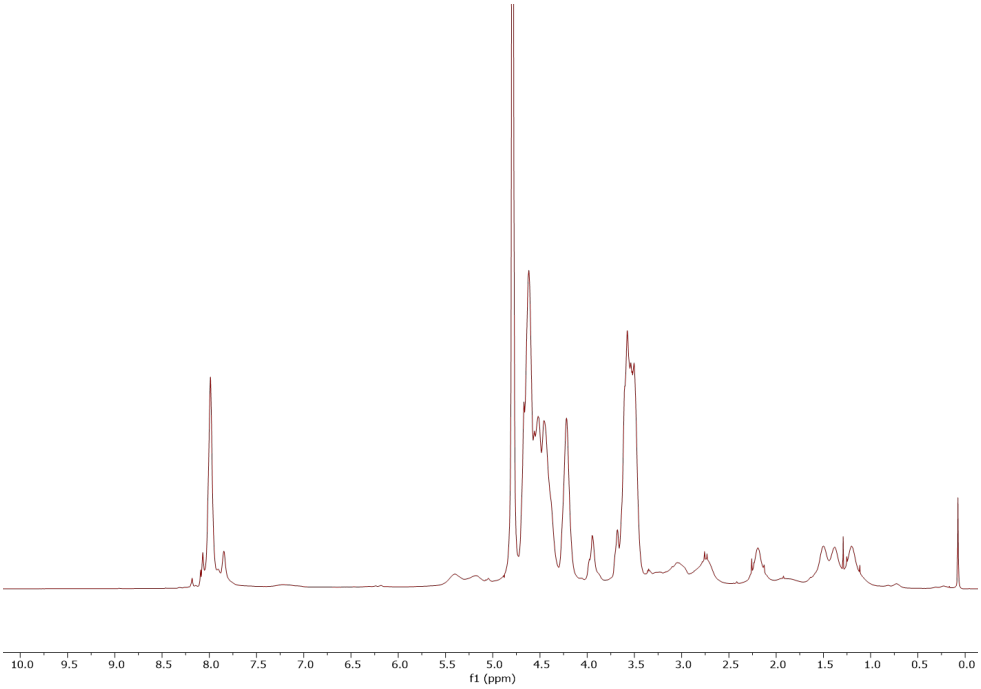

Figure 44. ^{1}H NMR spectrum for **5A-*S*-Cy** in D_2O.

2A-R

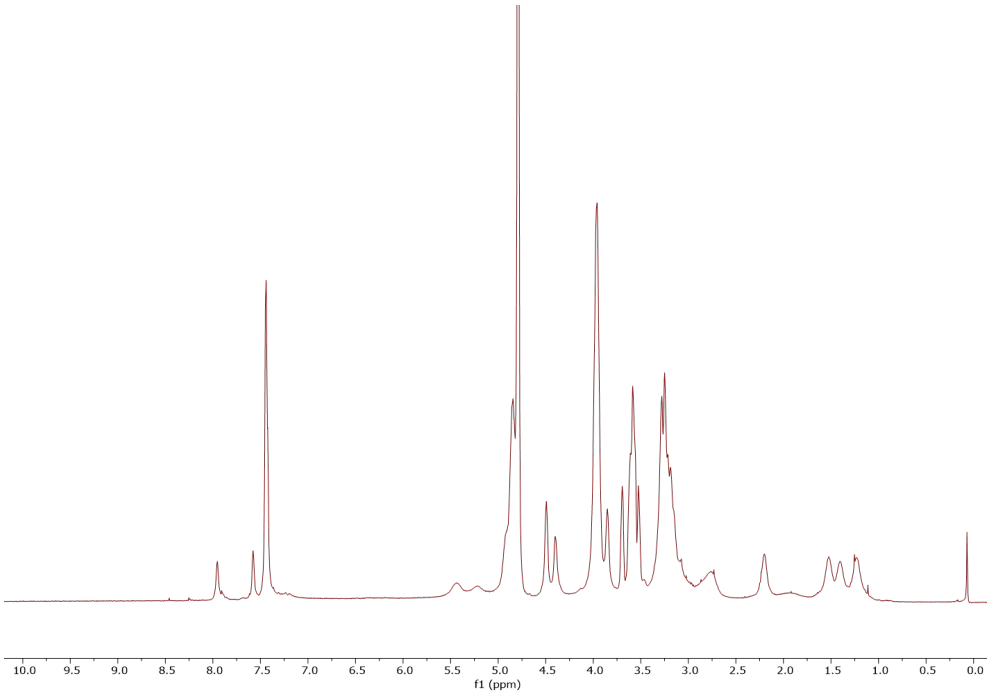

Figure 45. ^{1}H NMR spectrum for **2A-*R*** in D_2O.

2A-S

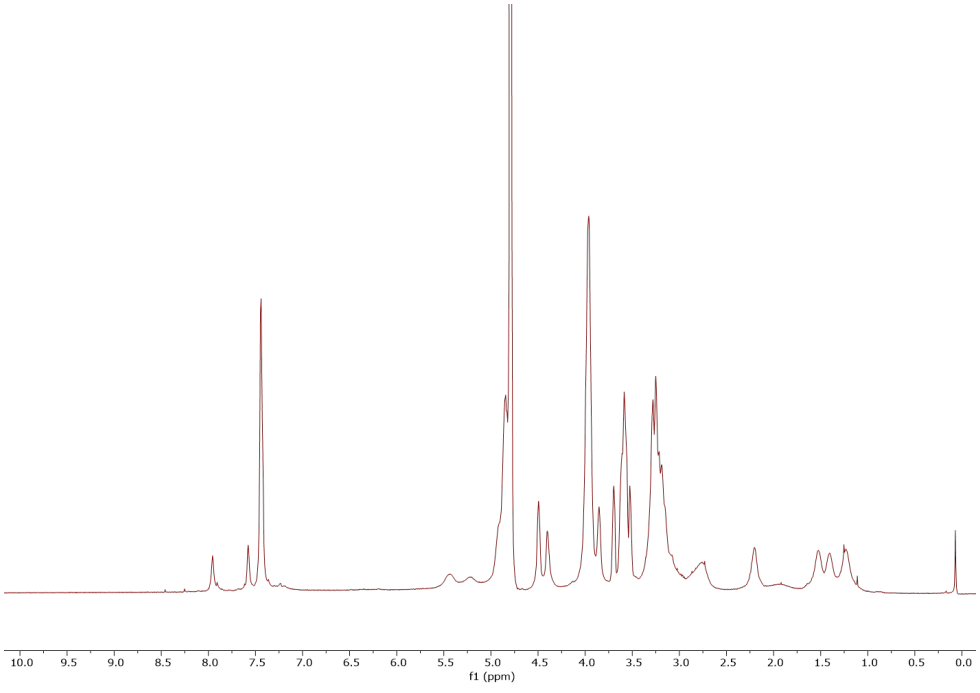

Figure 46. ^{1}H NMR spectrum for **2A-*S*** in D_2O.

2A-R-Cy

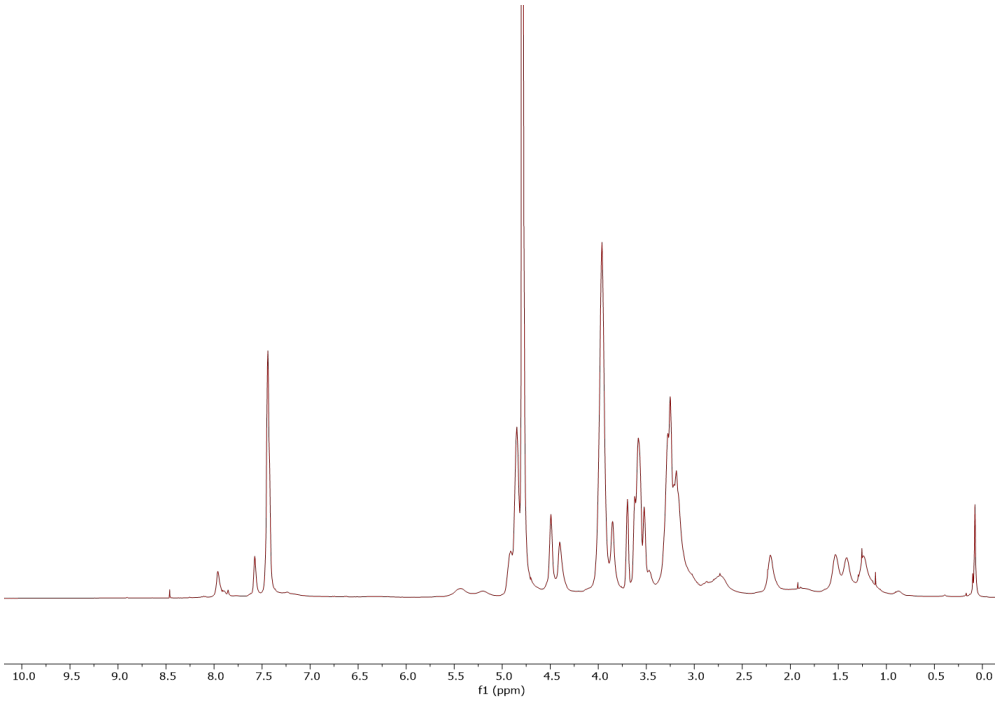

Figure 47. ^{1}H NMR spectrum for **2A-*R*-Cy** in D_2O.

2A-S-Cy

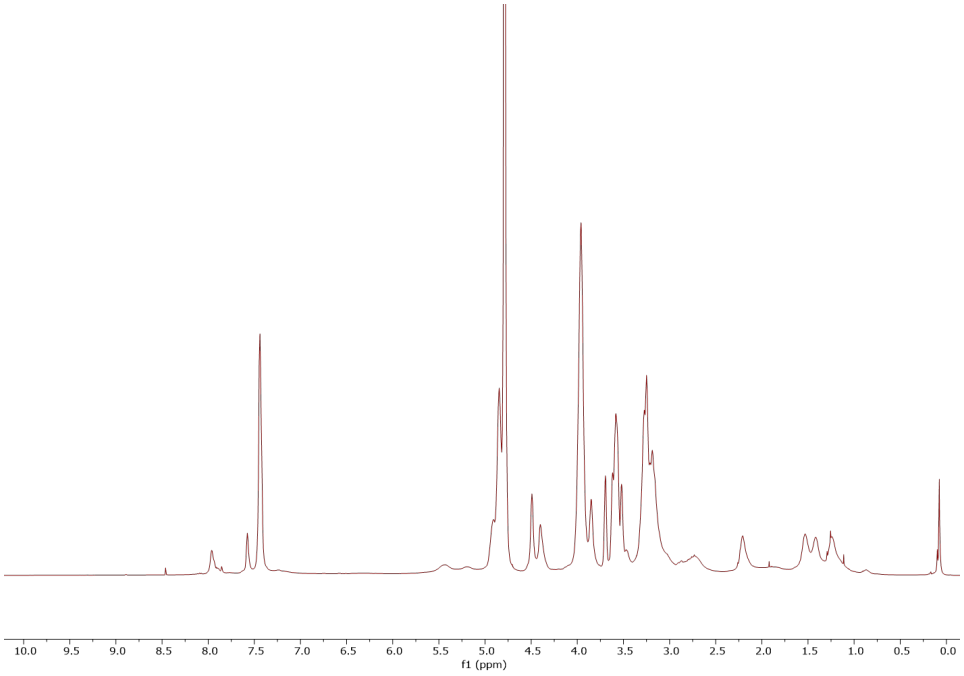

Figure 48. ^{1}H NMR spectrum for **2A-*S*-Cy** in D_2O.

Fourier-Transform Infrared (FT-IR) Spectroscopy

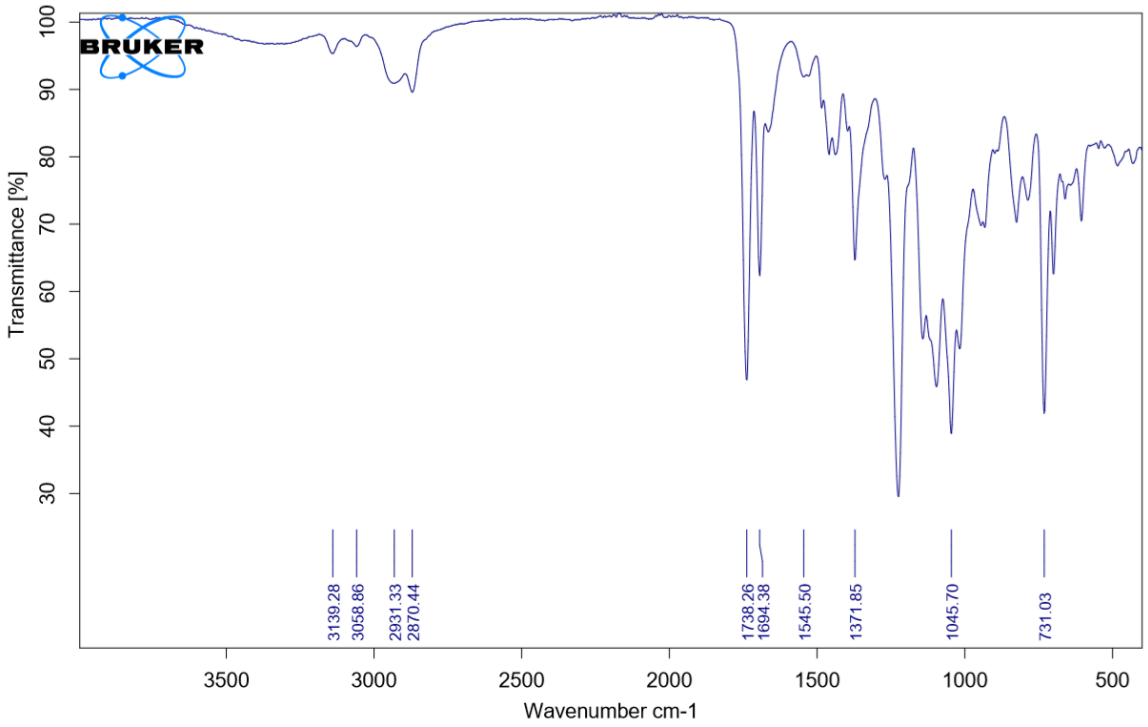

Figure 49. FT-IR spectrum for **5A-Poly-*R***.

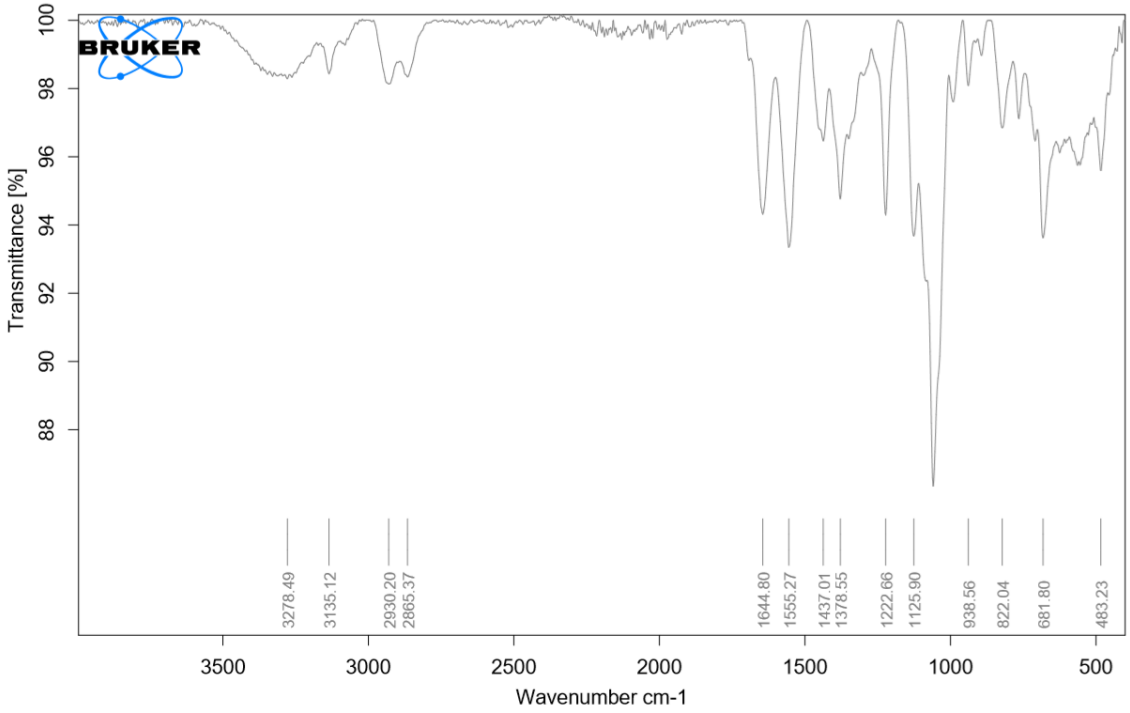

Figure 50. FT-IR spectrum for **5A-*R***.

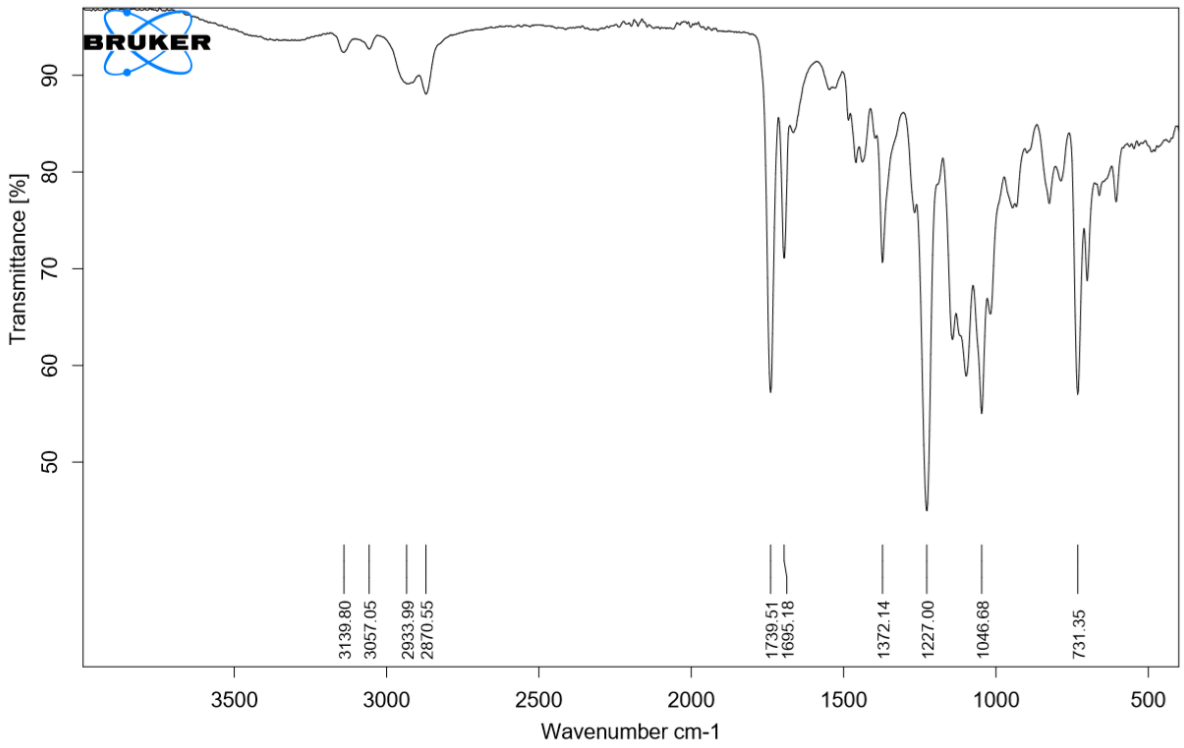

Figure 51. FT-IR spectrum for **5A-Poly-*S***.

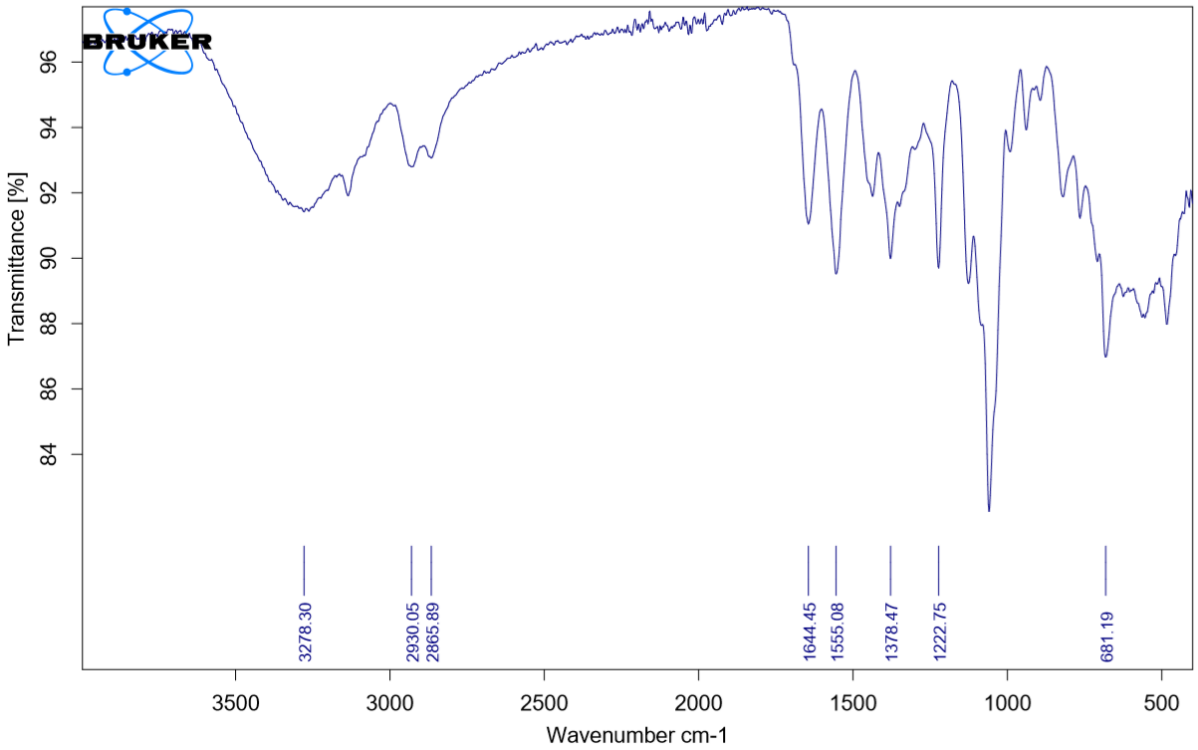

Figure 52. FT-IR spectrum for **5A-*S***.

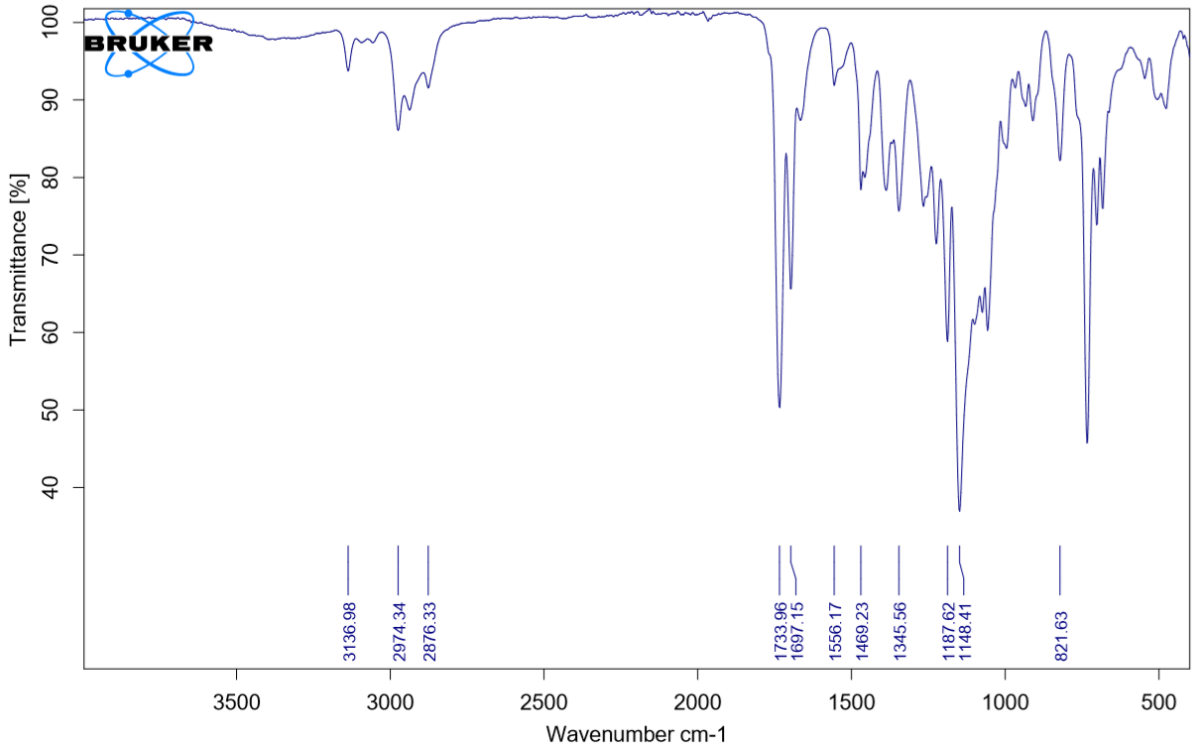

Figure 53. FT-IR spectrum for **2A-Poly-*R***.

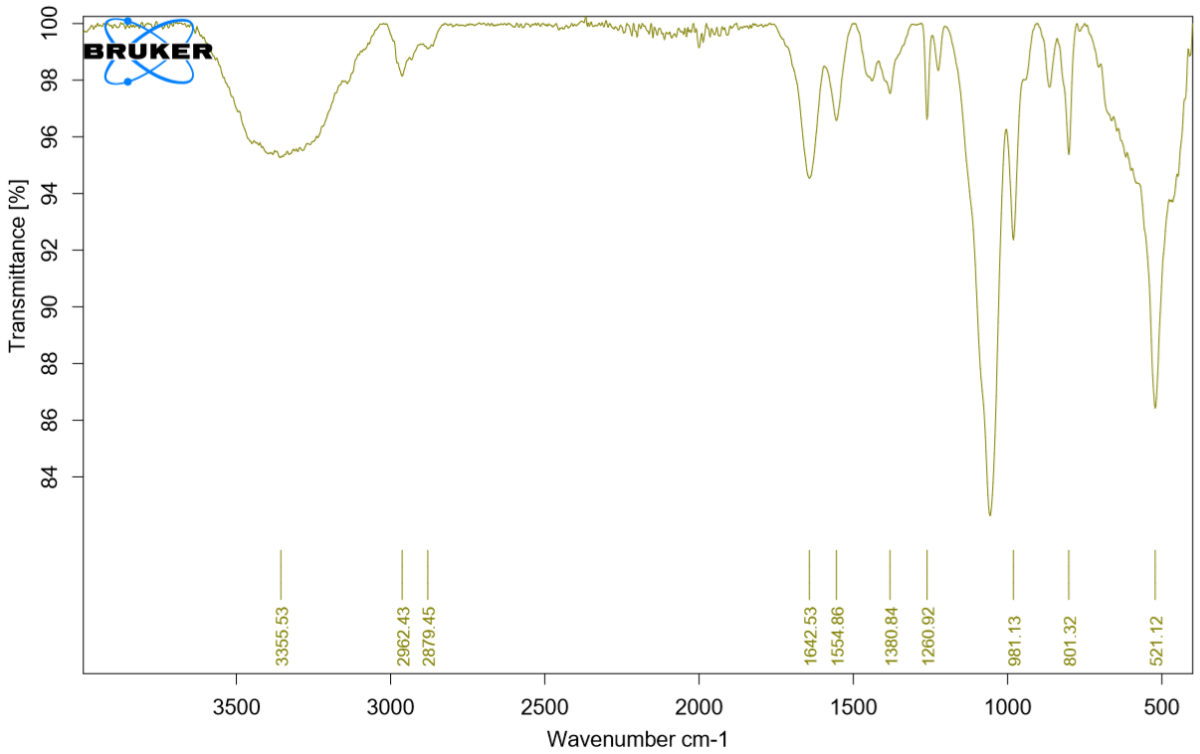

Figure 54. FT-IR spectrum for **2A-*R***.

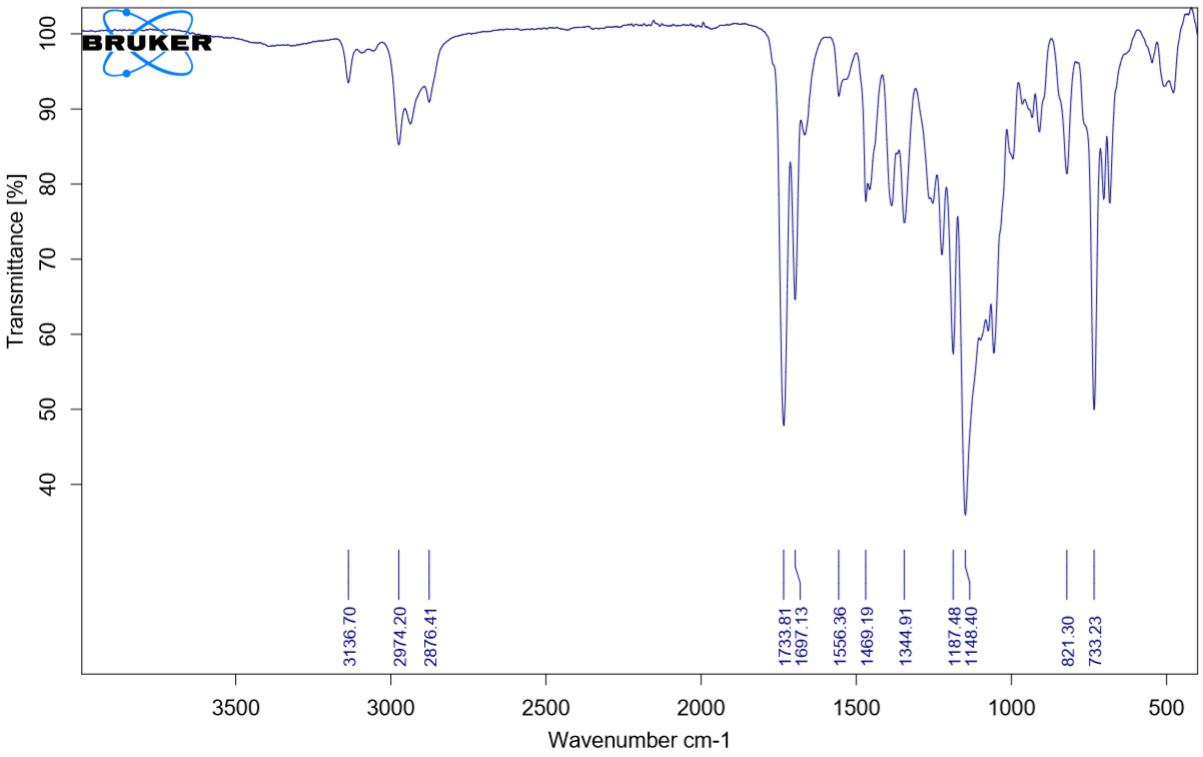

Figure 55. FT-IR spectrum for **2A-Poly-*S***.

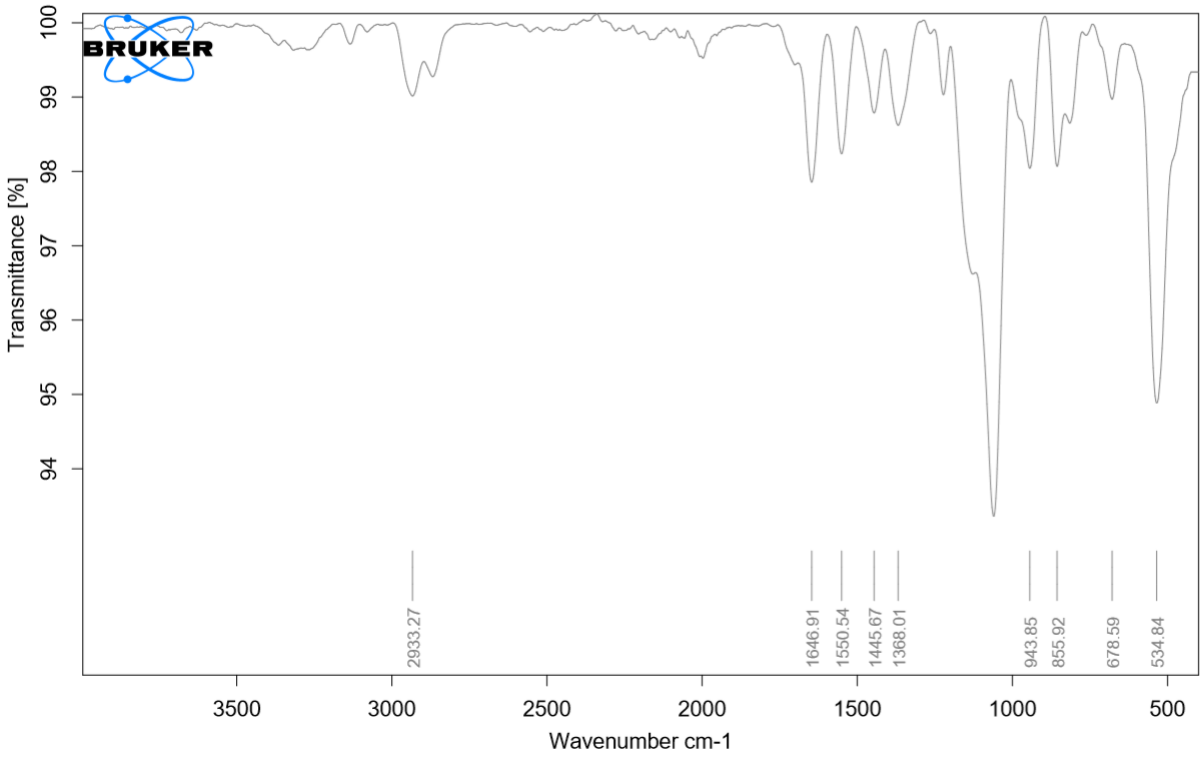

Figure 56. FT-IR spectrum for **2A-*S***.

Dynamic Light Scattering (DLS) of Chiral Bottlebrush Polymers (CBPs)

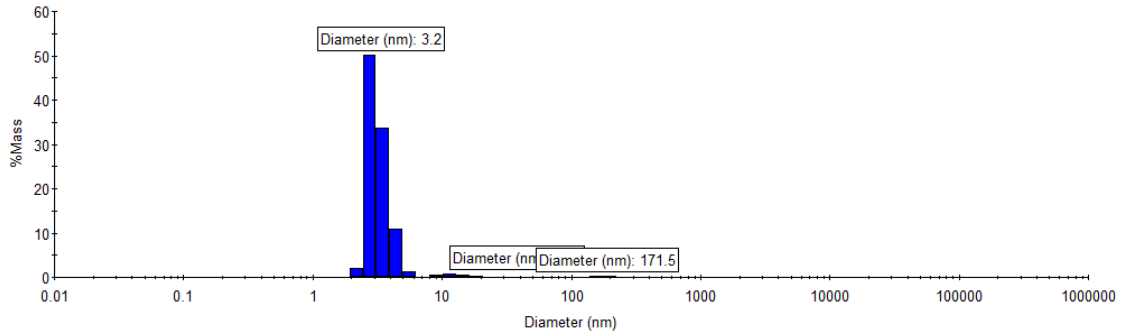

Figure 57. Dynamic light scattering (DLS) histogram for **5A-*R*** with peaks at 3.2 ± 0.6 nm (97.9%), 12.1 ± 2.7 nm (1.7%), and 171.5 ± 32.6 nm (0.4%).

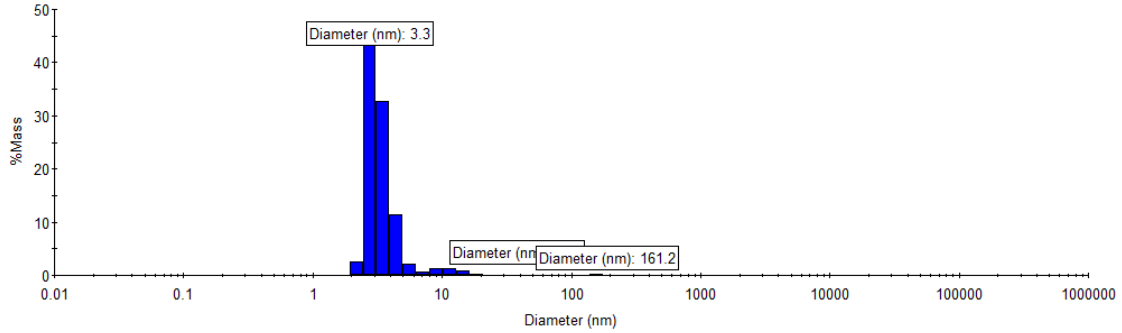

Figure 58. DLS histogram for **5A-*S*** with peaks at 3.3 ± 0.7 nm (96.3%), 11.8 ± 2.9 nm (3.5%), and 161.2 ± 27.2 nm (0.2%).

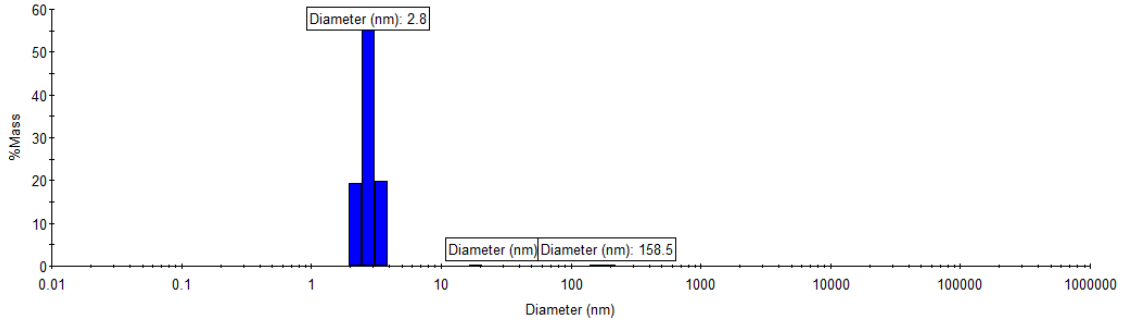

Figure 59. DLS histogram for **2A-*R*** with peaks at 2.8 ± 0.4 nm (99.0%), 20.4 ± 2.7 nm (0.3%), and 158.4 ± 33.9 nm (0.8%).

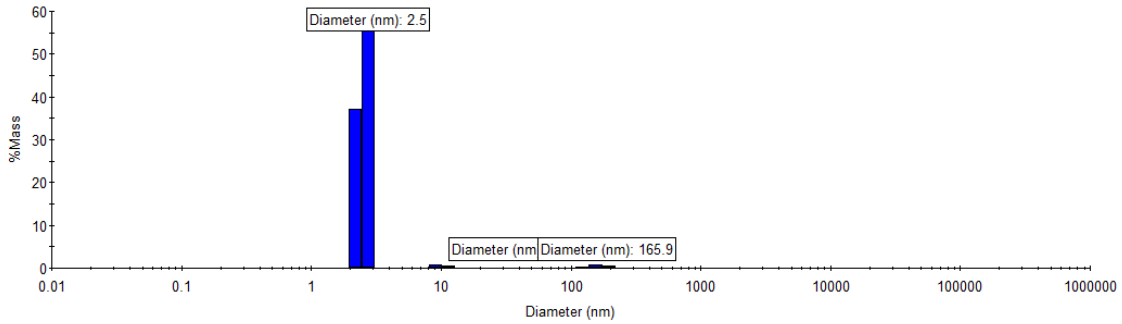

Figure 60. DLS histogram for **2A-*S*** with peaks at 2.5 ± 0.3 nm (97.0%), 10.0 ± 1.2 nm (1.4%), and 165.9 ± 14.6 nm (1.7%).

Fluorescent Monomer (Cy5.5-M)

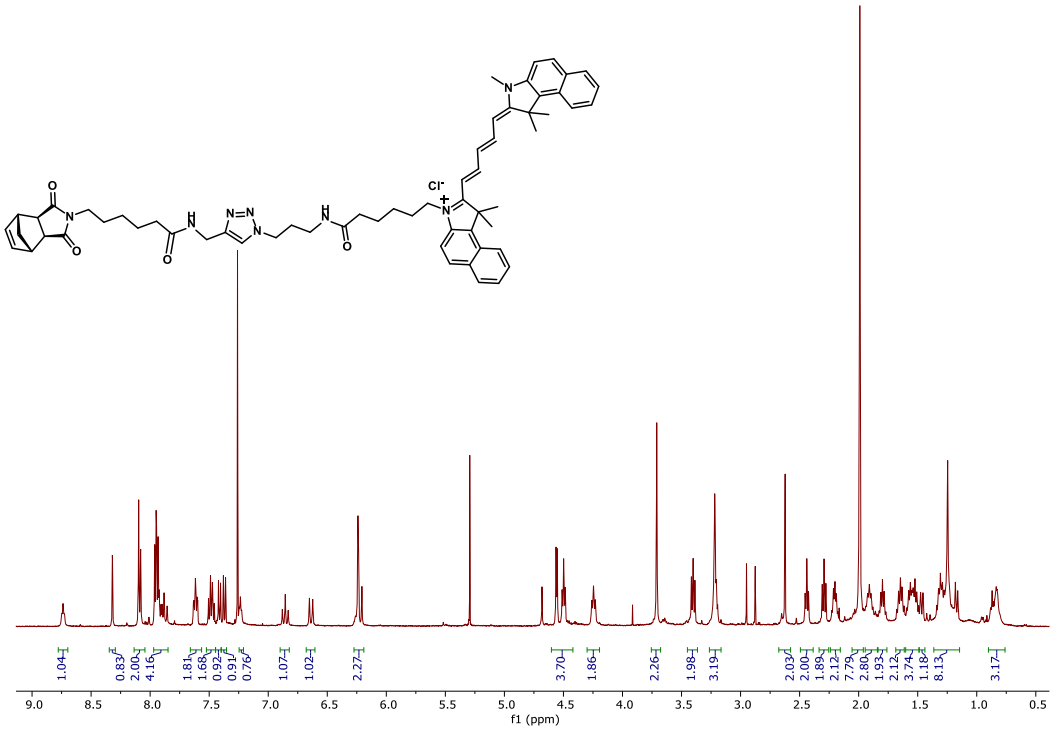

Figure 61. ^{1}H NMR spectrum for **Cy5.5-M** in $CDCl_3$.

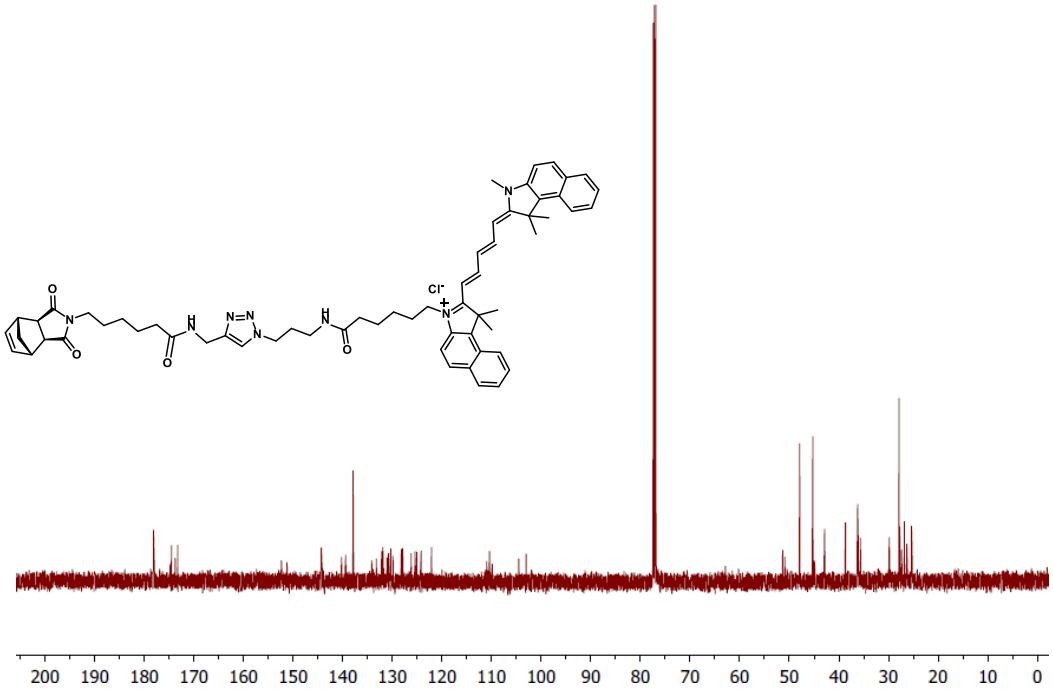

Figure 62. ^{13}C NMR spectrum for **Cy5.5-M** in $CDCl_3$.

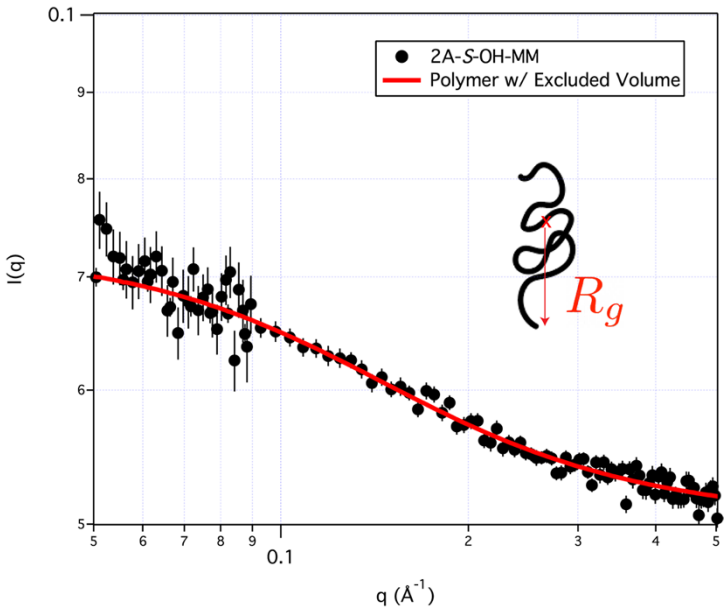

Figure 63. SANS measurements of **2A-*S*-OH-MM** in D_2O prior to polymerization. The solid line is a best fit according to a form factor of a polymer chain with excluded volume. The inset depicts the physical interpretation of the radius of gyration. The experiment was performed once. Data are presented as mean ± standard deviation, with error bars corresponding to one standard deviation in the intensity, calculated as the square root of the number of counts.

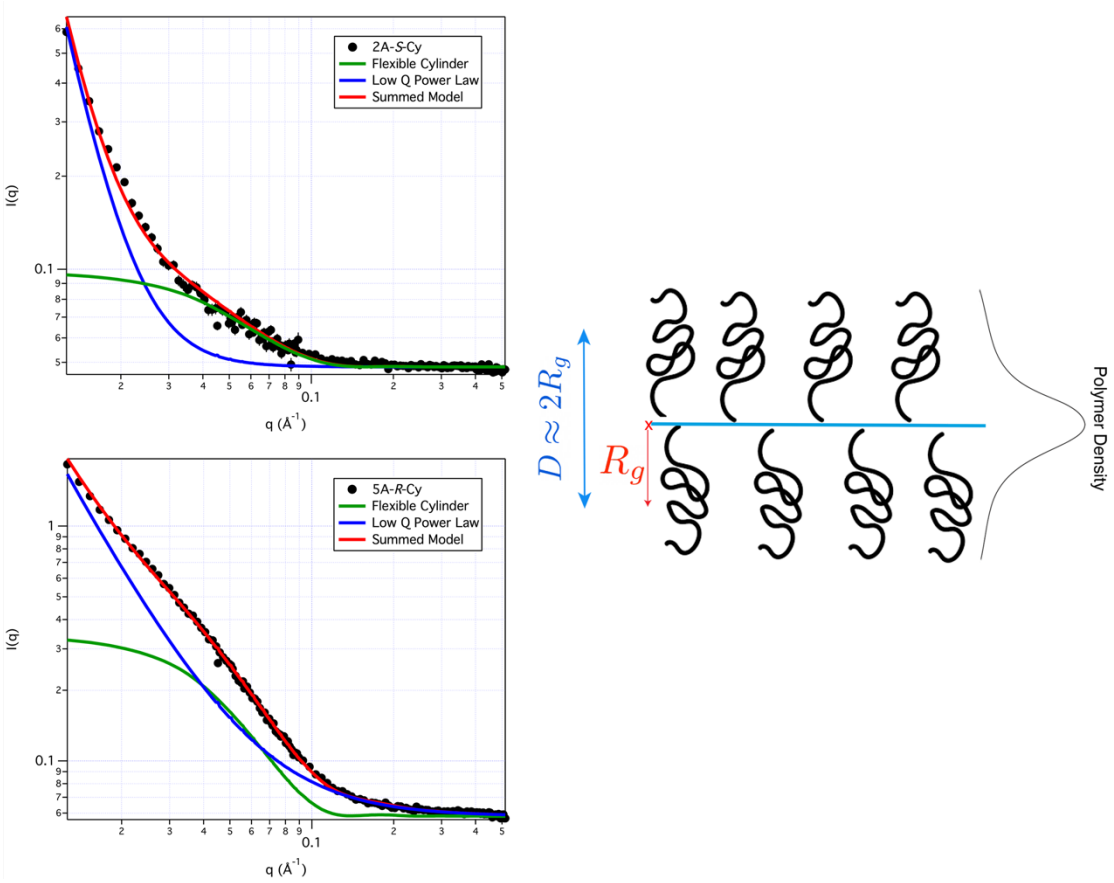

Figure 64. SANS measurements of CBPs (top) **2A-*S*-Cy** and (bottom) **5A-*R*-Cy**. The data were fit to a model consisting of a flexible cylinder, and a power law at low-q which accounts for clustering of polymers in solution. The illustration depicts the physical interpretation of the radius and diameter of the bottlebrushes in terms of the polymer density (flexible cylinder model) and the radius of gyration of the macromonomer. The experiment was performed once. Data are presented as mean ± standard deviation, with error bars corresponding to one standard deviation in the intensity, calculated as the square root of the number of counts.

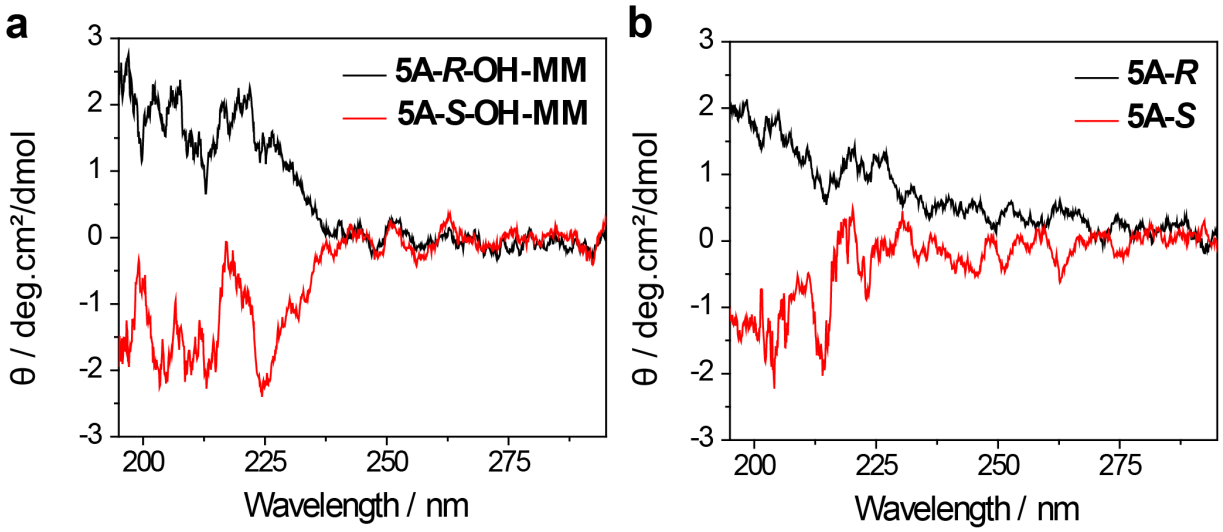

Figure 65. Circular dichroism (CD) spectra for **a.** MMs **5A-*R*-OH-MM** and **5A-*S*-OH-MM** and **b.** CBPs **5A-*R*** and **5A-*S***.

a

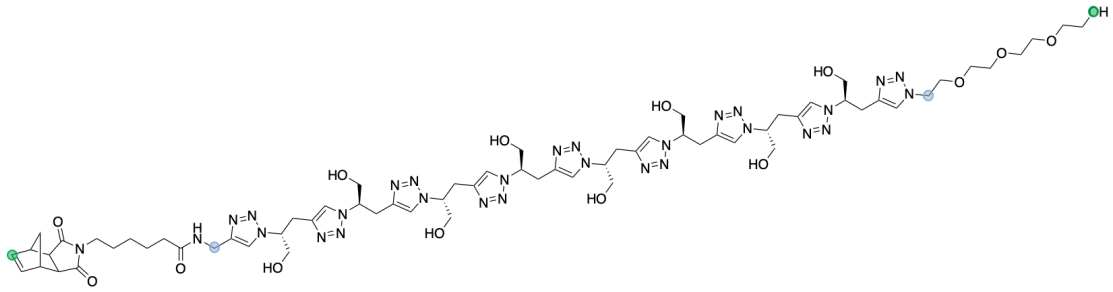

b

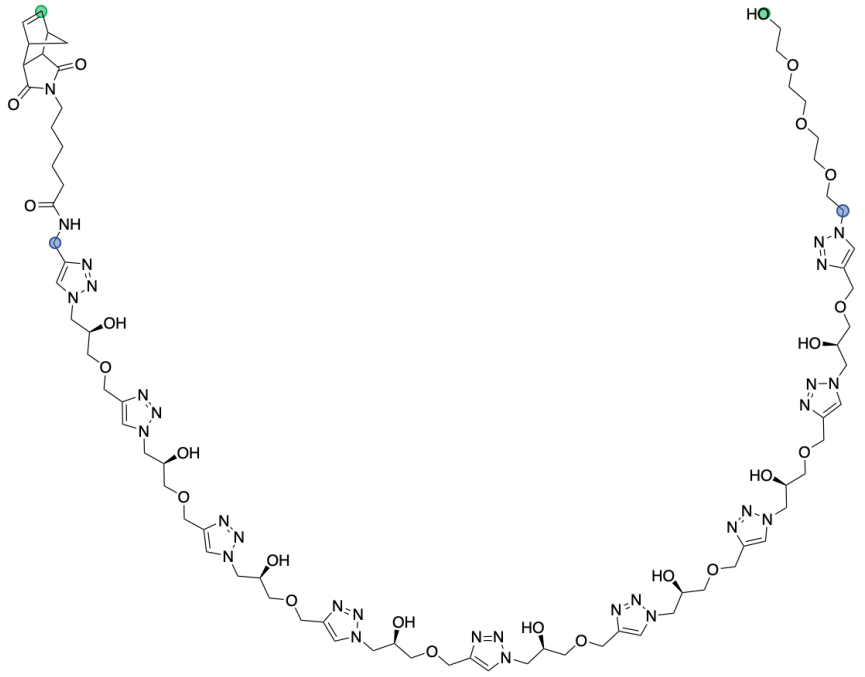

Figure 66. a. 2A-*R*-OH-MM and **b. 5A-*R*-OH-MM** MMs synthesized in this study and modeled using MD. The green dots (●) indicate the chain ends, and the blue dots (●) mark a section of the chains for further analysis.

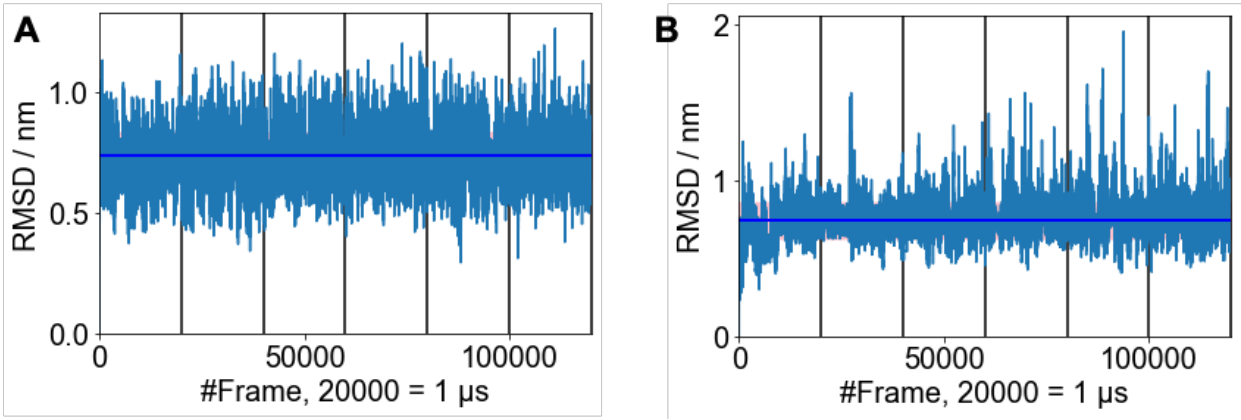

Figure 67. Variation of root mean square distance (RMSD) of the structure from the initial structure, for **a. 2A-*R*-OH-MM** and **b. 5A-*R*-OH-MM**. The plot is generated using a concatenated trajectory of 120,000 frames, with 20,000 frames (1 µs) per replicate. After concatenation, all frames are aligned with the first frame. The blue lines represent the mean of the respective parameters. The overlay in pink represents mean ± standard deviation.

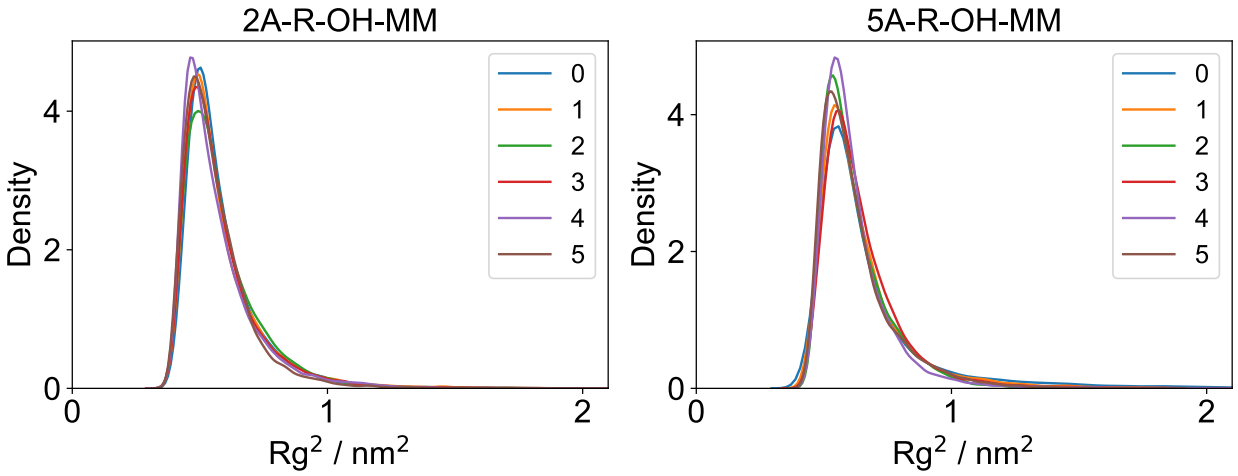

Figure 68. Distribution of radius of gyration - squared (R_g^2) for **2A-*R*-OH-MM** and **5A-*R*-OH-MM** replicates.

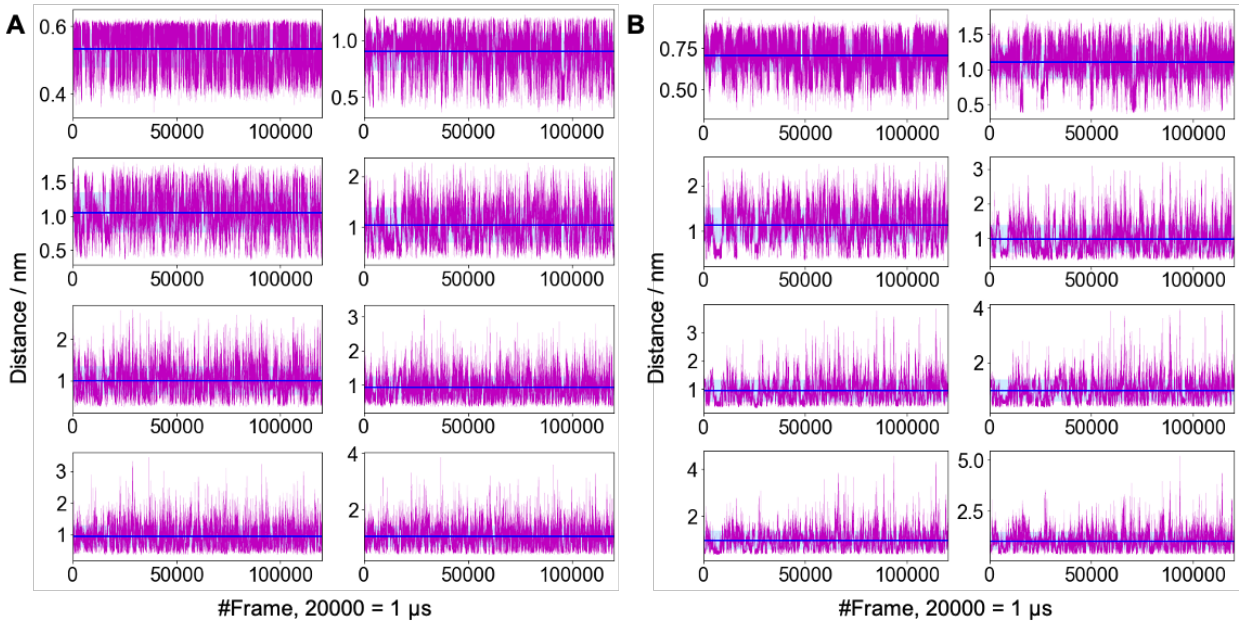

Figure 69. End-to-end distance between the C-atom on consecutive triazole units for **a. 2A-*R*-OH-MM** and **b. 5A-*R*-OH-MM**. The blue lines represent the mean of the respective parameters. The overlay in blue represents mean ± standard deviation. The plot is generated using a concatenated trajectory of 120,000 frames, with 20,000 frames (1 µs) per replicate.

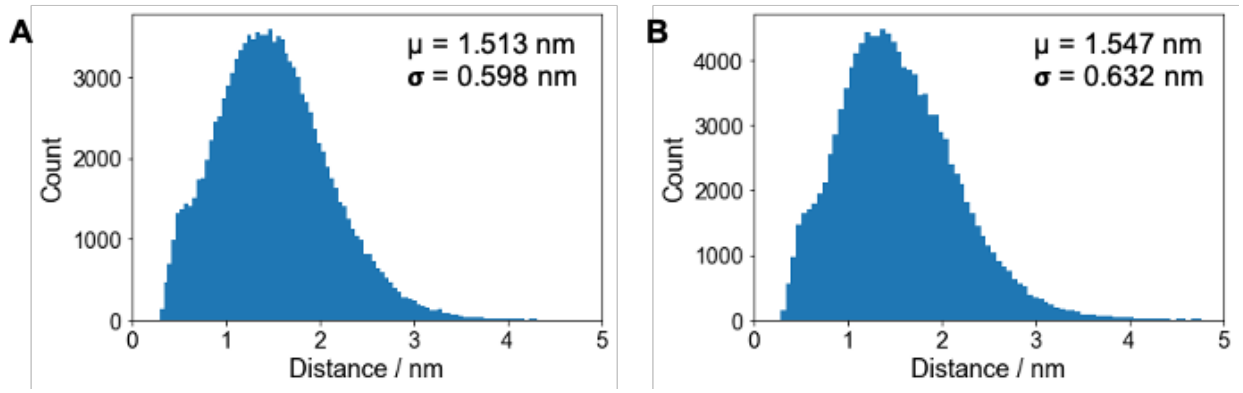

Figure 70. End-to-end distance between the chain ends for **a. 2A-*R*-OH-MM** and **b. 5A-*R*-OH-MM**. Statistical significance analysis for distances between chain ends for 2A-R-OH-MM and 5A-R-OH-MM using Welch's two-sided *t*-test resulted in *p*-value of 5.437E-41 and *t*-statistic of -13.410. The plot is generated using a concatenated trajectory of 120,000 frames, with 20,000 frames (1 µs) per replicate.

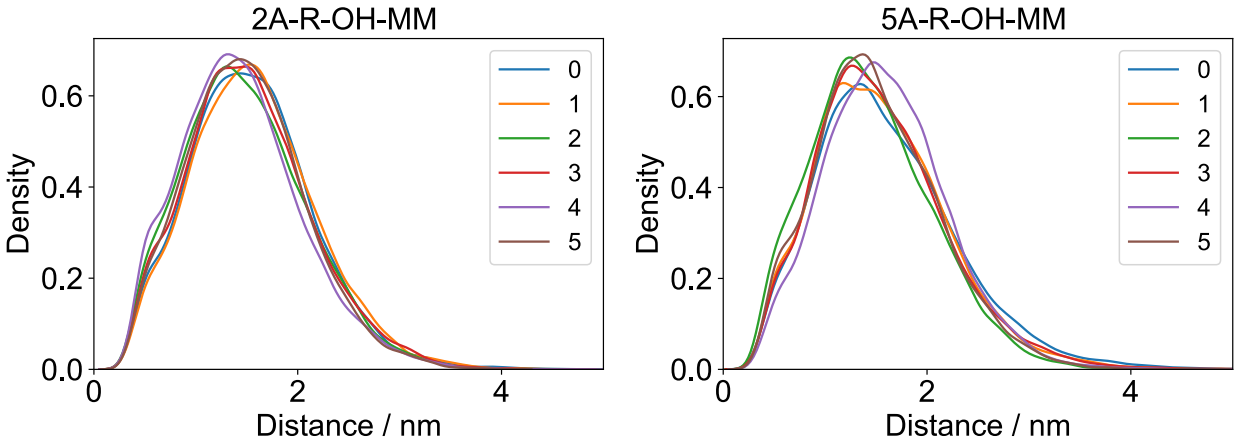

Figure 71. Distribution of chain end-to-end distance for **2A-*R*-OH-MM** and **5A-*R*-OH-MM** replicates.

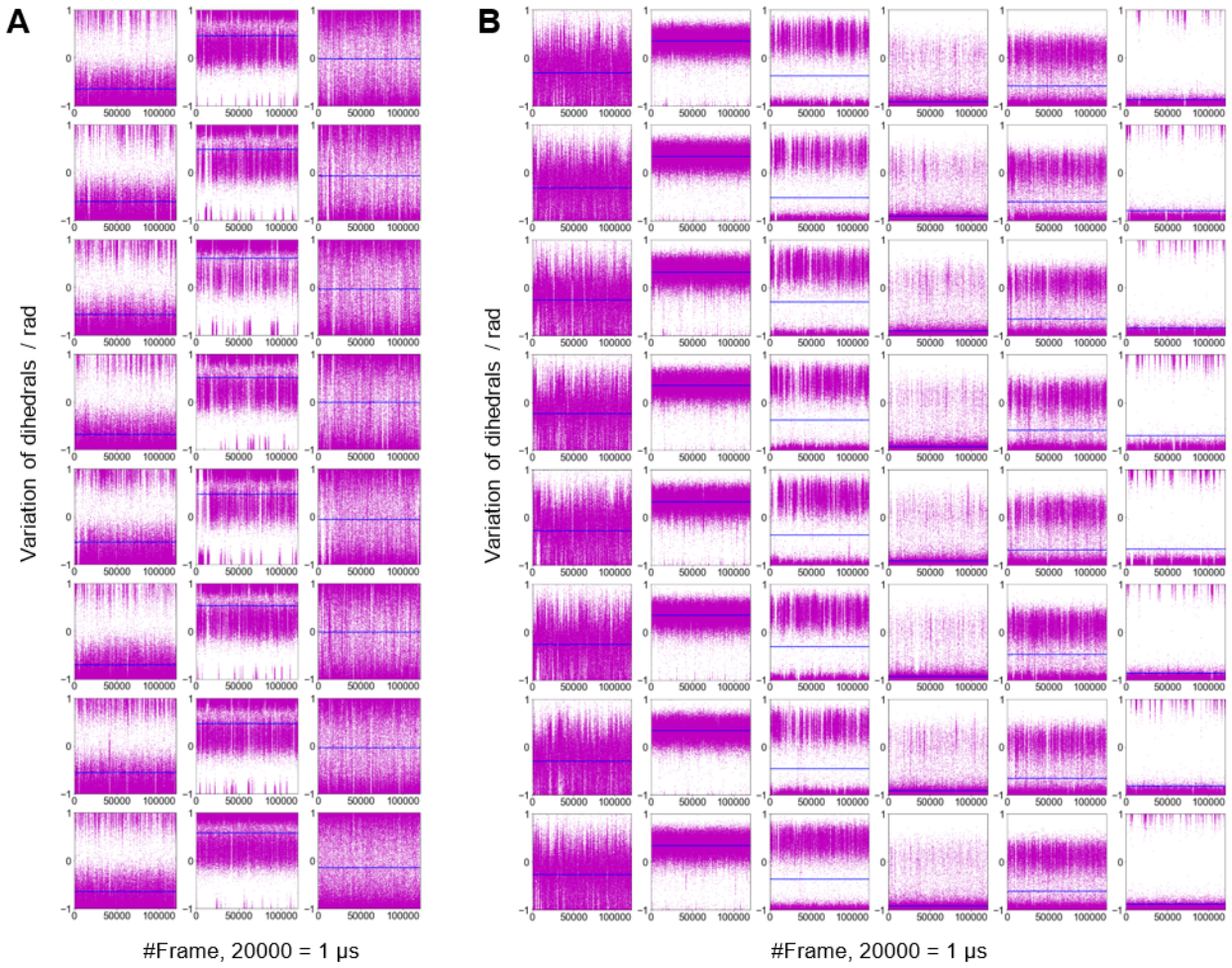

Figure 72. Variation of dihedral angles for the bonds between the triazole units along the backbone of the chain, for **a. 2A-*R*-OH-MM** and **b. 5A-*R*-OH-MM**. The plot is generated using a concatenated trajectory of 120,000 frames, with 20,000 frames (1 µs) per replicate.

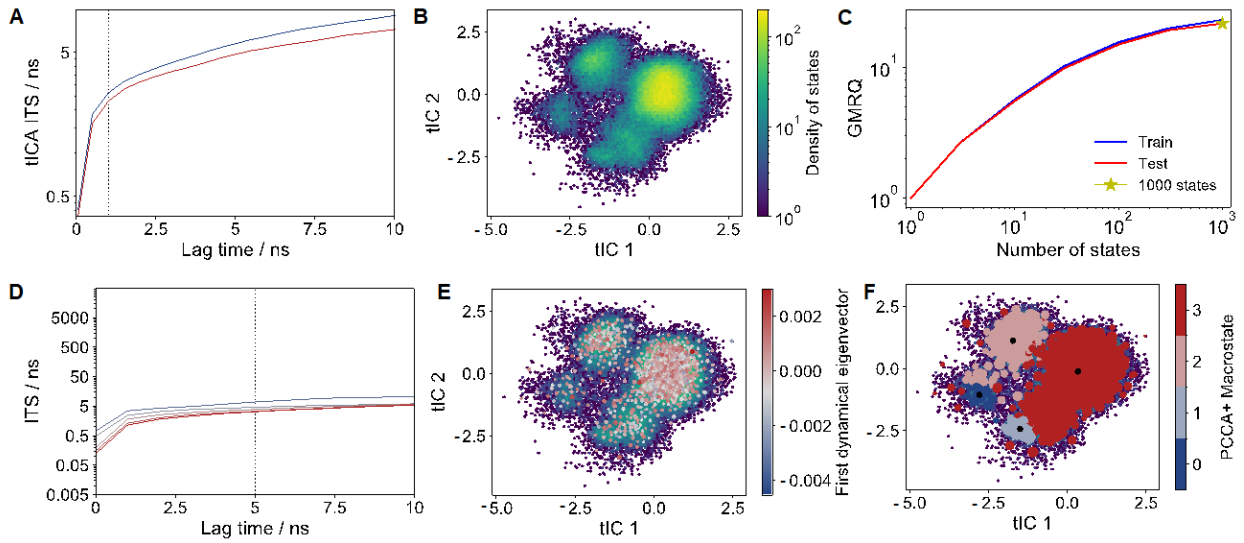

Figure 73. Time-structure independent component analysis (tICA) and Markov state modeling for **2A-*R*-OH-MM** macromonomer. **A.** Optimized tICA lag time, denoted by the vertical line, is 1 ns. **B.** 2-component tICA shows the density of states across the conformational landscape. **C.** Optimized number of microstates for MSM, denoted by the star, is 1000 states. **D.** Optimized MSM lag time, denoted by the vertical line, is 5 ns. **E.** Microstate MSM overlaid on the tICA plot shows different microstates in the MSM. The color bar denotes the first dynamical eigenvector of the microstates **F.** Macrostate MSM shows different microstates clustered into macrostates. The color bar denotes the PCCA+ clustered macrostates.

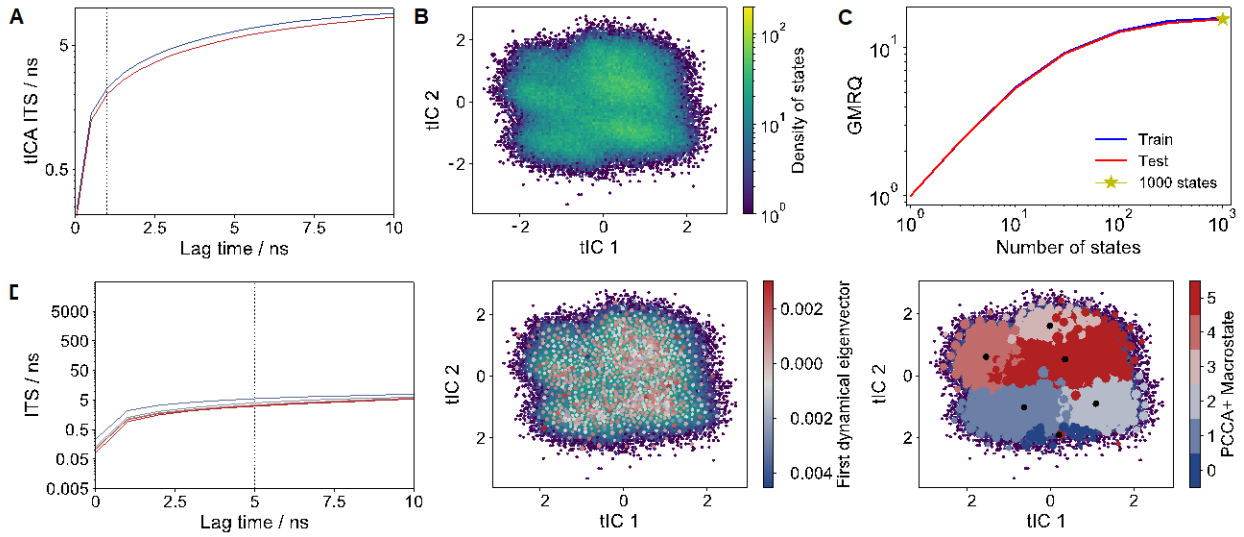

Figure 74. Time-structure independent component analysis (tICA) and Markov state modeling for **5A-*R*-OH-MM** macromonomer. **A.** Optimized tICA lag time, denoted by the vertical line, is 1 ns. **B.** 2-component tICA shows the density of states across the conformational landscape. **C.** Optimized number of microstates for MSM, denoted by the star, is 1000 states. **D.** Optimized MSM lag time, denoted by the vertical line, is 5 ns. **E.** Microstate MSM overlaid on the tICA plot shows different microstates in the MSM. The color bar denotes the first dynamical eigenvector of the microstates **F.** Macrostate MSM shows different microstates clustered into macrostates. The color bar denotes the PCCA+ clustered macrostates.

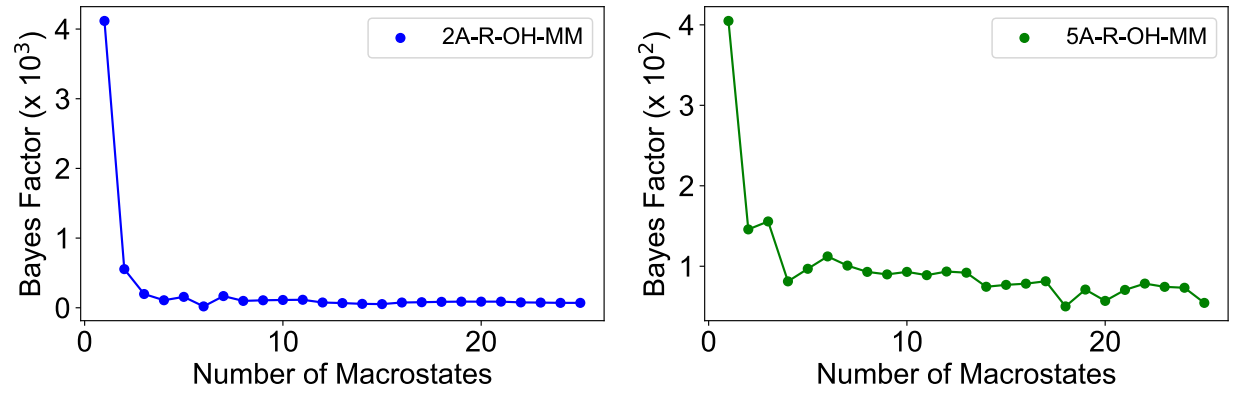

Figure 75. Bayes factor versus number of macrostates for **2A-*R*-OH-MM** and **5A-*R*-OH-MM**, obtained from using Bayesian agglomerative clustering engine (BACE) analysis.

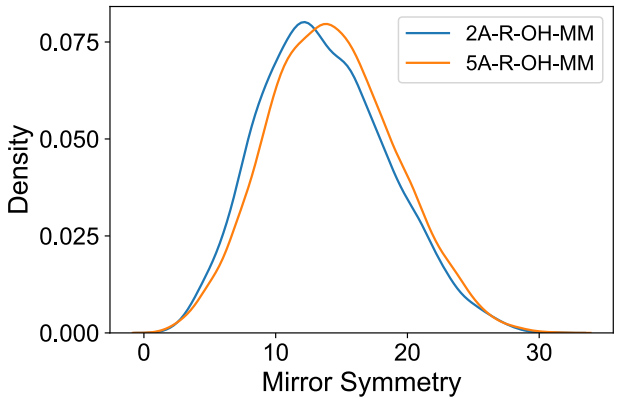

Figure 76. Distribution of mirror symmetry for **2A-*R*-OH-MM** and **5A-*R*-OH-MM**. The mean and standard deviation values for mirror symmetry measures are 13.68 ± 0.28, and 14.32 ± 0.36 for **2A-*R*-OH-MM** and **5A-*R*-OH-MM**, respectively. Statistical significance analysis for mirror symmetry measures for 2A-R-OH-MM and 5A-R-OH-MM using Welch's t-test resulted in p-value of 6.23E-21 and t-statistic of -9.40. The plot is generated by using every 10th frame in the concatenated trajectory of 120,000 frames, with 20,000 frames (1 μs) per replicate.

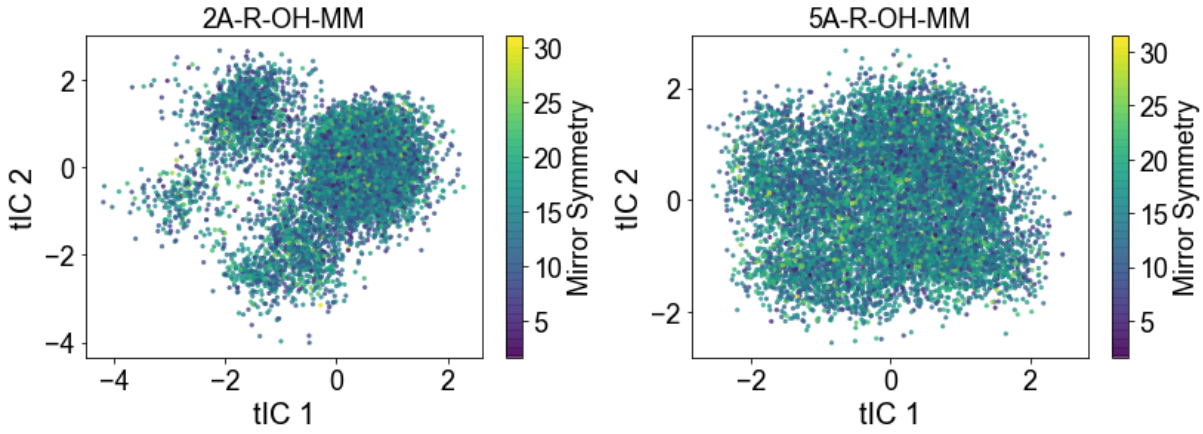

Figure 77. tIC coordinates colored by mirror symmetry values for **2A-*R*-OH-MM** and **5A-*R*-OH-MM**. The distribution is nearly uniform for both macromonomers.

Table 2. Stereoisomers for **2A-*R*-OH-MM** and **5A-*R*-OH-MM**.

2A-*R*-OH-MM isomers Baseline – $(SR)_4$	**5A-*R*-OH-MM** isomers Baseline - R_8
R_8	S_8
$(RS)_4$	$(RS)_4$
$(RRSS)_2$	$(RRSS)_2$
SRSRRSSR – Random1	SRSRRSSR – Random1
RRSRSSSR – Random2	RRSRSSSR – Random2

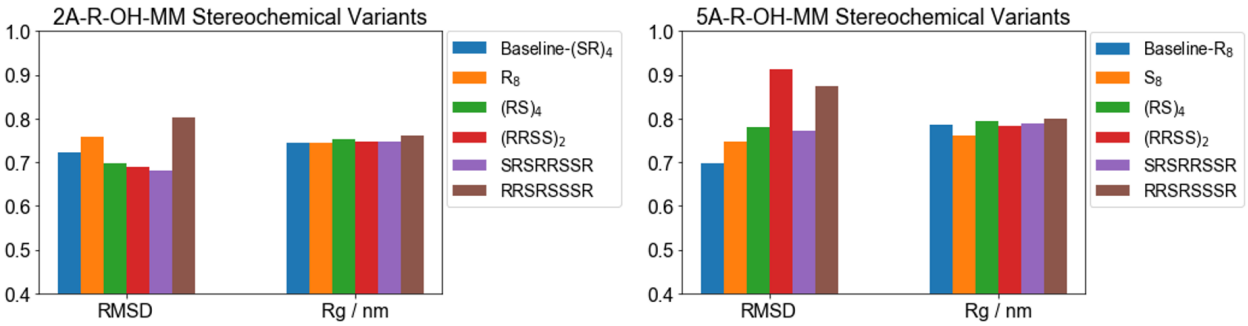

Figure 78. Comparison of mean values of RMSD and Rg for baseline, and stereoisomers of **2A-R-OH-MM** and **5A-R-OH-MM**. Experiments were performed once.

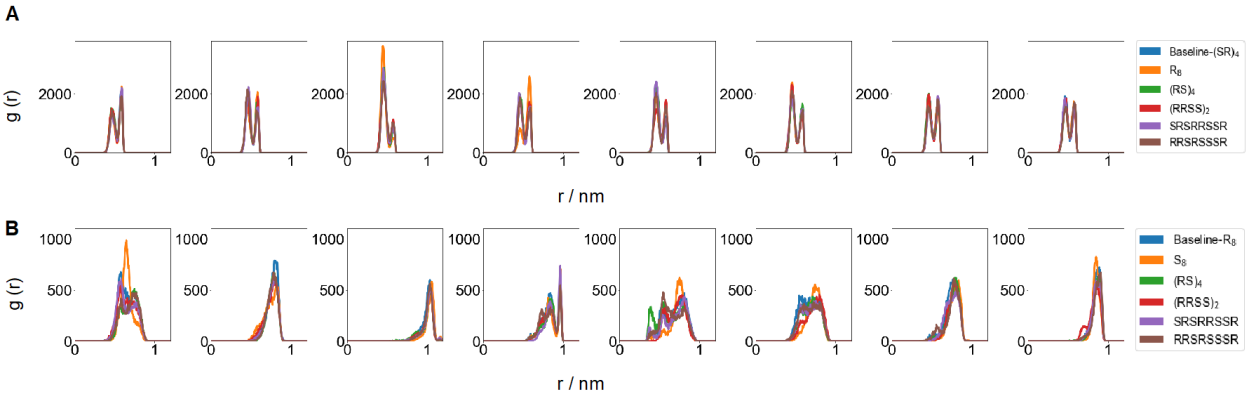

Figure 79. Radial Distribution Functions (RDFs) for consecutive triazole units of **A. 2A-R-OH-MM** and **B. 5A-R-OH-MM** stereoisomers.

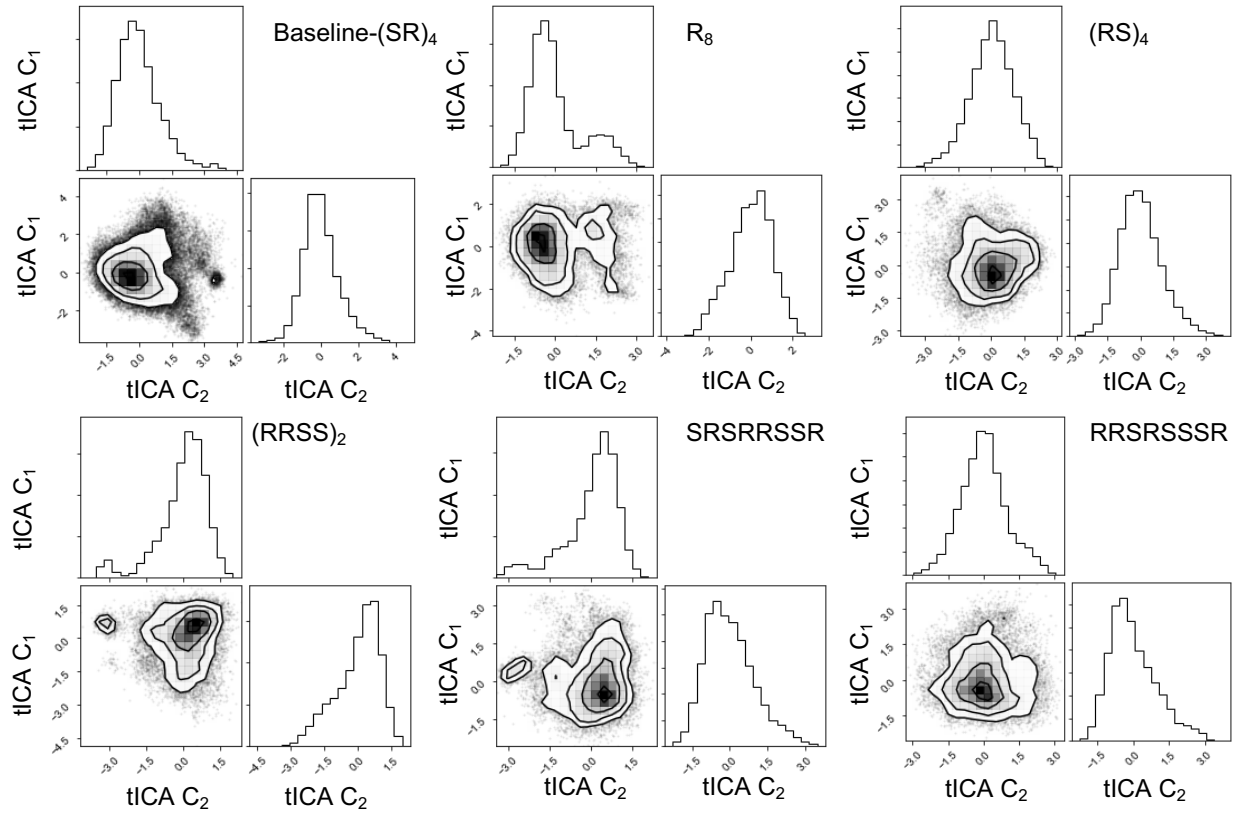

Figure 80. Two-dimensional Time-structure Independent Component Analysis for **2A-*R*-OH-MM** stereoisomers.

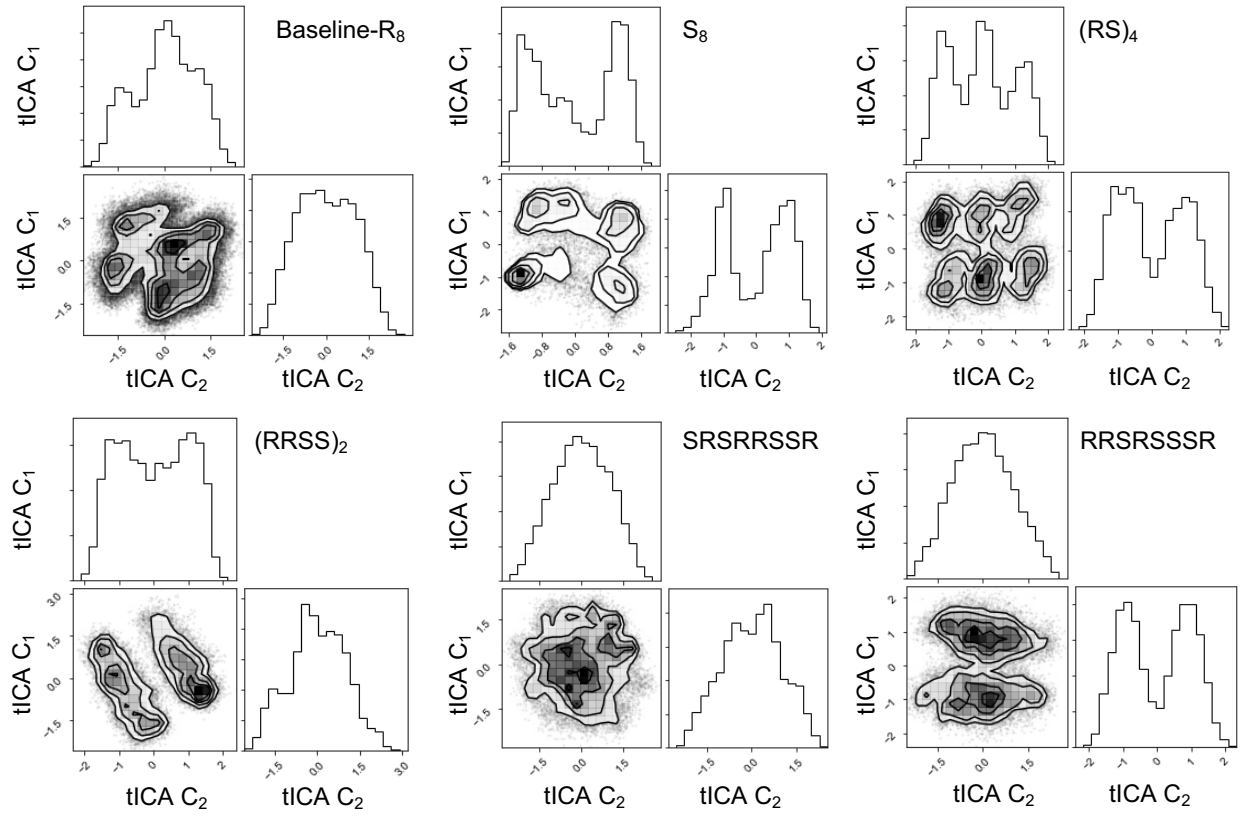

Figure 81. Two-dimensional Time-structure Independent Component Analysis for **5A-*R*-OH-MM** stereoisomers.

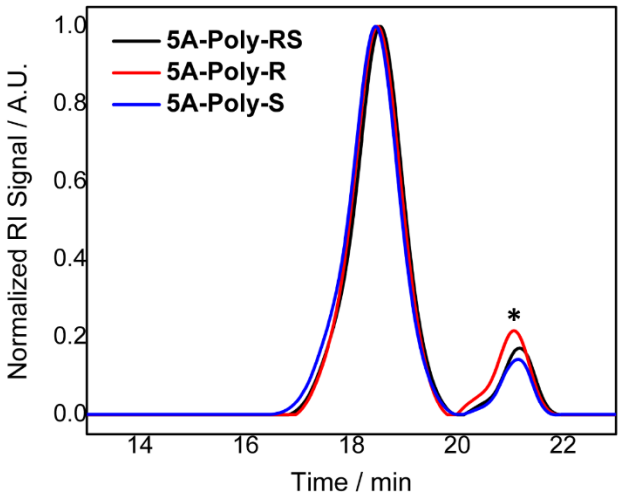

Figure 82. GPC traces for 5AIEG bottlebrush polymers. * denotes residual MM in the crude reaction mixture prior to deprotection and dialysis. In all cases, conversions of >90% was observed. GPC samples were run with two Shodex KD-806M column in series, due to COVID-related lack of access.

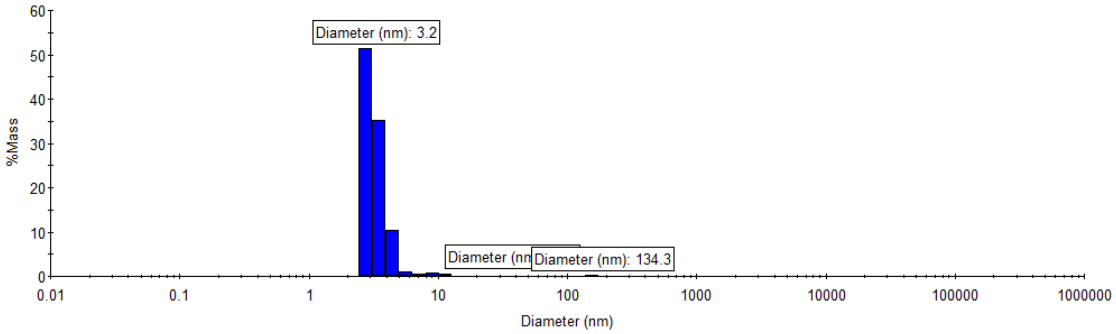

Figure 83. Dynamic light scattering (DLS) histogram for **5A-*RS*** with peaks at 3.2 ± 0.6 nm (98.2%), 10.4 ± 1.6 nm (1.5%), and 134.3 ± 28.2 nm (0.3%).

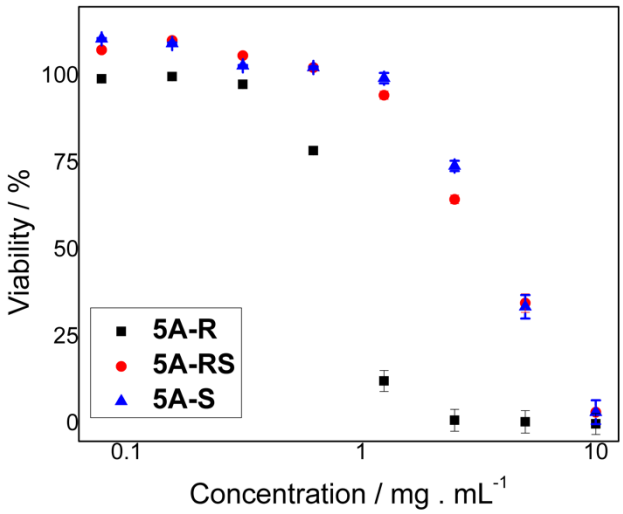

Figure 84. HUVEC cell viability (CellTiter-Glo assay) as a function of CBP concentration. Data are presented as mean ± SEM (n = 3 biologically independent samples).

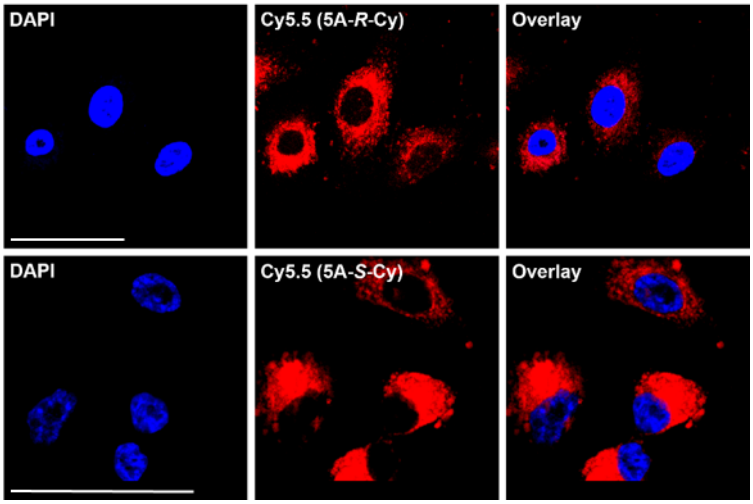

Figure 85. Confocal microscopy images of HUVEC cells (stained with DAPI) incubated with Cy5.5-labelled CBP **5A-*R*** (top) or **5A-*S*** (bottom) (n = 3 biologically independent samples). Scale bar = 50 μm.

Table 3. Red Blood Cell Hemolytic Activity of Chiral Bottlebrush Polymers (CBPs)

Concentration (mg/mL)	Hemolytic Activity (%)*	
	5A-*R*	**5A-*S***
10.00	3.7 ± 0.6	1.4 ± 0.2
5.00	0	0
2.50	0	0
1.25	0	0
0.63	0	0
0.31	0	0
0.16	0	0

*Limit of detection (LOD) of the assay was determined to be 0.063 mg/mL red blood cell, or 0.44% hemolytic activity.

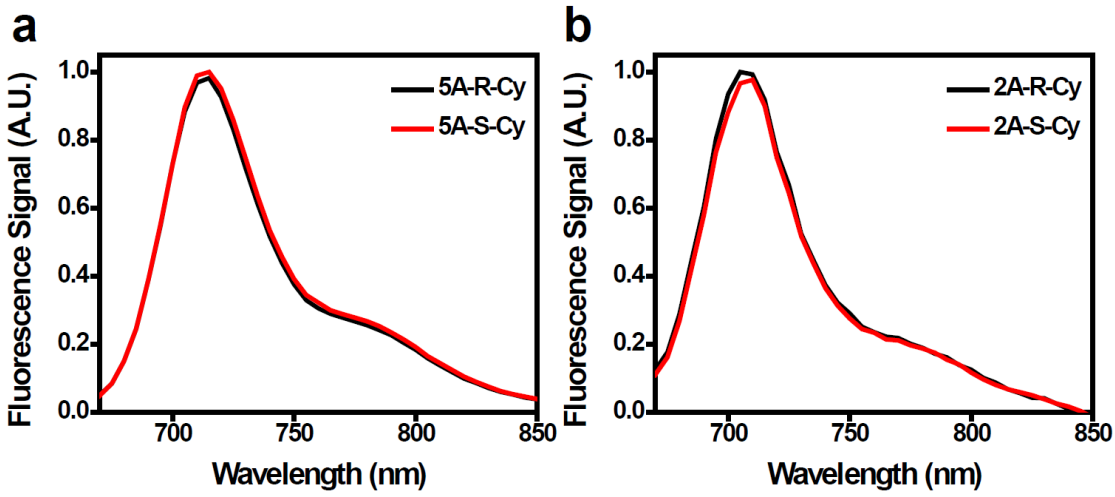

Figure 86. Emission spectra for **a. 5A-*R*-Cy** and **5A-*S*-Cy**; **b. 2A-*R*-Cy** and **2A-*S*-Cy**.

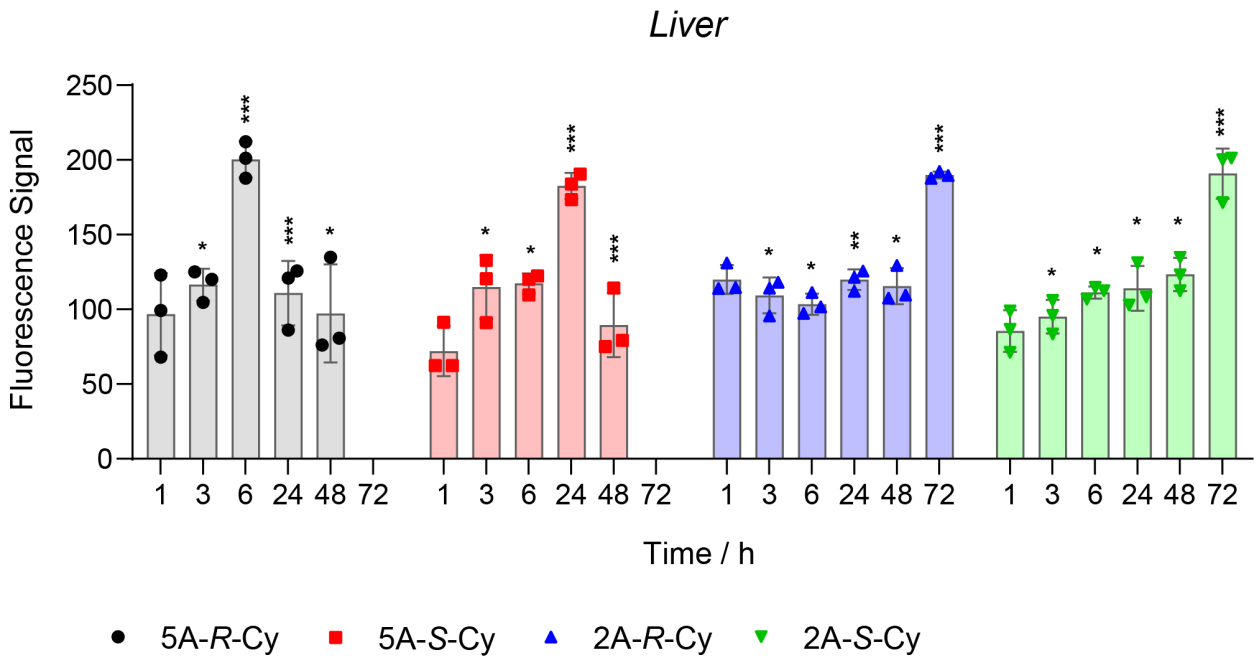

Figure 87. Quantification of *ex vivo* fluorescence signal from the liver of healthy balb/c mice (n = 3) injected with fluorescently labelled CBPs (Cy5.5, $\lambda_{ex}/\lambda_{em}$ = 640/700 nm). Peak liver accumulations were observed at 6 h and 24 h post-injection for **5A-*R*-Cy** and **5A-*S*-Cy**, respectively; in contrast, no differences were observed between **2A-*R*-Cy** and **2A-*S*-Cy**, both with highest accumulation at 72 h. Data are presented as mean ± SEM. Statistical comparisons were made using a two-tailed t test; comparisons were made between each time point and its previous time point. *not significant, **$p < 0.05$, ***$p < 0.01$, ****$p < 0.0001$. p values for **5A-*R*-Cy**: 0.3106 (3 h vs. 1 h), 0.0009 (6 h vs. 3 h), 0.0033 (24 h vs. 6 h), and 0.5796 (48 h vs. 24 h); **5A-*S*-Cy**: 0.0524 (3 h vs. 1 h), 0.8546 (6 h vs. 3 h), 0.0005 (24 h vs. 6 h), and 0.0022 (48 h vs. 24 h); **2A-*R*-Cy**: 0.3009 (3 h vs. 1 h), 0.5088 (6 h vs. 3 h), 0.0454 (24 h vs. 6 h), and 0.6194 (48 h vs. 24 h), 0.0005 (72 h vs. 48 h); **2A-*S*-Cy**: 0.4058 (3 h vs. 1 h), 0.0781 (6 h vs. 3 h), 0.7746 (24 h vs. 6 h), 0.4394 (48 h vs. 24 h), and 0.0044 (72 h vs. 48 h). Epi-fluorescence signal was reported in radiant efficiency ($\frac{p/sec/cm^2/sr}{\mu W/cm^2}$).

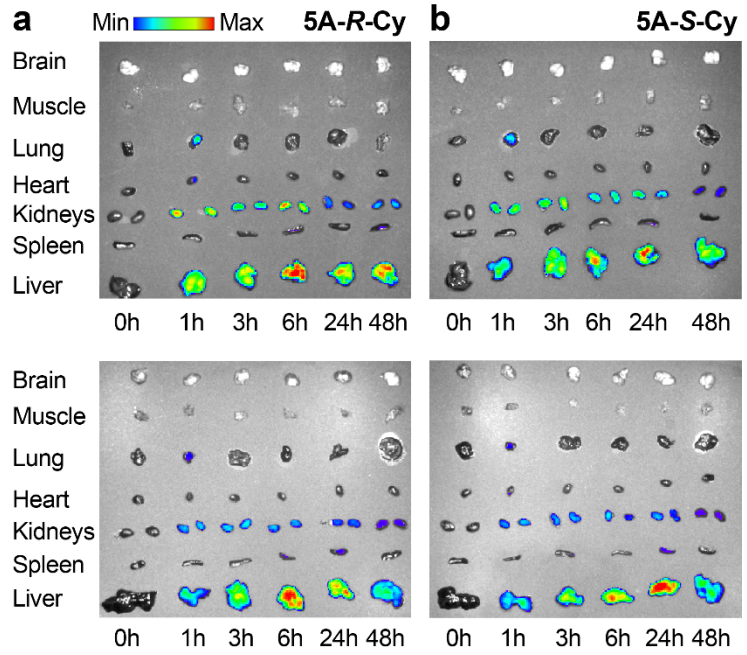

Figure 88. *Ex vivo* biodistribution of healthy balb/c mice (n = 3) injected with fluorescently labelled CBPs **5A-*R*-Cy** and **5A-*S*-Cy** (Cy5.5, $\lambda_{ex}/\lambda_{em}$ = 640/700 nm).

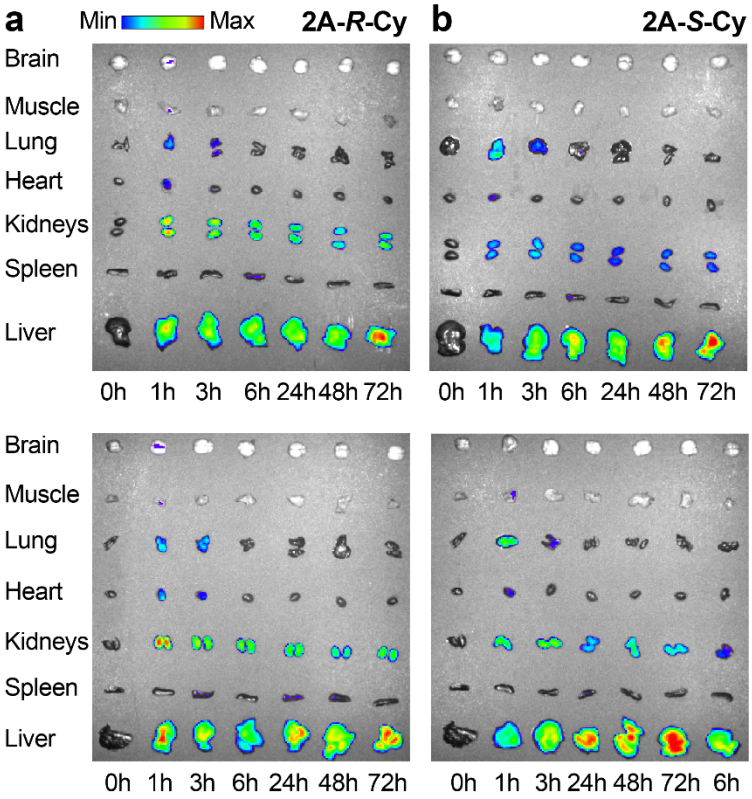

Figure 89. *Ex vivo* biodistribution of healthy balb/c mice (n = 3) injected with fluorescently labelled CBPs **2A-*R*-Cy** and **2A-*S*-Cy** (Cy5.5, $\lambda_{ex}/\lambda_{em}$ = 640/700 nm).

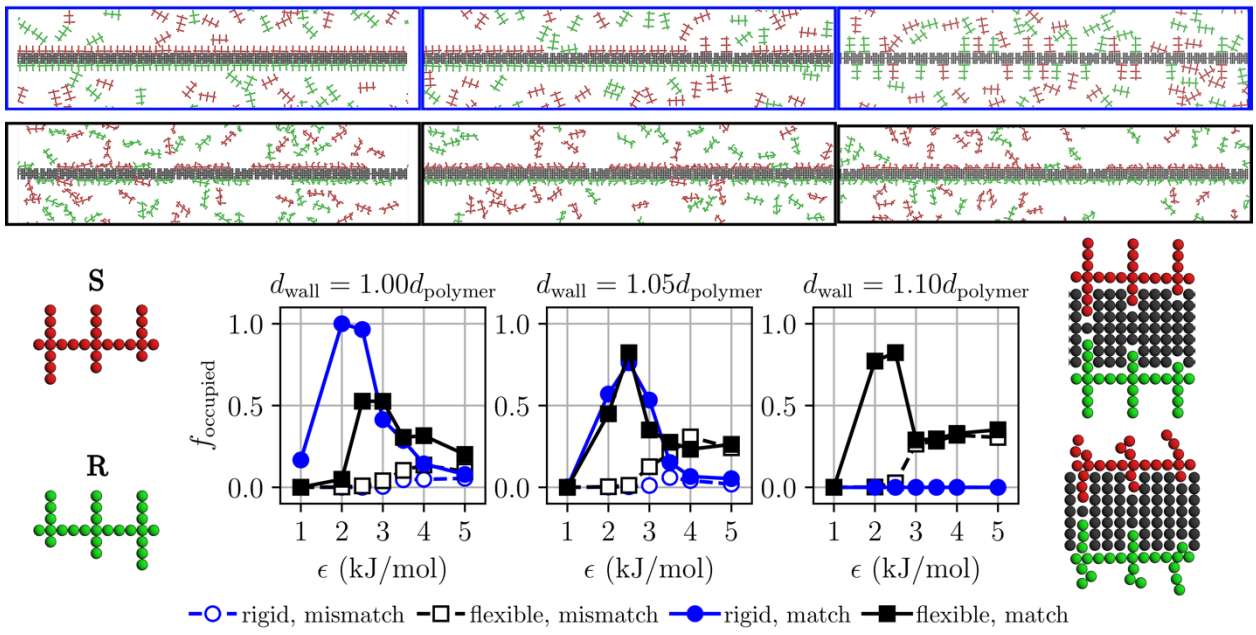

Figure 90. Fraction of wall binding sites occupied by matching and mismatching chiral bottlebrush polymers as a function of binding affinity (ϵ). The fraction of occupied binding sites is shown for polymers with rigid (blue) and flexible (black) sidechains and for the different wall geometries discussed in the text. Snapshots of the unit cell for the rigid and flexible polymers with ϵ = 2.5 (kJ/mol) are displayed above their corresponding plots of f_{occupied}. Enantiomeric polymers are shown in red and green. Enlarged snapshots of the rigid (top) and flexible (bottom) polymers bound to the wall surface are displayed to the right.

Section B. Materials / General Experimental Methods / Instrumentations

All reagents were purchased from commercial suppliers and used without further purification unless stated otherwise. 5-atom iterative exponential growth (5AIEG) octamer precursor **5A-*R*-OAc-8mer**[1] and **5A-*S*-OAc-8mer**[1] were prepared according to literature procedures using glycidal propargyl ether (**GPE**) monomers adapted from a more recent report.[2] Norbornene precursor **a1**,[3] tetraethylene glycol precursor **a2**,[4] and Grubbs 3rd generation bispyridyl catalyst **G3**[5] were prepared according to literature procedures with modifications specified in the following section.

Liquid chromatography mass spectrometry (LC/MS) was performed on an Agilent 1260 LC system equipped with a Zorbax SB-C18 rapid resolution HT column using a binary solvent system (acetonitrile and water with 0.1% acetic acid). Chiral HPLC was performed on an Agilent 1290 Infinity II system using a binary solvent system (hexanes and isopropanol). Data acquisition and analysis were performed with Chem Station. Recycling preparative HPLC was performed on a LaboACE system (Japan Analytical Industry) using a JAIGEL-2.5HR column. Size exclusion chromatography (SEC) analyses were performed on an Agilent 1260 Infinity setup with two Agilent PL1110-6500 columns in tandem and a 0.025 M LiBr DMF mobile phase run at 60 °C. The differential refractive index (dRI) of each compound was monitored using a Wyatt Optilab T-rEX detector. Data acquisition and analysis were performed with ASTRA6.1 and OriginPro 8, respectively. Column chromatography was carried out on silica gel 60F (EMD Millipore, 0.040–0.063 mm) or on aluminum oxide (Sigma-Aldrich, activated, neutral, Brockmann Activity I).

Nuclear magnetic resonance (NMR) spectra were recorded on Varian Inova-500 and Bruker AVANCE III-400 spectrometers, with working frequencies of 500 (^{1}H) and 125 (^{13}C) MHz, and 400 (^{1}H) and 100 (^{13}C) MHz, respectively. Chemical shifts are reported in ppm relative to the signals corresponding to the residual non-deuterated solvents: $CDCl_3$: δ_H = 7.26 ppm, MeOD: δ_H = 3.31 ppm and δ_C = 77.16 ppm; D_2O: δ_H = 4.79. Data acquisition and analysis were performed with Bruker TopSpin 4.0 and MestReNova v12.0.4, respectively. High-resolution mass spectra (HRMS) were measured on a Bruker Daltonics APEXIV 4.7 Tesla Fourier Transform Ion Cyclotron Resonance Mass Spectrometer (FT-ICR-MS) using an electrospray ionization (ESI) source. Matrix-assisted laser desorption/ionization-time of flight (MALDI-TOF) mass spectra were measured on a Bruker model MicroFlex instrument using α-cyano-4-hydroxycinnamic acid as the matrix. Data acquisition and analysis were performed with Bruker Daltonics. Dynamic light

scattering (DLS) measurements were performed using a Wyatt Technology Mobius DLS instrument. Bottlebrush polymer samples were prepared at 1 mg/mL in either nanopure water (MilliQ), PBS buffer, or 5% v/v glucose/nanopore water; disposable polystyrene cuvettes pre-cleaned with compressed air were used. Measurements were made in sets of 10 acquisitions, and the average hydrodynamic diameters were calculated using the DLS correlation function via a regularization fitting method (Dynamics 7.5.0.17 software package from Wyatt Technology). Circular dichroism (CD) measurements were performed on a Jasco J-1500 spectropolarimeter where the sensitivity, time constant, and scan rate were chosen appropriately. The temperature was kept constant at 293 K. Cells with an optical path length of 1 cm were used. Solutions were prepared in deionized water at a concentration of 5.87 μM concentration of the triazole. Data acquisition and analysis were performed with JASCO Spectra Manager and OriginPro 8, respectively.

In vitro cell viability: HUVEC cells were plated at 10^4 cells/well (in 100 μL media) in 96-well collagen-coated plates (Corning) and allowed for adhesion overnight, followed by the addition of one of the following bottlebrush polymers at various concentrations: **5A-*R***, **5A-*S***, **5A-*RS***, **2A-*R***, or **2A-*S***. The plates were incubated for 48h, and cell viability was then determined using CellTiter-Glo assay (Promega) via a Tecan Infinite ® 200 Pro plate reader. Data acquisition and analysis were performed with Tecan i-Control and GraphPad Prism 8, respectively. Viability assays with HeLa and MCF7 cells were performed in a similar manner, but without the use of collagen-coated plates.

In vitro cell uptake by flow cytometry: Stock solutions of **5A-*R*-Cy**, **5A-*S*-Cy**, **2A-*R*-Cy**, and **2A-*S*-Cy** were prepared in PBS (2 mg/mL). Cells were plated in 24-well plates and allowed for adhesion overnight in 450 μL media; HeLa and HUVEC cells were plated at 2.5×10^4 cells/well, whereas MCF7 cells were plated at 5.0×10^4 cells/well. Polymer solutions were then added (50 μL), resulting in the final polymer concentration of 0.2 mg/mL. Cells were then incubated for pre-determined intervals, and then harvested for analysis. Cell uptake was characterized by flow cytometry using a FACS LSR II HTS instrument (BD Biosciences). Data acquisition and analysis were performed with BD FACS Diva and GraphPad Prism 8, respectively. An example of the gating used is shown below.

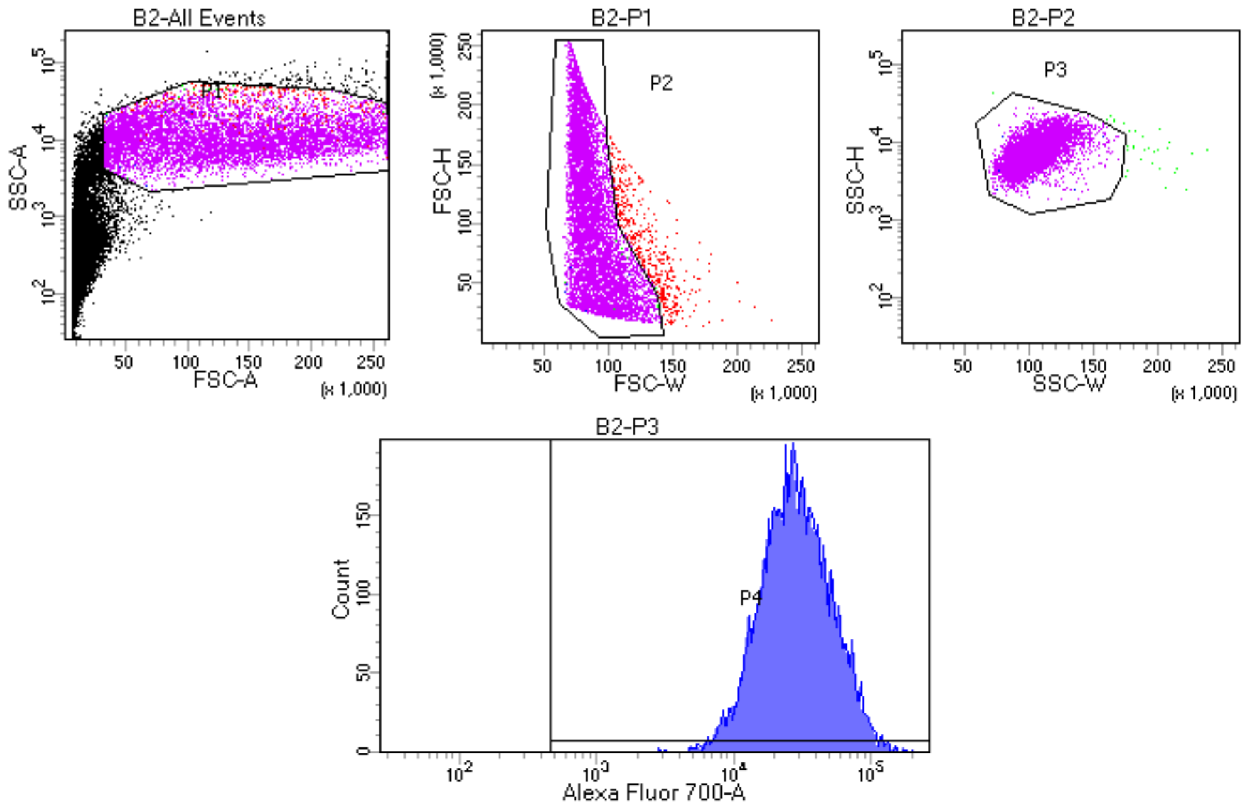

In vitro cell uptake by confocal microscopy: Stock solutions of **5A-*R*-Cy** and **5A-*S*-Cy** were prepared in PBS (2 mg/mL). Cells were plated at 1.0×10^5 cells/well in Nunc Lab-Tek Chambered Coverglass (Millipore-Sigma) plates and allowed for adhesion overnight in 180 µL media. Polymer solutions were then added (20 µL), resulting in the final polymer concentration of 0.2 mg/mL. Cells were then incubated for 24 h. Next, cells were stained with DAPI (Thermo Fisher) and subjected to confocal microscopy using a Nikon A1R confocal microscope. Data acquisition and analysis were performed with Olympus Fluoview 4.2a.

Hemolysis assay: the total hemoglobin concentration of human red blood cells stock (RBCs, Innovative Research) was measured using a Hemoglobin Colorimetric Detection Kit (Invitrogen). The RBC solution was then diluted to a hemoglobin concentration of 20 mg/ml with Ca^{2+}/Mg^{2+}-free DPBS. Diluted RBC solution (75 µl) was seeded in each well of a 96-well plate, followed by the addition of the following samples (75 µl): Triton-X100 (positive control), DPBS buffer (negative control), **5A-*R***, and **5A-*S*** at varying concentrations. The plate was then incubated at 37 ºC for 210 min with gentle mixing. Following the incubation, the plate was centrifuged at 800 × g

for 15 min. The supernatants were mixed in a 1:1 ratio with hemoglobin detection reagent and analyzed following manufacturer protocol.

Pharmacokinetic and biodistribution studies: In separate pharmacokinetic studies, **5A-*R*-Cy**, **5A-*S*-Cy**, **2A-*R*-Cy**, or **2A-*S*-Cy** doses (2.0 mg/200 μL) were injected into BALB/c mice (5 groups of *n=3*), and blood samples were taken at 1, 3, 6, 24, and 48h via cardiac puncture after euthanization in a CO_2 chamber, in addition to the control and 100% injected dose (ID). Samples were subjected to fluorescence imaging (IVIS, Cy5.5 $\lambda_{ex}/\lambda_{em}$ = 640/700 nm, Xenogen). For biodistribution studies, organs from these BALB/c mice were harvested and subjected to fluorescence imaging (IVIS, Cy5.5 $\lambda_{ex}/\lambda_{em}$ = 640/700 nm, Xenogen).

Imaging: *ex vivo* imaging was performed on an IVIS Spectrum-bioluminescent and fluorescent imaging system (Xenogen) at the Koch Institute for Integrative Cancer Research at MIT. Epi-fluorescence imaging was acquired through excitation of the Cy5.5 fluorophore ($\lambda_{ex}/\lambda_{em}$ = 640/700 nm, exposure time 2-10s). Data acquisition and analysis were performed with Living Image 4.5 and GraphPad Prism 8, respectively

Statistical Significance: statistical significance were accessed using GraphPad Prism 8.

Section C. Synthetic Protocols

1) Norbornene Endgroup

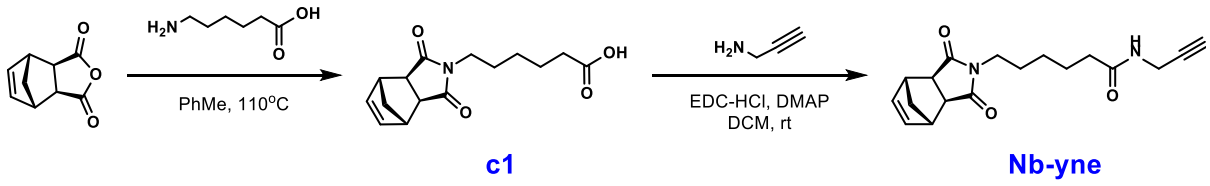

Scheme 1. Synthesis of the Norbornene Endgroup (**Nb-yne**).

c1: a literature procedure[3] was followed with slight modifications. Briefly, *cis*-5-norbornene-*exo*-2,3-dicarboxylic anhydride (500 mg, 3.0 mmol, 1.0 eq) and 6-aminohexanoic acid (479 mg, 3.7 mmol, 1.2 eq) were added to a round bottom flask (RBF) fitted with a condenser. Toluene (15 mL) was then added, and the solution was stirred overnight at 110°C. The mixture was then allowed to cool to room temperature, and concentrated under vacuum. DCM (150 mL) was then added, and the solution was washed with 1M HCl (3 × 150 mL) and brine (1 × 150 mL). The organic layer was collected, dried over Na_2SO_4, and concentrated under vacuum, affording the product as a white solid (834 mg, 96% yield). Characterization data agreed with the reported results.[3]

Nb-yne: into a RBF, **c1** (270 mg, 1.0 mmol, 1.5 eq), propargylamine (36 mg, 42 µL, 1.0 eq), *N*-(3-dimethylaminopropyl)-*N'*-ethylcarbodiimide hydrochloride (EDC.HCl) (187 mg, 1.0 mmol, 1.5 eq), and 4-dimethylaminopyridine (DMAP) (40 mg, 0.3 mmol, 0.5 eq), and DCM (35 mL) were added. The reaction mixture was stirred overnight and then concentrated under vacuum. Column chromatography (3% MeOH/DCM) of the crude mixture yielded product as a white solid (191 mg, 94% yield). HRMS-ESI: Calcd for $C_{18}H_{22}N_2O_3$: *m/z* = 315.1703 $[M + H]^+$; Found: 315.1692 $[M+H]^+$. ^{1}H NMR (400 MHz, $CDCl_3$, ppm) δ_H 6.28 (s, 2H), 5.70 (b, 1H), 4.04 (m, 2H), 3.45 (t, J = 7.2 Hz, 2H), 3.26 (s, 2H), 2.67 (s, 2H), 2.22 (t, J = 2.4 Hz, 1H), 2.18 (t, J = 7.6 Hz, 2H), 1.72 – 1.62 (m, *2*H), 1.61 – 1.48 (m, 3H), 1.38 – 1.27 (m, 2H), 1.23 – 1.17 (d, 1H). ^{13}C NMR (100 MHz, $CDCl_3$, ppm): δ_C 178.2, 172.3, 137.9, 79.8, 71.7, 47.9, 45.3, 42.9, 38.5, 36.2, 29.3, 27.5, 26.5, 25.0

2) 2-Atom IEG (2AIEG) Precursors

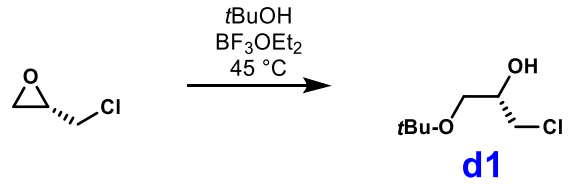

Scheme 2. Synthesis of **d1**.

d1: (*S*)-Epichlorohydrin (100 g, 1.08 mol) was added dropwise to a solution of *t*-BuOH (300 g, 4.04 mol) and BF_3OEt_2 (4.26 g, 30 mmol, 3.77 mL). The reaction solution was stirred at room temperature for 1 hour after which the reaction was heated to 45 °C and left to react overnight. 100 mL of water was then added to the solution and most of the *t*-BuOH was removed via reduced pressure. 400 mL of EtOAc was added to the reaction mixture and the solution was washed 2x with 400 mL of water and 1x with 200 mL of brine. The organic layer was isolated, dried over Na_2SO_4, and concentrated under vacuum, affording the product as a clear liquid (140 g, 843 mmol, 78% yield). HRMS-ESI: Calcd for $C_7H_{16}ClO_2$: *m/z* = 167.0761 $[M + H]^+$; Found: 167.0849 $[M+H]^+$. ^{1}H NMR (500 MHz, $CDCl_3$, ppm) δ_H 3.91 (sext, J = 5.5 Hz, 1H), 3.64 (dd, J = 5.5 Hz, 4.5 Hz, 1H), 3.58 (dd, J = 5.0 Hz, 4.5 Hz, 1H), 3.46 (d, J = 5.0 Hz, 2H), 2.56 (d, J = 5.0 Hz, 1H), 1.20 (s, 9H). ^{13}C NMR (125 MHz, $CDCl_3$, ppm): δ_C 73.5, 70.6, 62.3, 45.9, 27.4. The enantiomer of **d1** was also prepared in a similar fashion and afforded similar yield.

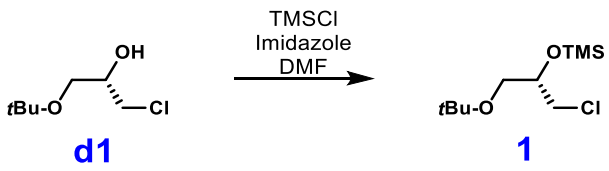

Scheme 3. Synthesis of **1** from **d1**.

1: Imidazole (111 g, 1.63 mol) and DMF (400 mL) were added to **d1** (138 g, 831 mmol) and the solution was stirred until the imidazole was dissolved. TMSCl (177.4 g, 1.63 mol) was added gradually to the solution and the reaction was left to react overnight at room temperature. Upon completion, excess TMSCl and DMF were removed through reduced pressure. Throughout

evaporation, the temperature was not allowed to exceed 60 °C to prevent degradation of the product. 300 mL of diethyl ether was then added to the mixture and stirred for half an hour. The organic solution was then extracted 3x with 200 mL H_2O, isolated, dried over Na_2SO_4, and concentrated under vacuum affording the product **1** as a clear liquid (169 g, 710 mmol, 85% yield). HRMS-ESI: Calcd for $C_{10}H_{24}ClO_2Si$: *m/z* = 239.1156 [*M* + H]$^+$; Found: 239.1247 [*M* +H]$^+$. ^{1}H NMR (500 MHz, $CDCl_3$, ppm) δ_H 3.91 (p, *J* = 5.7 Hz, 1H), 3.63 (dd, *J* = 5.5 Hz, 2.1 Hz, 1H), 3.49 (dd, *J* = 12.6 Hz, 1.8 Hz, 1H), 3.38 (dd, *J* = 3.7 Hz, 1.1 Hz, 1H), 3.33 (dd, *J* = 3.2 Hz, 0.9 Hz, 1H), 1.18 (s, 9H), 0.16 (s, 9H). ^{13}C NMR (125 MHz, $CDCl_3$, ppm): δ_C 72.2, 63.7, 47.1, 27.5, 0.3. The enantiomer of **1** was also prepared in a similar fashion and afforded similar yield.

1 2

Scheme 4. Synthesis of **2** from **1**.

2: Trimethylsilylacetylene (113 g, 1.15 mol) was added to anhydrous THF (460 mL), and the solution was cooled to -78 °C. A 2.5M solution of *n*-BuLi (460 mL) was added dropwise to the solution. The solution was allowed to warm to room temperature and kept inside a room temperature water bath. DMSO (300 mL) and then **1** (130 g, 546 mmol) were added to the reaction mixture and the reaction was left stirring for 4 hours. Completion of the reaction was checked through crude ^{1}H NMR. MeOH (30 mL) was then added very slowly dropwise to the solution to quench the reaction and remove all silyl protecting groups. Caution should be used as large quantities of gas will be released. 30 minutes after complete addition of MeOH, the majority of THF and other volatiles were removed under reduced pressure. 600 mL of diethyl ether was then added to the solution, which was then extracted 1x with 600 mL of H_2O and 2x with 300 mL of 5% LiCl solution. The organic layer was isolated, dried over Na_2SO_4, and concentrated under vacuum, affording the product **2** as a slightly yellow liquid (54 g, 346 mmol, 63% yield) which was used without further purification. HRMS-ESI: Calcd for $C_9H_{17}O_2$: *m/z* = 157.1150 [*M* + H]$^+$; Found: 157.1242 [*M* +H]$^+$. ^{1}H NMR (500 MHz, $CDCl_3$, ppm) δ_H 3.86 (sext, *J* = 4.3 Hz, 1H), 3.49

(dd, J = 9.0 Hz, 3.9 Hz, 1H), 3.36 (dd, J = 9.0 Hz, 6.5 Hz, 1H), 2.53 (d, J = 4.9 Hz, 1H), 2.45 (t, J = 2.4 Hz, 1H), 2.43 (t, J = 2.7 Hz, 1H), 2.02 (t, J = 2.8 Hz, 1H), 1.20 (s, 9H). ^{13}C NMR (125 MHz, $CDCl_3$, ppm): δ_C 80.6, 73.3, 70.3, 69.1, 64.30, 27.5, 23.4. The enantiomer of **2** was also prepared in a similar fashion and afforded similar yield.

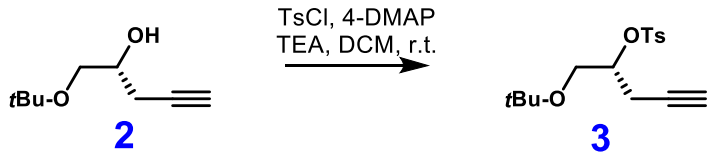

Scheme 5. Synthesis of **3** from **2**.

3: 4-DMAP (16.6 g, 136 mmol), triethylamine (51.5 g, 510 mmol), and DCM (600 mL) were added to **2** (53 g, 340 mmol). Tosyl chloride (71.3 g, 374 mmol) was then added portionwise into the solution and the reaction was left stirring overnight at room temperature. After completion of the reaction, DCM was removed under reduced pressure and 300 mL of EtOAc was added to the mixture. This organic solution was then extracted 1x with 300 mL of H_2O and 2x with 300 mL of pH=2 HCl solution. The organic layer was isolated, dried over Na_2SO_4, and concentrated under vacuum, affording the product **3** as a slightly yellow liquid (100 g, 322 mmol, 95% yield) which was used without further purification. HRMS-ESI: Calcd for $C_{16}H_{23}O_4S$: m/z = 311.1239 [M + H]$^+$; Found: 311.2041 [M +H]$^+$. ^{1}H NMR (500 MHz, $CDCl_3$, ppm) δ_H 7.81 (d, J = 8.4 Hz, 2H), 7.31 (d, J = 8.2 Hz, 2H), 4.54 (m, 1H), 3.50 (d, J = 5.3 Hz, 2H), 2.61 (dq, J = 17.1 Hz, 2.7 Hz, 1H), 2.56 (dq, J = 16.5 Hz, 3.1 Hz, 1H), 2.42 (s, 3H), 1.90 (t, J = 2.7 Hz, 1H), 1.08 (s, 9H). ^{13}C NMR (125 MHz, $CDCl_3$, ppm): δ_C 144.8, 133.9, 129.7, 128.2, 79.1, 78.5, 73.6, 71.0, 61.7, 27.3, 21.8, 21.7. The enantiomer of **3** was also prepared in a similar fashion and afforded similar yield.

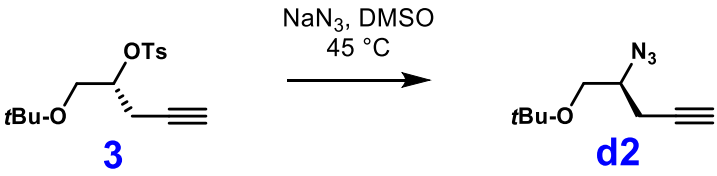

Scheme 6. Synthesis of **d2** from **3**.

d2: NaN_3 (41.3 g, 636 mmol) and DMSO (500 mL) were added to **3** (66 g, 212 mmol) and the reaction was heated to 45 °C and left to react overnight. After completion of the reaction, 800 mL of EtOAc was added to the solution and this organic solution was extracted 1x with 800 mL of H_2O and 2x with 400 mL of 2% LiCl solution. The organic layer was isolated, dried over Na_2SO_4, and concentrated under vacuum. The crude product **d2** (31 g, 171 mmol, 81% yield) was used without further purification. HRMS-ESI: Calcd for $C_9H_{16}NO$: *m/z* = 154.1231 $[M - N_2 + H]^+$; Found: 154.1240 $[M - N_2 + H]^+$. ^1H NMR (500 MHz, $CDCl_3$, ppm) δ_H 3.49 (m, 2H), 3.37 (m, 1H), 2.38 (ddd, 1H), 2.38 (ddd, 1H), 1.94 (t, J = 2.8 Hz, 1H), 1.19 (s, 9H). ^{13}C NMR (125 MHz, $CDCl_3$, ppm): 79.7, 78.9, 77.3, 73.4, 70.7, 63.3, 59.7. The enantiomer of **d2** was also prepared in a similar fashion and afforded similar yield.

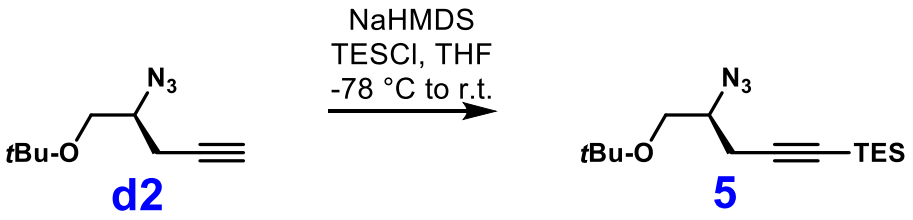

Scheme 7. Synthesis of **5** from **d2**.

5: Anhydrous THF (550 mL) was added to **d2** (30 g, 166 mmol) and the solution was cooled to -78 °C. 1M solution of NaHMDS in THF (199 mmol, 199 mL) was added dropwise to the reaction solution. The reaction was left to stir for 30 minutes and then TESCl (37.4 g, 45.0 mL, 248 mmol) was added dropwise. The solution was allowed to warm to room temperature and left to react for 4 hours. Acetic acid (30 mL) was added to the solution to quench the reaction and THF was removed under reduced pressure. 100 mL of EtOAc was added to the solution and extracted 1x with 100 mL H_2O. The organic layer was isolated, dried over Na_2SO_4, and concentrated under vacuum. The crude product was then purified with column chromatography (Hexanes/EtOAc) to afford the final product **5** as a clear liquid (42.2 g, 143 mmol, 86% yield). HRMS-ESI: Calcd for $C_{15}H_{31}NOSi$: *m/z* = 269.2175 $[M - N_2 + H]^+$; Found: 269.1864 $[M - N_2 + H]^+$. ^1H NMR (500 MHz, $CDCl_3$, ppm) δ_H 3.60-3.47 (overlap, 3H), 2.51 (dd, 1H), 2.48 (dd, 1H), 1.19 (s, 9H), 0.86 (t, 9H), 0.55 (q, 6H). ^{13}C NMR (125 MHz, $CDCl_3$, ppm): δ_C 103.3, 85.0, 73.7, 63.5, 60.3, 27.5, 22.8, 7.5, 4.5. The enantiomer of **5** was also prepared in a similar fashion and and afforded similar yield.

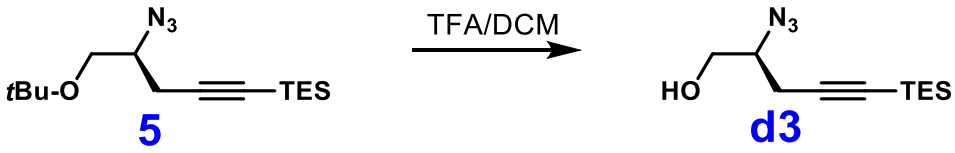

Scheme 8. Synthesis of **d3** from **5**.

d3: A 1:1 solution of TFA and DCM (140 mL) were added to **5** (40 g, 135 mmol) and the solution was allowed to stir for 90 minutes. Progress of the reaction was tracked through TLC. Upon completion, TFA and DCM were removed through reduced pressure and the crude product was dissolved in 100 mL EtOAc and extracted 1x with 100 mL of H_2O and 1x with 100 mL of pH=1 HCl solution. The organic layer was isolated, dried over Na_2SO_4, and concentrated under vacuum. The crude product was then purified with column chromatography (Hexanes/EtOAc) to afford the final product **d3** as a clear liquid (14 g, 58 mmol, 43% yield). HRMS-ESI: Calcd for $C_{11}H_{22}N_3OSi$: m/z = 240.1454 $[M + H]^+$; Found: 240.1573 $[M + H]^+$. ^{1}H NMR (500 MHz, $CDCl_3$, ppm) δ_H 3.73 (m, 1H), 3.60 (overlap, 2H), 2.52 (d, J = 2.9 Hz, 2H), 0.81 (t, 9H), 0.53 (q, 6H). ^{13}C NMR (125 MHz, $CDCl_3$, ppm): δ_C 102.5, 85.6, 85.6, 64.2, 62.3, 22.6, 7.5, 4.4. The enantiomer of **d3** was also prepared in a similar fashion and afforded similar yield.

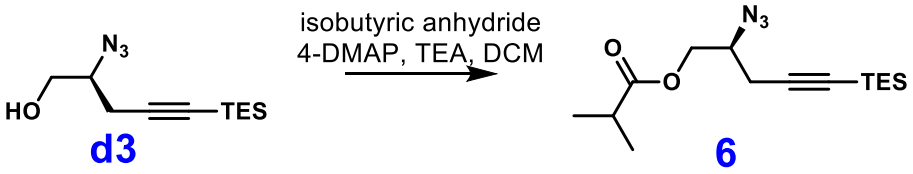

Scheme 9. Synthesis of **6** from **d3**.

6: 4-DMAP (1.3 g, 10.6 mmol), triethylamine (4 g, 5.5 mL, 40 mmol), and DCM (100 mL) were added to **d3** (6.3 g, 26.5 mmol). Isobutyric anhydride (7.19 g, 31.8 mmol) was then added dropwise into the solution and the reaction was left stirring for 2 hours. After completion of the reaction, DCM was removed under reduced pressure and 100 mL of EtOAc was added to the mixture. The organic solution was extracted 1x with 100 mL of H_2O and 2x with 100 mL of pH=1 HCl solution.

The organic layer was isolated, dried over Na_2SO_4, and concentrated under vacuum. The crude product was purified by column chromatography (Hexanes/EtOAc) to afford the final product **6** as a clear liquid (5.6 g, 18.3 mmol, 69% yield). HRMS-ESI: Calcd for $C_{15}H_{28}N_3O_2Si$: *m/z* = 310.1873 $[M + H]^+$; Found: 310.2018 $[M + H]^+$. ^1H NMR (500 MHz, $CDCl_3$, ppm) δ_H 4.28 (dd, *J* = 10.7 Hz, 3.3 Hz, 1H), 4.14 (dd, *J* = 11.2 Hz, 5.9 Hz, 1H), 3.75 (pent, *J* = 5.4 Hz, 1H), 2.60 (sept, *J* = 5.8 Hz, 1H), 2.53 (d, *J* = 5.6 Hz, 2H), 1.19 (d, *J* = 5.9 Hz, 6H), 0.97 (t, *J* = 6.6 Hz, 9H), 5.58 (q, *J* = 6.5 Hz, 6H). ^{13}C NMR (125 MHz, $CDCl_3$, ppm): δ_C 176.6, 101.8, 86.0, 65.2, 59.2, 34.0, 22.9, 19.0, 19.0, 7.5, 4.4. The enantiomer of **6** was also prepared in a similar fashion and afforded similar yield.

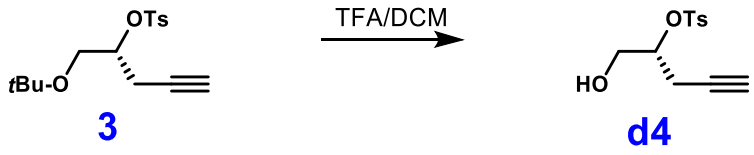

3 d4

Scheme 10. Synthesis of **d4** from **3**.

d4: A 1:1 solution of TFA and DCM (110 mL) were added to **3** (33 g, 110 mmol) and the solution was allowed to stir for 90 minutes. Progress of the reaction was tracked through TLC. Upon completion, TFA and DCM were removed through reduced pressure and the crude product was dissolved in 100 mL EtOAc and extracted 1x with 100 mL of H_2O and 1x with 100 mL of pH=1 HCl solution. The organic layer was isolated, dried over Na_2SO_4, and concentrated under vacuum. The crude product was then purified with column chromatography (Hexanes/EtOAc) to afford the final product **d4** as a clear liquid (18.6 g, 73 mmol, 67% yield). HRMS-ESI: Calcd for $C_{12}H_{15}O_4S$: *m/z* = 255.0613 $[M + H]^+$; Found: 255.0691 $[M + H]^+$. ^1H NMR (500 MHz, $CDCl_3$, ppm) δ_H 7.83 (d, *J* = 8.4 Hz, 2H), 7.36 (d, *J* = 8.3 Hz, 2H), 4.64 (m, 1H), 3.91 (dd, *J* = 12.6 Hz, 3.3 Hz, 1H), 3.84 (dd, *J* = 12.7 Hz, 5.4 Hz, 1H), 2.59 (dq, *J* = 5.7 Hz, 2.9 Hz, 1H), 2.55 (dq, *J* = 10.2 Hz, 2.7 Hz, 1H), 2.46 (s, 3H), 1.97 (t, *J* = 2.9 Hz, 1H). ^{13}C NMR (125 MHz, $CDCl_3$, ppm): δ_C 145.1, 133.2, 129.8, 127.8, 80.2, 78.0, 71.4, 62.6, 21.5, 21.0. The enantiomer of **d4** was also prepared in a similar fashion and afforded similar yield.

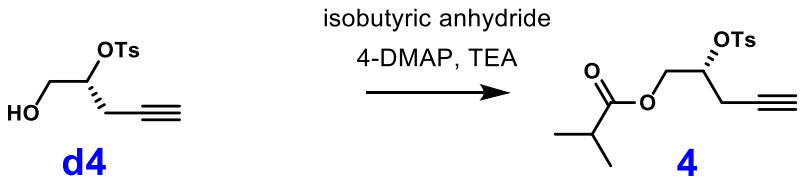

Scheme 11. Synthesis of **4** from **d4**.

4: 4-DMAP (3.05 g, 25 mmol), triethylamine (7.6 g, 10.4 mL, 75 mmol), and DCM (100 mL) were added to **d4** (14.7 g, 56.5 mmol). Isobutyric anhydride (9.8 g, 62.2 mmol) was then added dropwise into the solution and the reaction was left stirring for 2 hours. After completion of the reaction, DCM was removed under reduced pressure and 100 mL of EtOAc was added to the mixture. The organic solution was extracted 1x with 100 mL of H_2O and 2x with 100 mL of pH=1 HCl solution. The organic layer was isolated, dried over Na_2SO_4, and concentrated under vacuum to afford the final product **4** as a clear liquid (16.3 g, 50 mmol, 89% yield). HRMS-ESI: Calcd for $C_{16}H_{21}O_5S$: *m/z* = 325.1031 $[M + H]^+$; Found: 325.1193 $[M + H]^+$. ^{1}H NMR (500 MHz, $CDCl_3$, ppm) δ_H 7.78 (d, *J* = 7.0 Hz, 2H), 7.32 (d, *J* = 6.8 Hz, 2H), 4.73 (m, 1H), 4.26 (dd, *J* = 10.2 Hz, 2.9 Hz, 1H), 4.16 (dd, *J* = 10.3 Hz, 5.3 Hz, 1H), 2.57 (dd, *J* = 5.3 Hz, 2.3 Hz, 2H), 2.42 (s, 3H), 2.40 (pent, *J* = 5.9 Hz, 1H), 1.98 (t, *J* = 2.3 Hz, 1H), 1.08 (d, *J* = 5.9 Hz, 3H), 1.07 (d, *J* = 5.8 Hz, 3H). ^{13}C NMR (125 MHz, $CDCl_3$, ppm): δ_C 176.4, 145.1, 133.7, 129.9, 128.0, 127.9, 77.3, 76.8, 71.9, 63.5, 33.8, 21.9, 21.7, 18.9, 18.8. The enantiomer of **4** was also prepared in a similar fashion and afforded similar yield.

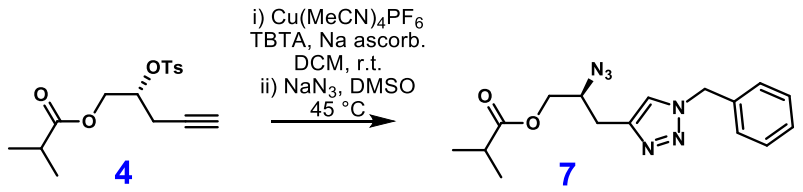

Scheme 12. Synthesis of **7** from **4**.

7: DCM (1.2 mL), benzyl azide (24.7 mg, 0.186 mmol) tris(benzyltriazolylmethyl)amine (TBTA) (6.4 mg, 0.012 mmol), $Cu(MeCN)_4PF_6$ (2.3 mg, 0.062 mmol), and sodium ascorbate (2.3 mg, 0.012 mmol) were added to **4** (20 mg, 0.062 mmol) in an oven-dried 20 mL scintillation vial. The reaction

was left at room temperature and stirred overnight. Progress of the reaction was tracked through TLC. At completion, EtOAc (10 mL) was added to the mixture which was extracted 3 times with 10 mL of water. The organic layer was isolated, dried over Na_2SO_4, and concentrated under reduced pressure. NaN_3 (8.1 mg, 0.12 mmol) and DMSO (240 µL) were added to the crude product and the mixture was heated to 45 °C and left to react overnight. EtOAc (10 mL) was added to the mixture which was extracted 3 times with 10 mL of 1% LiCl solution. The organic layer was isolated, dried over Na_2SO_4, and concentrated under reduced pressure. The crude product was loaded onto a silica column and purified with column chromatography (hexanes to DCM to 1% MeOH in DCM) to yield **7** (14 mg, 0.043 mmol, 69% yield). HRMS-ESI: Calcd for $C_{16}H_{21}N_6O_2$: m/z = 329.1648 $[M + H]^+$; Found: 329.1596 $[M + H]^+$. ^{1}H NMR (500 MHz, $CDCl_3$, ppm) δ_H 7.37 (overlap, 3H), 7.34 (s, 1H), 7.26 (overlap with $CDCl_3$, 2H), 5.52 (s, 2H), 4.26 (dd, J = 9.5 Hz, 2.5 Hz, 1H), 4.11 (dd, J = 9.5 Hz, 5.5 Hz, 1H), 4.01 (m, 1H), 2.95 (dd, J = 12.5 Hz, 1.8 Hz, 1H), 2.87 (dd, J = 12.5 Hz, 7.0 Hz, 1H), 2.60 (sept, J = 5.0 Hz, 1H), 1.19 (d, J = 6.0 Hz, 6H). ^{13}C NMR (100 MHz, $CDCl_3$, ppm): 176.7, 143.4, 134.7, 129.2, 129.2, 128.9, 128.1, 128.1, 122.2, 65.9, 60.3, 54.3, 34.0, 27.8, 19.0, 18.9. The enantiomer of **7** was also prepared in a similar fashion and has identical characterization to **7.**

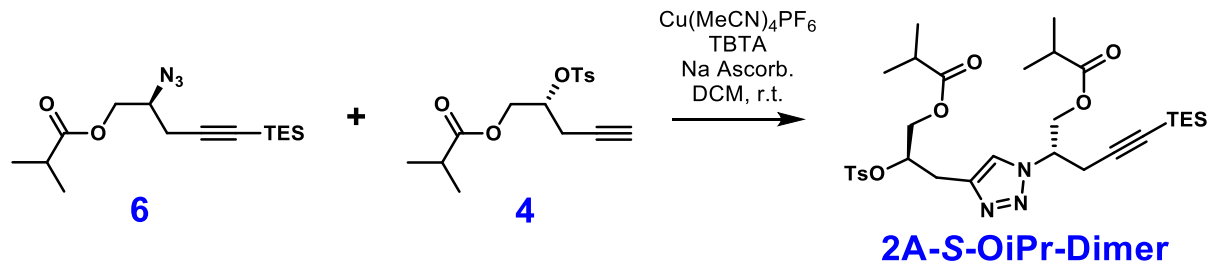

Scheme 13. Synthesis of **2A-*S*-OiPr-Dimer** from **6** and **4**.

2A-*S*-OiPr-Dimer: DCM (30 mL), tris(benzyltriazolylmethyl)amine (TBTA) (350 mg, 0.65 mmol), $Cu(MeCN)_4PF_6$ (160 mg, 0.43 mmol), and sodium ascorbate (160 mg, 0.81 mmol) were added to a mixture of **4** (5.5 g, 17.8 mmol) and **6** (6.2 g, 19.1 mmol) in an oven-dried 100 mL round bottom flask. The reaction was left at room temperature and stirred overnight. Progress of the reaction was tracked through TLC. At completion, the majority of DCM was removed under reduced pressure and the crude product was loaded onto a silica column. Column chromatography

(pure hexanes to pure DCM to 1% MeOH in DCM) was used to purify the desired product. **2A-*S*-OiPr-Dimer** was isolated as a slightly yellow viscous liquid (8.8 g, 13.9 mmol, 78% yield). ^{1}H NMR (500 MHz, $CDCl_3$, ppm) δ_H 7.76 (d, J = 8.3 Hz, 2H), 7.58 (s, 1H), 7.33 (d, J = 7.7 Hz, 2H), 4.98 (m, 1H), 4.91 (m, 1H), 4.53 (overlap, 2H), 4.20 (dd, J = 12.4 Hz, 3.5 Hz, 1H), 4.02 (dd, J = 12.4 Hz, 6.5 Hz, 1H), 3.15 (m, 2H), 2.92 (m, 2H), 2.53 (sept, J = 7.0 Hz, 1H), 2.44 (s, 3H), 2.37 (sept, J = 7.2 Hz, 1H), 1.12-1.07 (overlap, 12H), 0.94 (t, J = 7.9 Hz, 9H), 0.55 (q, J = 8.0 Hz, 6H). ^{13}C NMR (100 MHz, $CDCl_3$, ppm): 176.1, 176.1, 144.8, 141.0, 133.7, 129.7, 127.6, 122.0, 100.7, 86.4, 78.5, 63.8, 63.6, 58.6, 33.6, 33.5, 28.2, 23.3, 21.5, 18.7, 18.7, 18.6, 7.3, 4.1. **2A-*R*-OiPr-Dimer** was also prepared in a similar fashion and afforded similar yield.

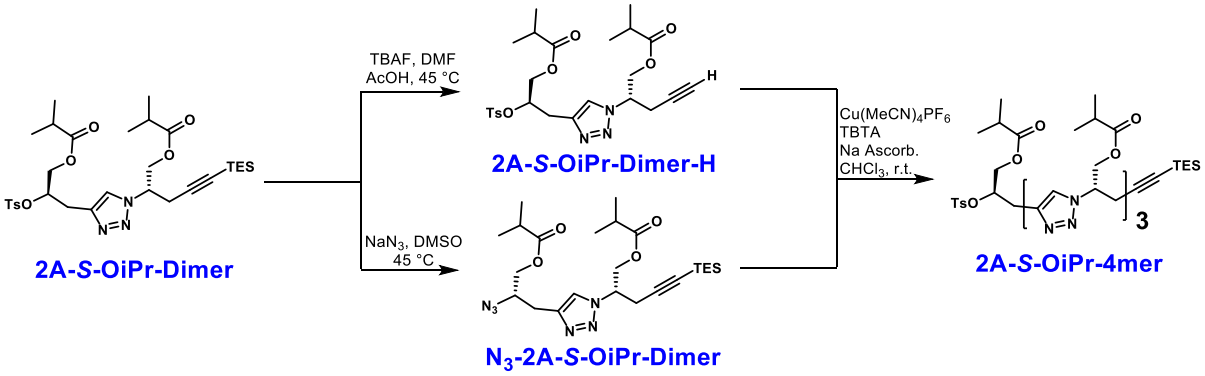

Scheme 14. Synthesis of **2A-*S*-OiPr-4mer** from **2A-*S*-OiPr-Dimer**.

2A-*S*-OiPr-4mer: The **2A-*S*-OiPr-2mer-H** precursor to **2A-*S*-OiPr-4mer** was prepared by dissolving **2A-*S*-OiPr-2mer** (2.8 g, 4.4 mmol) in DMF (20 mL) in a 40 mL scintillation vial. AcOH (263 mg, 4.4 mmol) was added to this solution. A solution of composed of a mixture of AcOH (263 mg, 4.4 mmol) and tetrabutylammonium fluoride (TBAF) (4.4 mL, 1M in THF, 4.4 mmol) was then added to reaction solution dropwise. Any additional excess AcOH will potentially slow down the reaction. The reaction was heated to 45 °C and left to react for 4 hours. The reaction was monitored by ^{1}H NMR to determine completion. After completion, 100 mL of EtOAc was added to the reaction mixture and extracted 3x with 100 mL 0.5% LiCl solution. The organic layer was isolated, dried over Na_2SO_4 and concentrated under vacuum. The resulting yellow oil containing **2A-*S*-OiPr-2mer-H** and TES-F was used directly in the next step.

The **N_3-2A-*S*-OiPr-2mer** precursor to **2A-*S*-OiPr-4mer** was prepared by dissolving **2A-*S*-OiPr-2mer** (2.8 g, 4.4 mmol) in DMSO (26 mL), followed by the addition of NaN_3 (858 mg, 13.2 mmol). The reaction mixture was heated to 45 °C and allowed to stir for 12 h before 100 mL of EtOAc was added to the reaction mixture and the solution was extracted 1x with 100 mL saturated sodium bicarbonate solution and 2x with 100 mL 0.5% LiCl solution. The organic layer was dried over Na_2SO_4 and concentrated under vacuum. The resulting **N_3-2A-*S*-OiPr-2mer** was obtained as an off-white solid and was used in the next step without further purification.

Under an N_2 atmosphere, chloroform (50 mL), $Cu(MeCN)_4PF_6$ (120 mg, 0.33 mmol), TBTA (260 mg, 0.48 mmol), and sodium ascorbate (120 mg, 0.61 mmol) were added to **N_3-2A-*S*-OiPr-2mer** in a 100 mL round bottom flask. The mixture was stirred and sonicated until the $Cu(MeCN)_4PF_6$ and TBTA are dissolved. A solution of **2A-*S*-OiPr-2mer-H** in chloroform (10 mL) was then added slowly to the above solution. The reaction mixture was warmed to 35 °C and allowed to react overnight. The reaction was tracked by TLC. Upon completion, the solution was concentrated under reduced pressure until it becomes a viscous mixture, which was then loaded carefully onto a silica column. Column chromatography (100% DCM to 1.25% MeOH/DCM then 3.5% MeOH/DCM) yielded the product **2A-*S*-OiPr-4mer** (3.8 g, 3.7 mmol, 84% yield) as an off-white solid. ^{1}H NMR (500 MHz, $CDCl_3$, ppm) δ_H 7.76 (d, J = 8.1 Hz, 2H), 7.48 (s, 1H), 7.34 (d, J = 8.0 Hz, 2H), 7.26 (s, 1H), 7.19 (s, 1H), 5.07 (overlap, 2H), 4.98 (m, 1H), 4.91 (m, 1H), 4.55-4.39 (overlap, 4H), 4.15 (dd, J = 12.5 Hz, 3.5 Hz, 1H), 3.99 (dd, J = 12.4 Hz, 6.6 Hz, 1H), 3.40-3.33 (overlap, 4H), 3.13 (m, 2H), 2.90 (m, 2H), 2.55-2.44 (overlap, 6H), 2.36 (sept, J = 7.0 Hz, 1H), 1.12-1.05 (overlap, 24H), 0.93 (t, J = 7.9 Hz, 9H), 0.55 (q, J = 7.9 Hz, 6H). ^{13}C NMR (125 MHz, $CDCl_3$, ppm): 176.4, 176.4, 176.3, 145.1, 141.9, 141.7, 141.4, 133.9, 130.0, 127.8, 122.8, 122.4, 121.7, 101.0, 86.5, 78.7, 64.8, 64.6, 63.9, 63.8, 60.1, 59.9, 58.8, 33.8, 33.80, 33.71, 28.4, 28.3, 28.1, 23.4, 21.7, 18.9, 18.9, 18.8, 7.5, 4.3. **2A-*R*-OiPr-4mer** was also prepared in a similar fashion and afforded similar yield.

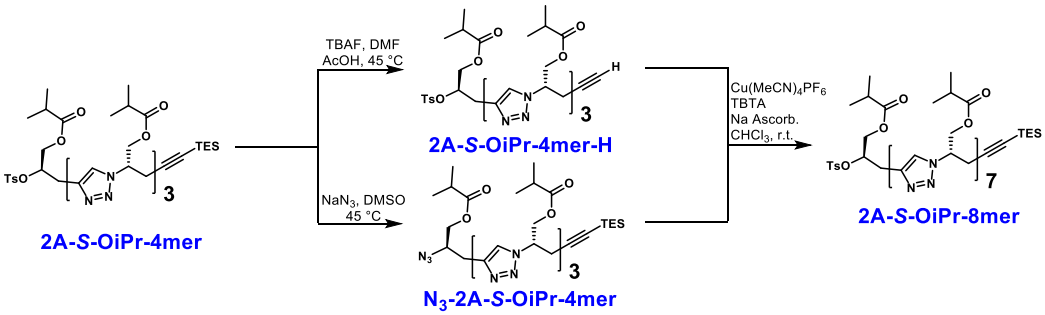

Scheme 15. Synthesis of **2A-*S*-OiPr-8mer** from **2A-*S*-OiPr-4mer**.

2A-*S*-OiPr-8mer: The **2A-*S*-OiPr-4mer-H** precursor to **2A-*S*-OiPr-8mer** was prepared by dissolving **2A-*S*-OiPr-4mer** (1.75 g, 1.7 mmol) in DMF (8.5 mL) in a 40 mL scintillation vial. AcOH (113 mg, 1.88 mmol) was added to this solution. A solution of composed of a mixture of AcOH (113 mg, 1.88 mmol) and TBAF (1.88 mL, 1M in THF, 1.88 mmol) was then added to reaction solution dropwise. Any additional excess AcOH will potentially slow down the reaction. The reaction was heated to 45 °C and left to react for 4 hours. The reaction was monitored by ^{1}H NMR to determine completion. After completion, 100 mL of EtOAc was added to the reaction mixture and extracted 1x with 100 mL saturated sodium bicarbonate solution and 2x with 100 mL 0.5% LiCl solution. The organic layer was isolated, dried over Na_2SO_4 and concentrated under vacuum. The resulting yellow oil containing **2A-*S*-OiPr-4mer-H** and TES-F was used directly in the next step.

The **N_3-2A-*S*-OiPr-4mer** precursor to **2A-*S*-OiPr-8mer** was prepared by dissolving **2A-*S*-OiPr-4mer** (1.75 g, 1.7 mmol) in DMSO (17 mL), followed by the addition of NaN_3 (332 mg, 5.1 mmol). The reaction mixture was heated to 45 °C and allowed to stir for 12 h before 100 mL of EtOAc was added to the reaction mixture and the solution was extracted 3x with 100 mL 0.5% LiCl solution. The organic layer was dried over Na_2SO_4 and concentrated under vacuum. The resulting **N_3-2A-*S*-OiPr-4mer** was obtained as an off-white solid and was used in the next step without further purification.

Under an N_2 atmosphere, chloroform (10 mL), $Cu(MeCN)_4PF_6$ (20 mg, 0.054 mmol), TBTA (43 mg, 0.08 mmol), and sodium ascorbate (20 mg, 0.1 mmol) were added to **N_3-2A-*S*-OiPr-4mer** in a 40 mL scintillation vial. The mixture was stirred and sonicated until the $Cu(MeCN)_4PF_6$ and TBTA are dissolved. A solution of **2A-*S*-OiPr-4mer-H** in chloroform (10 mL) was then added

slowly to the above solution. The reaction mixture was warmed to 35 °C and allowed to react overnight. The reaction was tracked by TLC. Upon completion, the solution was concentrated under reduced pressure until it becomes a viscous mixture, which was then loaded carefully onto a silica column. Column chromatography (100% DCM to 1.25% MeOH/DCM then 3.5% MeOH/DCM) yielded the product **2A-*S*-OiPr-8mer** (1.9 g, 1.05 mmol, 56% yield) as an off-white solid. ^{1}H NMR (500 MHz, $CDCl_3$, ppm) δ_H 7.83 (s, 1H), 7.82 (d, J = 8.3 Hz, 2H), 7.48 (s, 1H), 7.41 (s, 1H), 7.38 (d, J = 8.0 Hz, 2H), 7.26 (s, 1H), 7.24 (s, 1H), 7.09 (s, 1H), 7.08 (s, 1H), 5.33 – 4.99 (overlap, 10H), 4.92 (dd, J = 11.8 Hz, 8.9 Hz, 1H), 4.84 – 4.77 (overlap, 3Hw), 4.64 – 4.57 (overlap, 2H), 4.49 – 4.33 (overlap, 7H), 4.10 (m, 2H), 3.65 – 3.44 (overlap, 5H), 3.37 – 3.19 (overlap, 9H), 3.10 – 2.97 (overlap, 2H), 2.92 (dd, J = 17.1 Hz, 6.1 Hz, 1H), 2.62 – 2.41 (overlap, 10H), 2.29 (sept, J = 7.0 Hz, 1H), 1.17 – 0.91 (overlap, 57H), 0.55 (q, J = 8.0 Hz, 6H). ^{13}C NMR (125 MHz, $CDCl_3$, ppm): 180.0, 177.3, 176.6, 176.5, 176.5, 176.4, 176.4, 176.3, 176.3, 176.3, 176.2, 176.2, 145.4, 143.1, 142.8, 142.6, 142.6, 142.5, 140.4, 133.6, 130.0, 129.9, 128.9, 127.7, 127.7, 126.0, 122.4, 121.4, 121.2, 121.1, 120.9, 120.7, 120.2, 101.5, 101.5, 85.7, 85.7, 78.7, 64.6, 64.5, 64.4, 64.4, 64.3, 64.2, 64.1, 64.1, 63.9, 63.8, 63.8, 63.7, 63.6, 61.5, 61.5, 61.4, 61.3, 61.2, 60.9, 59.2, 33.8, 33.7, 33.6, 33.6, 33.5, 29.3, 28.5, 28.4, 27.9, 27.7, 27.7, 27.5, 23.2, 21.6, 21.3, 19.0, 18.9, 18.9, 18.8, 18.7, 18.7, 18.7, 18.6, 18.6, 7.4, 4.2. **2A-*R*-OiPr-8mer** was also prepared in a similar fashion and afforded similar yield.

3) Macromonomer Synthesis

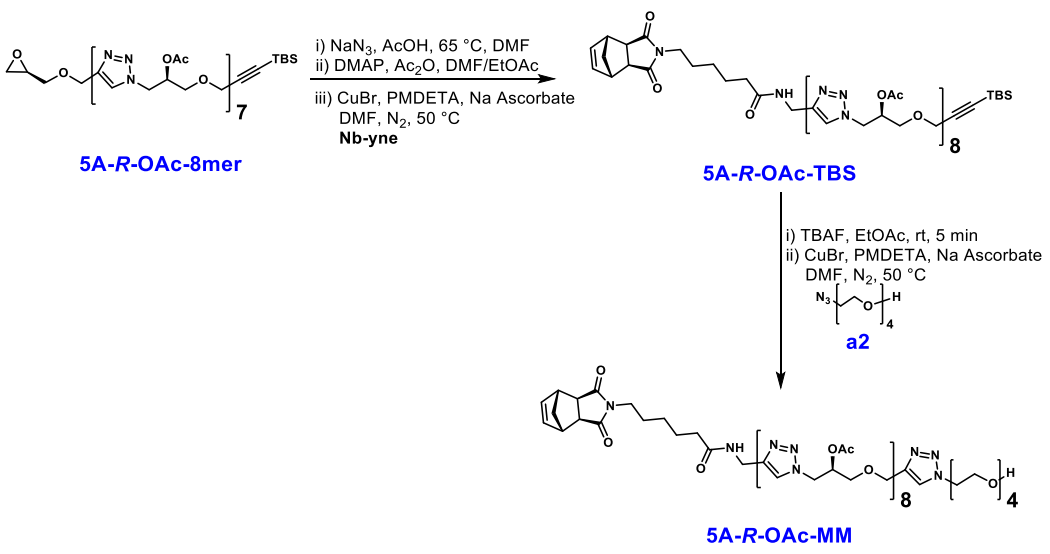

Scheme 16. Synthesis of **5A-*R*-OAc-MM**.

5A-*R*-OAc-TBS: In a RBF, **5A-*R*-OAc-8mer** (1.1 g, 0.7 mmol, 1.0 eq) was dissolved in DMF (7 mL), followed by the addition of acetic acid (63 mg, 60 µL, 1.1 mmol, 1.5 eq) and sodium azide (137 mg, 2.1 mmol, 3.0 eq). The reaction mixture was stirred at 65°C for 6 hours, and the DMF was then removed via rotary evaporator, leaving only ~0.5 mL of DMF. EtOAc (~5 mL) was then added, and the precipitated salt was filtered off. DMAP (43 mg, 0.4 mmol, 0.5 eq) and acetic anhydride (143 mg, 133 µL, 1.4 mmol, 2.0 eq) were added, and the mixture was stirred for 30 minutes. The mixture was then concentrated and pushed through a plug of silica gel using 6-7% MeOH/DCM. The resulting material was collected, concentrated under vacuum, and added to a RBF with DMF (4 mL), **Nb-yne** (340 mg, 1.1 mmol, 1.5 eq), copper (I) bromide (5 mg, 0.04 mmol, 0.05 eq), PMDETA (14 mg, 17 µL, 0.08 mmol, 0.1 eq), and sodium ascorbate (16 mg, 0.08 mmol, 0.1 eq). The reaction mixture was heated to 50°C and allowed to stir for 2 hours under nitrogen. The crude product was concentrated under vacuum and purified by column chromatography (0-10% MeOH/DCM), affording **5A-*R*-OAc-TBS** (1.3 g, 80% yield) as a white solid.

5A-*R*-OAc-MM: 5A-*R*-OAc-TBS (1.2 g, 0.6 mmol, 1.0 eq) was dissolved in EtOAc (12 mL), followed by the slow addition of TBAF (1M in THF, 700 µL, 0.7 mmol, 1.1 eq). The reaction was stirred for 5 minutes, and MeOH (5 mL) was added, followed by 5-10 minutes of stirring. The crude material was concentrated under vacuum and pished through a silica gel plug using 2-3%

MeOH/DCM. The resulting material was collected, concentrated under vacuum, and added to a RBF with DMF (5 mL), **a2** (200 mg, 1.0 mmol, 1.5 eq), copper (I) bromide (4 mg, 0.03 mmol, 0.05 eq), PMDETA (11 mg, 10 µL, 0.06 mmol, 0.1 eq), and sodium ascorbate (12 mg, 0.06 mmol, 0.1 eq). The reaction mixture was heated to 50°C and allowed to stir for 2 hours under nitrogen. The crude product was concentrated under vacuum and purified by column chromatography (2-14% MeOH/DCM), affording **5A-*R*-OAc-MM** (960 mg, 78% yield) as a white solid. MALDI: Calcd for $C_{90}H_{128}N_{29}O_{31}$: *m/z* = 2110.93 $[M+H]^+$; Found: 2111.572 $[M+H]^+$. ^{1}H NMR (500 MHz, $CDCl_3$, ppm) δ_H 7.83 (s, 1H), 7.67 (m, 7H), 7.58 (s, 1H), 6.42 (b, 1H), 6.27 (s, 2H), 5.31 – 5.25 (m, 8H), 4.70 – 4.54 (m, 32H), 4.51 – 4.41 (m, 3H), 3.87 (t, *J* = 4.0 Hz, 2H), 3.74 – 3.49 (m, 30H), 3.43 (t, *J* = 6.0 Hz, 2H), 3.25 (s, 2H), 2.67 (s, 2H), 2.18 (t, *J* = 6.0 Hz, 2H), 2.08 – 1.98 (br s, 24H), 1.67 – 1.60 (m, *2*H), 1.57 – 1.47 (m, 3H), 1.33 – 1.26 (m, 2H), 1.21 – 1.17 (d, 1H). ^{13}C NMR (100 MHz, $CDCl_3$, ppm): δ_C 178.2, 172.9, 170.0, 144.3, 137.9, 124.5, 124.1, 123.5, 72.6, 70.7, 70.6, 70.5, 70.3, 69.5, 68.2, 64.7, 61.7, 50.4, 50.1, 47.9, 45.3, 42.9, 38.5, 36.2, 35.0, 27.6, 26.6, 25.1, 21.0. This procedure was also implemented for the synthesis of the **5A-*S*-OAc-MM**, affording similar yield. MALDI: Calcd for $C_{90}H_{128}N_{29}O_{31}$: *m/z* = 2110.93 $[M+H]^+$; Found: 2111.449 $[M+H]^+$. ^{1}H NMR (400 MHz, $CDCl_3$, ppm) δ_H 7.83 (s, 1H), 7.67 (m, 7H), 7.58 (s, 1H), 6.42 (b, 1H), 6.27 (s, 2H), 5.32 – 5.28 (m, 8H), 4.70 – 4.54 (m, 32H), 4.51 – 4.42 (m, 3H), 3.87 (t, *J* = 4.0 Hz, 2H), 3.73 – 3.50 (m, 30H), 3.43 (t, *J* = 6.0 Hz, 2H), 3.25 (s, 2H), 2.66 (s, 2H), 2.18 (t, *J* = 6.0 Hz, 2H), 2.08 – 1.99 (br s, 24H), 1.67 – 1.60 (m, *2*H), 1.57 – 1.47 (m, 3H), 1.34 – 1.26 (m, 2H), 1.21 – 1.17 (d, 1H). ^{13}C NMR (100 MHz, $CDCl_3$, ppm): δ_C 178.2, 172.9, 170.0, 144.3, 137.9, 124.5, 124.1, 123.4, 72.6, 70.7, 70.6, 70.5, 70.3, 69.5, 68.2, 64.7, 61.7, 50.4, 50.1, 47.9, 45.3, 42.9, 38.5, 36.3, 35.0, 27.6, 26.6, 25.1, 21.0.

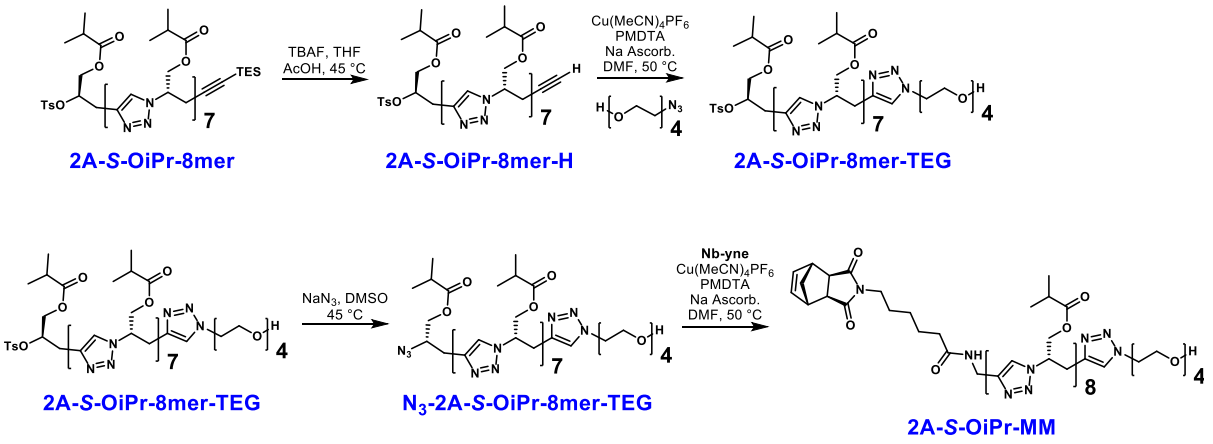

Scheme 17. Synthesis of **2A-*S*-OiPr-MM** from **2A-*S*-OiPr-8mer**.

2A-*S*-OiPr-8mer-TEG: 2A-*S*-OiPr-8mer (1.5 g, 0.84 mmol) was dissolved in DMF (8 mL), followed by the addition of AcOH (63 mg, 1.04 mmol). A solution of composed of a mixture of AcOH (63 mg, 1.04 mmol) and TBAF (1.04 mL, 1M in THF, 1.04 mmol) was then added to reaction solution dropwise. Any additional excess AcOH will potentially slow down the reaction. The reaction was heated to 45 °C and left to react for 4 hours. The reaction was monitored by ^{1}H NMR to determine completion. After completion, 100 mL of EtOAc was added to the reaction mixture and extracted 1x with 100 mL saturated sodium bicarbonate solution and 2x with 100 mL 0.5% LiCl solution. The organic layer was isolated, dried over Na_2SO_4 and concentrated under vacuum. The compound was then transferred to a 40 mL scintillation vial and DMF (10 mL), **TEGN$_3$** (466 mg, 2.22 mmol), $Cu(MeCN)_4PF_6$ (20 mg, 0.054 mmol), PMDETA (19 mg, 0.11 mmol), and sodium ascorbate (20 mg, 0.1 mmol) were also added to the vial. The reaction mixture was heated to 50 °C and allowed to stir for 2 hours under nitrogen. The reaction solution was run through a neutral alumina column with 5% MeOH/DCM to remove copper. The solvent was removed under reduced pressure and **2A-*S*-OiPr-8mer-TEG** was purified through preparatory GPC to yield **2A-*S*-OiPr-8mer-TEG** (1.02 g, 0.53 mmol, 64% yield) as a white solid.

2A-*S*-OiPr-8mer-TEG (1.0 g, 0.53 mmol) was dissolved in DMSO (15 mL) followed by the addition of NaN_3 (100 mg, 1.5 mmol). The reaction mixture was heated to 45 °C and allowed to stir for 12 h before 100 mL of EtOAc was added to the reaction mixture and the solution was extracted 3x with 100 mL 0.5% LiCl solution. The organic layer was dried over Na_2SO_4 and concentrated under vacuum which resulted in crude **N$_3$-2A-*S*-OiPr-8mer-TEG**. DMF (15 mL),

Nb-yne (630 mg, 2.0 mmol), $Cu(MeCN)_4PF_6$ (20 mg, 0.054 mmol), PMDETA (19 mg, 0.11 mmol), and sodium ascorbate (20 mg, 0.1 mmol) were also added to **N_3-2A-*S*-OiPr-8mer-TEG**. The reaction mixture was heated to 50 °C and allowed to stir for 2 hours under nitrogen. The reaction solution was run through a neutral alumina column with 5% MeOH/DCM to remove copper. The solvent was removed under reduced pressure and the crude product was purified through preparatory GPC to yield **2A-*S*-OiPr-MM** (820 mg, 0.39 mmol, 74% yield) as a white solid. MALDI-TOF-MS: Calcd for $C_{98}H_{144}N_{29}O_{23}$: *m/z* = 2097.86 $[M + H]^+$; Found: 2097.35 $[M+H]^+$. ^{1}H NMR (500 MHz, $CDCl_3$, ppm) δ_H δ 7.87 (s, 1H), 7.32 (s, 1H), 7.27 (s, 1H), 7.24 (s, 1H), 7.22 (s, 1H), 7.17 (s, 1H), 7.15 (s, 1H), 6.99 (t, *J* = 5.7 Hz), 6.87 (s, 1H), 6.29 (s, 2H), 5.49-5.34 (overlap, 5H), 5.28-5.04 (overlap, 10H), 4.98 (t, *J* = 10.1 Hz, 1H), 4.78-4.70 (overlap, 2H), 4.66-4.53 (overlap, 4H), 4.47-4.31 (overlap, 10H), 3.98-3.89 (overlap, 2H), 3.75-3.56 (overlap, 20H), 3.48-3.44 (overlap, 3H), 3.38 (dd, *J* = 15.5 Hz, 4.2 Hz), 3.31-3.16 (overlap, 11H), 2.85 (t, *J* = 13.3 Hz, 1H), 2.68 (s, 2H), 2.62 (sept, *J* = 7.0 Hz, 1H), 2.55 – 2.33 (overlap, 7H), 2.15 (pent, *J* = 7.4 Hz, 1H), (2.06, *J* = 7.2 Hz, 1H), 1.72-1.51 (overlap, 23H), 1.34-1.28 (overlap, 2H), 1.25-1.16 (overlap, 9H), 1.10-0.82 (overlap, 49H). ^{13}C NMR (125 MHz, $CDCl_3$, ppm): 178.1, 177.1, 176.7, 176.7, 176.7, 176.7, 176.4, 176.3, 173.3, 146.5, 143.1, 143.0, 143.0, 142.8, 142.6, 142.5, 142.1, 137.9, 123.5, 121.1, 120.8, 120.7, 120.6, 120.4, 120.4, 119.8, 72.6, 70.6, 70.5, 70.5, 69.6, 65.0, 65.0, 64.8, 64.7, 64.5, 64.3, 64.1, 62.0, 61.8, 61.7, 61.6, 61.5, 61.4, 61.0, 60.8, 50.0, 47.9, 47.9, 45.2, 42.8, 38.4, 36.1, 35.3, 33.9, 33.8, 33.8, 33.7, 33.7, 33.7, 33.6, 29.0, 28.9, 28.0, 27.9, 27.9, 27.8, 27.8, 27.7, 27.5, 26.6, 25.2, 19.1, 19.0, 18.9, 18.9, 18.9, 18.9, 18.8, 18.8, 18.7, 18.7. **2A-*R*-OiPr-MM** was also prepared in a similar fashion and afforded similar yield.

4) Fluorescent Monomer Synthesis (**Cy-M**):

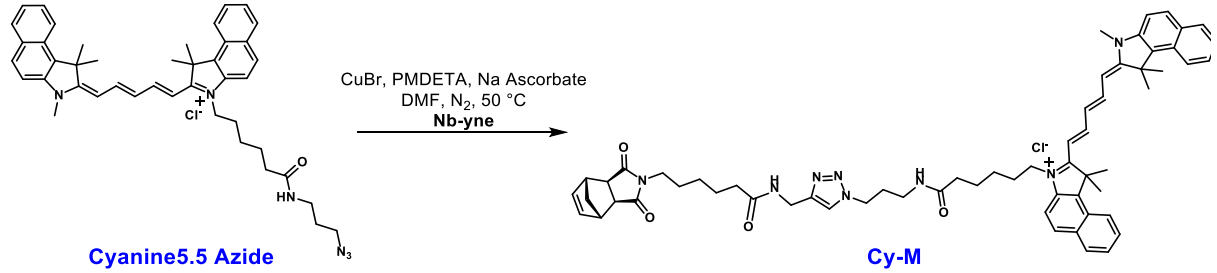

Scheme 18. Synthesis of the **Cy5.5-M**.

Cy5.5-M: Nb-yne (9 mg, 0.03 mmol, 1.5 eq) and Cyanine5.5 azide (Lumiprobe, 13 mg, 0.02 mmol, 1.0 eq) was dissolved in DMF (2 mL), followed by the addition of copper (I) bromide (1

mg, 0.001 mmol, 0.05 eq), PMDETA (1 mg, 1 µL, 0.002 mmol, 0.1 eq), and sodium ascorbate (1 mg, 0.002 mmol, 0.1 eq). The reaction mixture was heated to 50°C and allowed to stir for 3 hours under nitrogen. The mixture was then allowed to cool to room temperature, and concentrated under vacuum. DCM (50 mL) was then added, and the solution was washed with brine (3 × 50 mL). The organic layer was collected, dried over Na_2SO_4, and concentrated under vacuum. The crude mixture was then purified by column chromatography (0-15% MeOH/DCM), affording **Cy5.5-M** (31 mg, 82% yield) as a blue solid. HRMS-ESI: Calcd for $C_{61}H_{71}N_8O_4Cl$: *m/z* = 979.5593 [*M* + Cl]; Found: 979.5580 [*M* + Cl]. ^{1}H NMR (500 MHz, $CDCl_3$, ppm) δ_H 8.73 (s, 1H), 8.32 (s, 1H), 8.09 (d, *J* = 9.0 Hz, 2H), 7.95 – 7.84 (m, 4H), 7.64 – 7.59 (m, 2H), 7.53 – 7.39 (m, 2H), 7.41 (d, *J* = 9.0 Hz, 1H), 7.37 (d, *J* = 8.7 Hz, 1H), 7.28 – 7.21 (m, 1H), 6.86 (t, *J* = 12.4 Hz, 1H), 6.64 (d, *J* = 13.7 Hz, 1H), 6.28 – 6.19 (m, 2H), 4.56 (d, *J* = 5.0 Hz, 2H), 4.50 (t, *J* = 6.5 Hz, 2H), 4.24 (*t*, J = 7.8 Hz, 2H), 3.71 (s, 2H), 3.40 (t, *J* = 7.5 Hz, 2H), 3.25 – 3.18 (m, 3H), 2.62 (s, 2H), 2.44 (t, *J* = 7.1 Hz, 2H), 2.29 (*t*, J = 7.6 Hz, 2H), 2.24 – 2.17 (m, 2H), 1.99 (s, 9H), 1.90 (p, *J* = 7.8 Hz, 2H), 1.80 (p, *J* = 7.3 Hz, 2H), 1.65 (p, *J* = 9.3 Hz, 2H), 1.59 – 1.50 (m, 4H), 1.47 (t, *J* = 9.9, 1H), 1.34 – 1.16 (m, 8H), 0.90 – 0.81 (m, 3H). ^{13}C NMR (126 MHz, $CDCl_3$, ppm) δ_C 178.2, 174.5, 173.8, 173.3, 144.3, 140.3, 139.4, 137.9, 134.2, 133.2, 132.2, 131.9, 131.1, 130.8, 130.4, 130.3, 129.9, 128.3, 128.2, 127.9, 126.2, 125.4, 125.1, 124.2, 122.1, 110.9, 110.4, 109.9, 104.5, 103.0, 77.4, 77.2, 76.9, 51.3, 50.9, 48.0, 47.9, 45.3, 42.9, 38.7, 36.2, 36.1, 35.7, 29.8, 27.9, 27.7, 27.4, 26.8, 26.3, 25.4, 25.2.

5) Procedure for Bottlebrush Polymer Syntheses

*a) **5A-Poly-R-Cy** and **5A-Poly-S-Cy:***

5A-Poly-*R*-Cy: Fresh solution of **Cy-M** in DCM was prepared (**Cy5.5-Stock**, 15.4 mg/mL). To a vial containing a stir bar, **5A-*R*-OAc-MM** (35.9 mg, 17.0 µmol, 25.0 eq) and **Cy-M** (44.9µL from **Cy5.5-Stock**, 0.68 µmol, 1.0 eq) was added. To another vial, a solution of Grubbs 3rd generation bispyridyl catalyst **G3** (0.02 M in DCM) was freshly prepared. DCM (261 µL) was then added to the **MM** vial, followed by the addition of **G3** solution (34.0 µL, 0.68 µmol, 1.0 eq) to give the desired **MM:G3** ratio of **26:1**, while achieving a total **MM** concentration of **0.05 M**, affording a dark blue solution. The reaction mixture was allowed to stir for 12 hours at room temperature. To quench the polymerization, a drop of ethyl vinyl ether was then added, and an aliquot was taken out for GPC analysis. This procedure was also implemented for the synthesis of the **5A-Poly-*S*-Cy**.

*b) **5A-Poly-RS:***

To a vial containing a stir bar, **5A-*R*-OAc-MM** (28.3 mg, 13.4 µmol, 12.5 eq) and **5A-*S*-OAc-MM** (28.3 mg, 13.4 µmol, 12.5 eq) were added. To another vial, a solution of Grubbs 3rd generation bispyridyl catalyst **G3** (0.02 M in DCM) was freshly prepared. DCM (483 µL) was then added to the **MM** vial, followed by the addition of **G3** solution (53.6 µL, 1.07 µmol, 1.0 eq) to give the desired **MM:G3** ratio of **25:1**, while achieving a total **MM** concentration of **0.05 M**, affording a yellow solution. The reaction mixture was allowed to stir for 12 hours at room temperature. To quench the polymerization, a drop of ethyl vinyl ether was then added, and an aliquot was taken out for GPC analysis.

*c) **2A-Poly-R-Cy** and **2A-Poly-S-Cy:***

2A-Poly-*R*-Cy: Fresh solution of **Cy-M** in DCM was prepared (**Cy5.5-Stock**, 15.4 mg/mL). To a vial containing a stir bar, **2A-*R*-OiPr-MM** (35.9 mg, 17.0 µmol, 25.0 eq) and **Cy-M** (44.9µL from **Cy5.5-Stock**, 0.68 µmol, 1.0 eq) was added. To another vial, a solution of Grubbs 3rd generation bispyridyl catalyst **G3** (0.02 M in DCM) was freshly prepared. DCM (261 µL) was then added to the **MM** vial, followed by the addition of **G3** solution (34.0 µL, 0.68 µmol, 1.0 eq) to give the desired **MM:G3** ratio of **26:1**, while achieving a total **MM** concentration of **0.05 M**, affording a dark blue solution. The reaction mixture was allowed to stir for 12 hours at room temperature. To quench the polymerization, a drop of ethyl vinyl ether was then added, and an aliquot was taken out for GPC analysis. This procedure was also implemented for the synthesis of the **2A-Poly-*S*-Cy**.

Section D. Small-Angle Neutron Scattering (SANS) Measurements

Methods

Small-angle neutron scattering (SANS) measurements were performed on the NG7 30 m SANS instrument at the NIST Center for Neutron Research (Gaithersburg, MD). Scattered neutron intensities were collected at two sample-to-detector distances of 1 m and 4 m. The resulting data covered a q-range from 0.01 $Å^{-1}$ to 0.5 $Å^{-1}$, where the scattering variable q is defined in terms of the neutron wavelength (λ) and scattering angle (θ) as $q = (4\pi/\lambda)\sin(\theta/2)$. The neutron wavelength was $\lambda = 6$ Å. The data were corrected for background radiation and scattering from the sample cell using standard methods, and placed on to an absolute scale using the empty beam flux.

Analysis

SANS measurements of the macromonomer **2A-*S*-OH-MM** are shown in Supplementary Figure 63, along with a fit to a form factor describing a polymer with excluded volume.[6] The results find a radius of gyration $R_g = 1.2$ nm. The physical interpretation of the radius of gyration is illustrated in the inset of the figure.

SANS measurements of the bottlebrushes are shown in Supplementary Figure 64. The data were fit according to a flexible cylinder model,[7] with a power law term which accounts for the upturn in the intensities at low values of q due to clustering/aggregation of polymers in solution. This upturn is a common feature of aqueous polymer solutions.[6,8-10] Note that the use of the flexible cylinder model assumes that the bottlebrush is of uniform density, which is not true for a polymer, as shown in the illustration in Supplementary Figure 64. For this reason, if no significant change in the conformation of the macromonomer (e.g., **2A-*S*-OH-MM**) occurs upon polymerization, then the expected radius of the bottlebrush using the flexible cylinder model is expected to be roughly twice the radius of gyration of the macromonomer $r_c \approx 2R_g$, leading to a bottle brush diameter on the order of 2.4 nm. The best fits indicated that sample **2A-*S*-Cy** had a length $l_c = 9$ nm and diameter $r_c = 2.5$ nm, which is in quantitative agreement with the value estimated from the macromonomer size. Sample **5A-*R*-Cy**, which was prepared from a slightly larger macromonomer, was found to have length $l_c = 10$ nm and radius $r_c = 2.8$ nm. The increase in the backbone length of the polymer with a greater side chain length is in agreement with behaviors

observed previously by Pesek *et al.*[7] In addition, the similarity between the radii of **2A-*S*-Cy** and **5A-*R*-Cy** agrees well with our molecular dynamics simulations (Figure 4, main text).

The diameter of the bottlebrush can also be compared to DLS measurements if the radius of gyration of the bottlebrush cross-section is estimated. This is because DLS calculates an effective size on the basis of the diffusion coefficient of the mass fractal (*i.e.*, bottlebrush), whereas the radius obtained by the flexible cylinder model assumes a non-fractal structure. For this reason, the radius of gyration of the cross-section is related to, but a different quantity, than the one obtained from the flexible cylinder model. The radius of gyration quantifies the average distance of each monomer from the center of mass of the molecule. In terms of the bottlebrush cross-section, this implies that after polymerization of the MMs, the center of mass would shift to the backbone of the bottlebrush. We estimated that the diameter of the bottlebrush, in terms of R_g of the MM, would be $D = 2R_g$, which is smaller than what would be obtained if the MMs were not mass fractals. More quantitatively, if the cross-section of the bottlebrush was treated analogously to a star polymer with $f = 2$ arms, then the radius of gyration of the bottlebrush (BB) cross-section would be $R_{g,BB} \approx R_{g,MM}\sqrt{3 - 2/f} = 1.4R_{g,MM}$, and the diameter would be 2.8 times the radius of gyration of the MM. Using the measured value of $R_{g,MM} = 1.2$ nm, this leads to a diameter of the molecule on the order of 3 nm, which is in quantitative agreement with the values of D_h reported in the main text.

Section E. Molecular Dynamics Simulations of 2A and 5A IEG MMs

E1. Simulation of 2A-*R*-OH-MM and 5A-*R*-OH-MM trajectories

The initial PDB structures for the macromonomers were generated using RDKit v2019.03.[11] A truncated version was used to obtain the topology and OPLS-AA forcefield parameters files from LigParGen (http://zarbi.chem.yale.edu/ligpargen/, accessed on 7th July 2019).[12-14] TIP3P model was used to represent the water molecules.[15]

2A-*R*-OH-MM structure was solvated in 9 x 9 x 9 nm^3 box, and **5A-*R*-OH-MM** structure was solvated in 9.5 x 9.5 x 9.5 nm^3 box. All covalent bonds involving hydrogen atoms were constrained using SHAKE algorithm.[16] A cut Particle Mesh Ewald algorithm of with a cutoff at 1 nm was applied for the non-bonded interactions.[17] NVT simulation was carried out with a Langevin thermostat[18] in OpenMM 7.3.1.[19] We performed 6 simulations per system.

The starting point for one simulation was obtained from low-energy configuration generated using random distance matrix approach in RDKit. This configuration was directly solvated with explicit water molecules. The system was minimized for 10,000 iterations and then allowed to equilibrate for 25 ns. The analysis was performed on the following 1 μs trajectory after the equilibration.

Five different uncorrelated starting points were obtained from a high temperature 500K simulation. For the high temperature simulation, each system was run at 300 K for 10 ns, ramped up to 500 K over 10 ns with 1000 steps for every 0.04 K increase in temperature, and 100 ns at 500 K. 5 frames per system, snapshotted at 40, 60, 80, 100 and 120 ns, were used to initialize 1035 ns - 10 ns for cooling from 500 K to 300 K using the same simulation and temperature step as heating, 25 ns for equilibration, followed by 1 μs for production run.

E2. Analysis of 2A-*R*-OH-MM and 5A-*R*-OH-MM trajectories

The trajectories were analyzed using MDTraj 1.9.5,[20] and visualized using VMD 1.9.3.[21] Time-Structure Independent Component (tIC) analysis was performed using MSMBuilder 3.8.0.[22] All backbone dihedrals (except those inside the triazole units) in the middle segment were used for tICA analyses.

Root mean square distance [Supplementary Figure 67], radius of gyration-squared [Supplementary Figure 68] and end-to-end distance between triazoles with respect to the first triazole

[Supplementary Figure 69] were calculated for the structures along the trajectory. The statistical exploration of the states is evident from the plot where the structures have values on either side of mean. It may be noted that the standard deviation is slightly larger, on the order of 1 - 10 pm, in the case of **5A-*R*-OH-MM** in comparison to **2A-*R*-OH-MM**. End-to-end distance [Supplementary Figure 70] between the ends were calculated along the trajectory. **2A-*R*-OH-MM** has very sharp structure, particularly when we exclude the capping groups. **5A-*R*-OH-MM** has a wider distribution, indicative of an unfolded, coiled state. The end-to-end distance distribution remains similar when we plot it for individual replicates of **2A-*R*-OH-MM** and **5A-*R*-OH-MM** [Supplementary Figure 71]**.** Variation of dihedrals [Supplementary Figure 72] indicate statistical exploration of the conformational space without any abnormalities.

E3. Markov state modeling of 2A-*R*-OH-MM and 5A-*R*-OH-MM trajectories

Hyperparameters for tIC, microstate and macrostate MSMs were optimized [Figures S73, S74]. tIC lag time was optimized for 2-component tIC models by constructing multiple tIC models for 0-10 ns lag time. The optimized tIC lag time was chosen by visual inspection, where the ITS versus lag time plot starts to converge. Number of microstates for the MSM was optimized by 3-fold cross validation of generalized matrix Rayleigh quotient (GMRQ) score,[23] where the mean train and test scores are calculated for MSMs with 1, 3, 10, 30, 100, 300 and 1000 microstates. Optimal number of microstates was chosen based on the maximum test GMRQ score. Multiple MSM models with optimized number of microstates were constructed for 0-10 ns lag time. The optimized MSM lag time was chosen by visual inspection, where the ITS versus lag time plot converges. The final MSM model was constructed using optimized number of microstates and lag time. For both 2A-R-OH-MM and 5A-R-OH-MM, the tIC lag time was 1 ns, optimal number of microstates was 1000, and microstate MSM lag time was 5 ns.

The number of macrostates was optimized by Bayes' factor obtained from Bayesian agglomerative clustering engine[24] (BACE) [Supplementary Figure 75]. Using BACE over microstate MSM, we obtained the Bayes factors for 1-25 macrostates. The optimal number of macrostates was chosen once the Bayes factor had converged, based on the reasoning that lower the Bayes factor, higher the probability of macrostate MSM capturing all necessary conformational states. To construct macrostate MSMs, we selected 4 macrostates for 2A-R-OH-MM, and 6 macrostates for 5A-R-OH-MM. From Supplementary Figure 75, we note that the Bayes factor versus number of

macrostates trend has converged for 2A-R-OH-MM, while the trend for 5A-R-OH-MM decays relatively slowly. These trends indicate that 2A-R-OH-MM has stronger preferences for distinct conformational states, in comparison to 5A-R-OH-MM.

The transition matrix and network were constructed from the macrostate MSMs [Manuscript Figure 4d-f]. For 2A-R-OH-MM, a single macrostate (macrostate-3) is strongly preferred over others, with probability of being in the same state as 0.88, and other macrostates transitioning into it with 0.35, 0.39 and 0.66 transition probabilities. The three other macrostates in 2A-R-OH-MM have significantly probability of being in the same state, being 0.41, 0.43 and 0.53, respectively. Also, the transition probabilities between the non-macrostate-3 macrostates are less than 0.05 for all but one, where it is 0.23 to macrostate-2, which in turn has the highest transition probability (0.66) of moving to macrostate-3. The transition probabilities further cement the argument of a single preferred conformational state for 2A-R-OH-MM. In contrast, there is no single preferred macrostate for 5A-R-OH-MM with a significantly large number of macrostate transition probabilities being greater than 0.10, and almost all macrostates having ~0.50 or less probability of being in the same state.

All MSM analyses were performed on the post-equilibration 1 μs trajectory of each replicate using MDTraj,[20] PyEMMA 2.5.9,[25] and MSMBuilder.[22] Representative conformations for the transition network were sampled around macrostate cluster centers and visualized using PyMOL 2.4[26]

E4. Calculation of mirror symmetry of 2A-*R*-OH-MM and 5A-*R*-OH-MM trajectories

Mirror symmetry was calculated for all 120,000 frames of concatenated **2A-*R*-OH-MM** and **5A-*R*-OH-MM** trajectories using code obtained from ProteinCSM 1.0.1 GitHub repository (https://github.com/continuous-symmetry/proteincsm, accessed on March 1, 2021).[27,28] For the calculations, we removed all hydrogen atoms, prevented atom permutations, and obtained bond connectivities using OpenBabel 2.4.1.[29] Supplementary Figure 76 shows that both 2A-R-OH-MM and 5A-R-OH-MM explore similar chiral conformational space. Supplementary Figure 77 indicates that the regions in the tICA plot do not have strong dependence on the mirror symmetry values, and that the distribution of symmetry values are almost uniform in all regions. Mirror symmetry values for both macromonomers is noted to be statistically significant.

E5. Methods for *ab initio* simulation of CD spectra

Ground state quantum chemistry calculations were performed with Orca 4.1.1.[30] The geometry of the triazole was optimized using DFT with the wB97X-D3 functional[31] and the def2-TZVP basis.[32] We used the resolution of identity approximation ("RIJCOSX"),[33-39] the "Grid5 FinalGrid6" grid option, and the "TightSCF" self-consistent field option. Excited state properties were calculated with Gaussian using TDDFT/TDA, with the wB97X-D2 functional and the def2-TZVP basis. Five excited states were included in the calculation.

Excited state energies, transition dipole moments, transition magnetic dipole moments, and transition Mulliken charges were calculated for each state. The reduced electronic Hamiltonian was constructed for each MD geometry using Eq. (13) in Ref 40, with the inter-site couplings given by Eq. (16) using Mulliken transition charges. Intra-site couplings were set to 0 as these usually to have a negligible effect on CD spectra.[41] The Hamiltonian was diagonalized at each frame, yielding the modified excitation energies and transformation matrix. The transformation matrix was applied to the bare magnetic and transition dipole moments (Eq. (12) in Ref. 40), yielding modified moments for each new excitation energy. The associated CD signal at each energy was obtained from the modified moments using Eq. (4) of Ref 40. This process was repeated at each frame, yielding a set of energies and signals for the entire run. The spectrum was constructed by averaging Gaussian functions of width 12 nm centered on each excitation energy and multiplied by the corresponding signal. The final spectrum was red-shifted by 44 nm, the difference between the experimental triazole excitation energy (230 nm) and the second TDDFT excitation energy (186 nm). The second excitation energy was chosen as it had a significantly higher oscillator strength than the first (0.0827 vs. 0.0090). It therefore represented the most likely transition for the lowest energy experimental peak.

E6. Simulations and analysis of stereoisomers of 2A-*R*-OH-MM and 5A-*R*-OH-MM

Molecular dynamics simulations for a few selected alternative stereo configurations in the backbone were conducted (Supplementary Table 2). The starting point for each simulation was obtained from low-energy configuration generated using random distance matrix approach in RDKit, followed by solvation with explicit water molecules, energy minimization for 10,000, equilibration for 25 ns, and production run for 1 μs. The analysis was performed on the production trajectory of 1 μs. All simulation and analysis parameters were similar to the ones used for **2A-*R*-OH-MM** and **5A-*R*-OH-MM** systems.

The stereoisomers of **2A-*R*-OH-MM** and **5A-*R*-OH-MM** have varying degrees of rigidity, as noted from the RMSD, Rg and RDF, in comparison to the original structures (Figures S78 and S79). The tICA analysis shows that **2A-*R*-OH-MM** stereoisomers have a stronger preference to have a particular conformation than **5A-*R*-OH-MM** stereoisomers (Figures S80 and S81). In summary, **2-A** chains are conformationally more rigid than their **5-A** counterparts.

Section F. Modeling the Influence of Stereochemistry and Sidechain Flexibility in Surface-Ligand Binding

To examine the interplay between side-chain stereochemistry and flexibility in protein binding, we have devised a simplified physical model. Each model contains a rigid binding surface, meant to represent the surface of chiral biomolecules in a biological system (e.g., a protein), and a dilute concentration of mobile particles capable of interacting with the surface with a variable binding strength, parameterized by ϵ, in a periodically replicated 2D unit cell.

We have used the general purpose particle simulation toolkit, HOOMD-blue v2.9.4,[42] to construct a physical model consisting of a 2D periodic unit cell filled with a racemic mixture of 2D chiral binding particles (BPs), which preferentially bind to a rigid wall composed of two surfaces with chiral binding sites. The rigid wall has a fixed position that bisects the vertical coordinate (y-coordinate) of the unit cell. The "*S*" BPs have the correct handedness to bind to the top surface of the wall; the "*R*" BPs have the correct handedness to bind to the bottom surface. Supplementary Figure 90 contains snapshots that illustrate the geometry of the unit cell and the labeling and coloring of the "*S*"- and "*R*"-enantiomers of the BPs.

Both the polymers and the rigid wall are composed of hard-sphere particles of diameter d_{polymer} and d_{wall}, respectively. The backbone of each BP consists of 11 hard-sphere particles and are kept rigid with HOOMD-blue rigid body constraints.[43] Each polymer contains six side-chains, four of which have an equal length of three hard-spheres, while the remaining two side-chains have a length of two and one hard spheres, respectively. Chirality is imposed by altering the location of the shortened side-chains in the local coordinate system of the polymer such that two otherwise identical polymer particles are non-superimposable mirror images in the 2D plane. Rigid particle constraints are again used to keep the side-chains fixed in the rigid polymer model. Flexible side-chains are modeled by adding harmonic bonds to the side-chain particles with a force constant of 1,000 kJ/nm^2 and a bond length of 1 nm.

To investigate the effects of binding site geometry on ligand binding affinity we considered three different wall geometries. In the ideal case, the diameters of the wall and polymer particles are equal, $d_{\text{wall}} = d_{\text{polymer}} = 1$ nm, in reduced units. The geometry of the system in this case is such that the ligands bind to the wall in a perfect lock-and-key fashion. In the other two geometries, the

diameter of the wall particles are scaled by a small amount to make the binding site geometry slightly incommensurate with the geometry of the ligands. In one case the diameter of the wall particles is scaled by 5%, *i.e.*, $d_{\mathrm{wall}} = 1.05 \times d_{\mathrm{polymer}}$, and in another the diameter of the wall particles is scaled by 10%, *i.e.,* $d_{\mathrm{wall}} = 1.1 \times d_{\mathrm{polymer}}$.

In each system we studied there are 80 BPs, 40 of each enantiomer. The rigid wall contains 20 possible binding sites for each enantiomer with 40 binding sites in total. The dynamics were propagated with Langevin dynamics at 300 K, or in the units employed by HOOMD-blue $k_{\mathrm{B}}\mathrm{T}$ = 2.49 kJ/mol, with a time step of 0.001 ps. The inter- and intra-particle interactions within the polymers are modeled with a force-shifted Lennard-Jones potential with a cut-off of $r_{\mathrm{cut}} = 2^{1/6}\sigma$, where σ is equal to the diameter of the particle. This potential allows us to model the excluded volume interactions of the polymers without complicating the ensemble statistics in considering their mutual attraction. The binding affinity of the polymers to the rigid surface is modeled with a Lennard-Jones potential where we account for different binding affinities with a parameter ϵ. We randomized the polymer coordinates by first performing a simulation at $k_{\mathrm{B}}\mathrm{T}$ = 10.0 kJ/mol without polymer-wall attractive interactions for a time of 50 ns. The coordinates from the last snapshot of this initial high-temperature simulation were then used as a starting point for simulations at $k_{\mathrm{B}}\mathrm{T}$ = 2.49 kJ/mol, which were also 50 ns long. Coordinates from the last 20 ns of the trajectories were used in the analysis.

A bound ligand state is defined using a distance metric as an order parameter. A BP is considered bound to the surface if the particle at the center of the rigid backbone is within 4–5 nms from the center wall atoms, which have a y-coordinate of 0.0 within our unit cell. This order parameter is reasonable because only perfectly bound ligands can have the minimum distance of 4 nm. With this definition, the fraction of binding sites occupied by their matching ligands is $f_{\mathrm{occupied}} = [n_R P_R(y_{\mathrm{bind}}) + n_S P_S(y_{\mathrm{bind}})]/n_{\mathrm{sites}}$ where P_X is the probability of the central particle within the BP with chirality x being located at their respective binding locations, as described above. The number of X enantiomers is denoted n_X and the number of binding sites is denoted n_{sites}.

We now compare the impacts of side-chain flexibility and rigidity on the BP binding affinity to the wall. As expected, when the binding site geometry exactly matches the geometry of the BP, as it does when $d_{\mathrm{wall}} = d_{\mathrm{polymer}}$, the rigid enantiomers maximally bind to their respective surfaces

with a binding affinity of 2.0 kJ/mol. The BPs with flexible side-chains, in comparison, pay an entropic cost to confine their side-chains within the binding site, which is reflected in the peak in f_{occupied} occurring at a slightly higher binding affinity of 2.5 kJ/mol. Further, about half as many flexible ligands bind to the surface compared to their rigid counterparts, but this observation could be due to the flexible ligands having slower binding kinetics than the ligands with rigid side-chains.

By contrast, as the binding site geometry becomes incommensurate with the geometry of the ligands, which is expected to be the case for the bottlebrush polymers studied experimentally in this work, the number of ligands with rigid side-chains correctly bound to the surface decreases, becoming 0.0 for a wall geometry just 10% different from the ideal geometry. In stark contrast, the ligands with flexible side-chains are capable of binding to the surface despite the distorted binding geometry. This observation highlights the ability of polymeric ligands with flexible side-chains to bind to heterogeneous surfaces compared to their rigid side-chain counterparts. In a homochiral biological system, we would therefore expect to observe a greater difference in properties between enantiomers of flexible polymers than comparably rigid ones, as shown herein for **5A-*R*** versus **5A-*S*** compared to **2A-*R*** and **2A-*S***.

Section G. References

1. Barnes, J. C., Ehrlich, D. J.-C., Gao, A. X., Leibfarth, F. A., Jiang, Y., Zhou, E., Jamison, T. F. & Johnson, J. A. Iterative exponential growth of stereo- and sequence-controlled polymers. *Nat. Chem*. **7**, 810-815 (2015).
2. Jiang, Y., Golder, M. R., Nguyen, H. V.-T., Wang, Y., Zhong, M., Barnes, J. C., Ehrlich, D. J.-C. & Johnson, J. A. Iterative exponential growth synthesis and assembly of uniform diblock copolymers. *J. Am. Chem. Soc*. **138**, 9369-9372 (2016).
3. Patel, P. R., Kiser, R. C., Lu, Y. Y., Fong, E., Ho, W. C., Tirrell, D. A. & Grubbs, R. H. Synthesis and cell adhesive properties of linear and cyclic RGD functionalized polynorbornene thin films. *Biomacromolecules* **13**, 2546-2553 (2012).
4. DeForest, C. A. & Tirrell, D. A. A photoreversible protein-patterning approach for guiding stem cell fate in three-dimensional gels. *Nat. Mater.* **14**, 523-531 (2015).
5. Love, J. A., Morgan, J. P., Trnka, T. M. & Grubbs, R. H. A practical and highly active ruthenium-based catalyst that effects the cross metathesis of acrylonitrile. *Angew. Chem. Int. Ed.* **41**, 4035-4037 (2002).
6. Hore, M. J. A., Hammouda, B., Li, Y. & Cheng, H. Co-nonsolvency of poly(n-isopropylacrylamide) in deuterated water/ethanol mixtures. *Macromolecules* **46**, 7894-7901 (2013).
7. Pesek, S. L., Xiang, Q., Hammouda, B. & Verduzco, R. Small-angle neutron scattering analysis of bottlebrush backbone and side chain flexibility. *J. Polym. Sci. Part B: Polym. Phys*. **55**, 104-111 (2017).
8. Hammouda, B., Ho, D. L. & Kline, S. Insight into clustering in poly(ethylene oxide) solutions. *Macromolecules* **37**, 6932-6937 (2004).
9. Lang, X., Patrick, A. D., Hammouda, B. & Hore, M. J. A. Chain terminal group leads to distinct thermoresponsive behaviors of linear PNIPAM and polymer analogs. *Polymer* **145**, 137-147 (2018).
10. Lang, X., Lenart, W. R., Sun, J. E. P., Hammouda, B. & Hore, M. J. A. Interaction and conformation of aqueous poly(N-isopropylacrylamide) (PNIPAM) star polymers below the LCST. *Macromolecules* **50**, 2145-2154 (2017).
11. Landrum, G. RDKit: Open-source cheminformatics. 2006.
12. Jorgensen, W. L. & Tirado-Rives, J. Potential energy functions for atomic-level simulations of water and organic and biomolecular systems. *Proc Natl Acad Sci*. **102**, 6665-6670 (2005).
13. Dodda, L.S., Vilseck, J.Z., Tirado-Rives, J. & Jorgensen, W.L. 1.14* CM1A-LBCC: localized bond-charge corrected CM1A charges for condensed-phase simulations. *J Phys Chem B*. **121**, 3864-3870 (2017).
14. Dodda, L.S., Cabeza de Vaca, I., Tirado-Rives, J. & Jorgensen, W.L. LigParGen web server: an automatic OPLS-AA parameter generator for organic ligands. *Nucleic Acids Res*. **45**, W331-W336 (2017).
15. Mark, P. & Nilsson, L. Structure and dynamics of the TIP3P, SPC, and SPC/E water models at 298 K. *J Phys Chem A*. **105**, 9954-9960 (2001).
16. Ryckaert, J.-P., Ciccotti, G. & Berendsen, H. J. C. Numerical integration of the cartesian equations of motion of a system with constraints: molecular dynamics of n-alkanes. *J Comput Phys*. **23**, 327-341 (1977).
17. Darden, T., York, D. & Pedersen, L. Particle mesh Ewald: An N· log (N) method for Ewald sums in large systems. *J Chem Phys*. **98**, 10089-10092 (1993).
18. Pastorino, C., Kreer, T., Müller, M. & Binder, K. Comparison of dissipative particle

dynamics and Langevin thermostats for out-of-equilibrium simulations of polymeric systems. *Phys Rev E*. **76**,, 26706 (2007).
19. Eastman, P., Swails, J., Chodera, J. D., McGibbon, R. T., Zhao, Y., Beauchamp, K. A., Wang, L.-P., Simmonett, A. C., Harrigan, M. P., Stern, C. D., Weiwiora, R. P., Brooks, B. R. & Pande, V. S. OpenMM 7: Rapid development of high performance algorithms for molecular dynamics. *PLOS Comput. Biol*. **13**, e1005659 (2017).
20. McGibbon, R. T., Beauchamp, K. A., Harrigan, M. P., Klein, C., Swails, J. M., Hernández, C. X., Schwantes, C. R., Wang, L.-P., Lane, T. J. & Pande, V. S. MDTraj: a modern open library for the analysis of molecular dynamics trajectories. *Biophys. J*. **109**, 1528-1532 (2015).
21. Humphrey, W., Dalke, A. & Schulten, K. VMD: visual molecular dynamics. *J. Mol. Graph*. **14**, 33-38 (1996).
22. Harrigan, M. P., Sultan, M. M., Hernández, C. X., Husic, B. E., Eastman, P., Schwantes, C. R., Beauchamp, K. A., McGibbon, R. T. & Pande, V. S. MSMBuilder: statistical models for biomolecular dynamics. *Biophys J*. **112**, 10-15 (2017).
23. McGibbon, R. T. & Pande, V. S. Variational cross-validation of slow dynamical modes in molecular kinetics. *J. Chem. Phys*. **142**, 1-13 (2015).
24. Bowman, G. R. Improved coarse-graining of Markov state models via explicit consideration of statistical uncertainty. *J. Chem. Phys*. **137**, 134111 (2012).
25. Scherer, M. K., Trendelkamp-Schroer, B., Paul, F., Pérez-Hernández, G., Hoffmann, M., Plattner, N., Wehmeyer, C., Prinz, J.-H. & Noé, F. PyEMMA 2: a software package for estimation, validation, and analysis of Markov models. *J. Chem. Theory Comput*. **11**, 5525-5542 (2015).
26. Schrödinger, LLC. The {PyMOL} molecular graphics system, Version~1.8 (2015).
27. Tuvi-Arad, I. & Alon, G. Improved algorithms for quantifying the near symmetry of proteins: complete side chains analysis. *J. Cheminformatics* **11**, 39 (2019).
28. Dryzun, C., Zait, A. & Avnir D. Quantitative symmetry and chirality - a fast computational algorithm for large structures: proteins, macromolecules, nanotubes, and unit cells. *J. Comput. Chem*. **32**, 2526-2538 (2011).
29. O'Boyle, N. M., Banck, M., James, C. A., Morley, C., Vandermeersch, T. & Hutchison, G. R. Open Babel: an open chemical toolbox. *J. Cheminformatics* **3**, 33 (2011).
30. Neese, F, Wennmohs, F., Becker, U. & Riplinger, C. The ORCA quantum chemistry program package. *J. Chem. Phys*. **152**, 224108 (2020).
31. Chai, J.-D. & Head-Gordon, M. Long-range corrected hybrid density functionals with damped atom–atom dispersion corrections. *Phys. Chem. Chem. Phys*. **10**, 6615-6620 (2008).
32. Weigend, F. & Ahlrichs, R. Balanced basis sets of split valence, triple zeta valence and quadruple zeta valence quality for H to Rn: Design and assessment of accuracy. *Phys. Chem. Chem. Phys*. **7**, 3297-3305 (2005).
33. Baerends, E. J., Ellis, D. E. & Ros, P. Self-consistent molecular Hartree—Fock—Slater calculations I. The computational procedure. *Chem. Phys*. **2**, 41-51 (1973).
34. Dunlap, B. I., Connolly, J. W. D. & Sabin, J. R. On some approximations in applications of Xα theory. *J. Chem. Phys*. **71**, 3396 (1979).
35. Alsenoy, C. V. Ab initio calculations on large molecules: The multiplicative integral approximation. *J. Comput. Chem*. **9**, 620-626 (1988).
36. Kendall, R. A. & Fruchtl, H. A. The impact of the resolution of the identity approximate

integral method on modern ab initio algorithm development. *Theor. Chem. Acc*. **97**, 158-163 (1997).
37. Eichkorn, K., Treutler, O., Ohm, H., Haser, M. & Ahlrichs, R. Auxiliary basis sets to approximate Coulomb potentials. *Chem. Phys. Lett*. **240**, 283-290 (1995).
38. Eichkorn, K., Weigend, F., Treutler, O. & Ahlrichs, R. Auxiliary basis sets for main row atoms and transition metals and their use to approximate Coulomb potentials. *Theor. Chem. Acc*. **97**, 119-124 (1997).
39. Whitten, J. L. Coulombic potential energy integrals and approximations. *J. Chem. Phys.* **58**, 4496 (1973).
40. Bullheller, B. M., Rodger, A. & Hirst, J. D. Circular and linear dichroism of proteins. *Phys. Chem. Chem. Phys*. **9**, 2020-2035 (2007).
41. Besley, N. A. & Hirst, J. D. Theoretical studies toward quantitative protein circular dichroism calculations. *J. Am. Chem. Soc.* **121**, 9636-9644 (1999).
42. Anderson, J. A., Glaser, J. & Glotzer, S. C. HOOMD-blue: a Python package for high-performance molecular dynamics and hard particle Monte Carlo simulations. *Comput. Mater. Sci.* **173**, 109363 (2020).
43. Nguyen, T. D., Phillips, C. L. Anderson, J. A. & S. C. Glotzer, S. C. Rigid body constraints realized in massively-parallel molecular dynamics on graphics processing units. *Comput. Phys. Commun.* **182**, 2313-2307 (2011).